ABSTRACT

Title of Dissertation: **DEVELOPMENT OF FLUORESCENT IMAGING METHODS AND SYSTEMS TO DETERMINE PHOTODYNAMIC POTENTIAL AND INFORM CANCER TREATMENT EFFICACY**

Brandon Gaitan, Doctor of Philosophy, 2022

Dissertation Directed By: Assistant Professor, Huang Chiao Huang, Fischell Department of Bioengineering

Photodynamic therapy (PDT) is a treatment modality that has gained rapid popularity in both research and clinical settings over the past 20 years. PDT involves harmless red/near-infrared light excitation of non-toxic photosensitizers to generate reactive molecular species (RMS) that can induce tissue damage and/or cell death. In addition, the fluorescence signal generated from the photosensitizer can also be used for optical imaging. These effects have been harnessed for image-guided treatment of cancer and other diseases. As PDT gains popularity, it is crucial to understand and monitor different factors that could impact overall treatment efficacy. These factors include, but are not limited to, the RMS yield of photosensitizers, the distribution of photosensitizers in tissue, and the PDT activation depth in tissues. Our work focused on developing methodologies and devices to characterize and improve PDT treatment. In collaboration with the FDA, we developed a cell-free assay to rapidly and more quantitatively determine the potential phototoxicity of fluorescent probes through the measurement of singlet oxygen. We also developed a method to compare the maximal PDT activation depth of FDA-

approved photosensitizers (BPD and PpIX) in the brain. We found that BPD can be activated 50% deeper into brain tissues compared to PpIX at the same radiant exposure. Next, we tested the ability of a 3D imaging system, Fluorescence Laminar Optical Tomography (FLOT), to image the distribution of photosensitizers in the rodent brain. We demonstrated that FLOT could accurately map the photosensitizer distribution up to 0.5 mm in tissues. Lastly, we developed an autofluorescent-based endoscopic imaging system to measure the metabolic impact of PDT on cancer and normal tissues, finding that PDT leads to significant changes in tissue metabolism immediately after treatment. In summary, we have developed a series of systems that can aid in PDT treatment optimization in three major ways:1) rapidly quantifying the singlet oxygen production of photosensitizers, 2) more accurately measuring a photosensitizers localization and activatable depth, and 3) developing the ability to measure a tissues response to PDT in real-time.

DEVELOPMENT OF FLUORESCENT IMAGING METHODS AND SYSTEMS TO DETERMINE PHOTODYNAMIC POTENTIAL AND INFORM CANCER TREATMENT EFFICACY

by

Brandon Gaitan

Thesis submitted to the Faculty of the Graduate School of the
University of Maryland, College Park, in partial fulfillment
of the requirements for the degree of
Doctor of Philosophy
2022

Advisory Committee:

Assistant Professor	Huang-Chiao Huang, Chair
Associate Professor	Yu Chen, Co-Chair
Associate Professor	Giuliano Scarcelli
Professor	Yang Tao
Professor	Mario Dagenais, Dean's Representative

Acknowledgments

I would like to thank my advisors, Dr. Chen and Dr. Huang, for their guidance and encouragement during my graduate studies over the last five years, which has developed me into a better scientist and researcher. I am also incredibly grateful to the entire Huang lab for taking me in as one of their own lab members, aiding me in both my professional and personal life. The journey through graduate school would have been more difficult and less pleasant without the support of the Huang lab. A special thanks to the Scarcelli lab, who have given me help when it came to device development and letting me borrow optical components for my own projects. Finally, I would like to thank my family, friends, and partner for their support and sacrifices that they have made along the way. Without all their help, I would not have been able to reach this milestone.

Table of Contents

List of Tables

Chapter 2

List of Figures

Abbreviations

Chapter 1

- PSA (Prostate-Specific Antigens)
- PDT (Photodynamic Therapy)
- RMS (Reactive Molecular Species)
- 5-ALA (5-Aminolevulinic Acid Hydrochloride)
- PpIX (Protoporphyrin IX)
- S0 (Ground State)
- S1 (Higher Energy State)
- T1 (Triplet Excited State)
- SO (Singlet Oxygen)
- ICG (Indocyanine Green)
- FLOT (Fluorescence Laminar Optical Tomography)
- NADH (Nicotinamide Adenine Dinucleotide Hydrogen)
- FAD (Flavin Adenine Dinucleotide)
- SOSG (Singlet Oxygen Sensor Green)
- BPD (Benzoporphyrin Derivative)

Chapter 2

- 3T3-NRU (3T3-Neutral Red Uptake)
- CDER (Center for Drug Evaluation and Research)
- CBER (Center for Biologics Evaluation and Research)
- H_e (Radiant Exposure)
- ICH (The International Council for Harmonisation)
- DI (Deionized)

Chapter 3

- FGS (Fluorescence-guided surgery)
- FDA (Food and Drug Administration)
- GBM (Glioblastoma Multiforme)
- Nal (Nanoliposomal)
- μ_s' (Reduced Scattering Coefficient)

Chapter 4

- SFDI (Spatial Frequency Domain Imaging)
- DOT (Diffuse Optical Tomography)
- OCT (Optical Coherence Tomography)
- PIT (Photoimmunotherapy)
- MIP (Maximal Intensity Projections)
- DPPC (Dipalmitoylphosphatidylcholine)
- DSPE-PEG (Distearoylphosphatidylethanolamine-Methoxy Polyethylene Glycol)
- DOTAP (1,2-Dioleoyl-3-Trimethylammonium-Propane)
- FWHM (Full Width at Half Maximum)
- CCD (Charged Coupled Device)

- MC (Monte Carlo)
- μ_s (Scattering Coefficient)
- W (Weighted Matrix)

Chapter 5

- ORR (Optical Redox Ratio)
- FCCP (Carbonyl cyanide 4-(trifluoromethoxy)phenylhydrazone)
- LOD (Limit of Detection)
- LDH (Lactate Dehydrogenase)

Chapter 1: Introduction*

1.1 Motivation

1.1.1 Cancer and patient outcomes

Cancer is one of the most deadly and life-threatening diseases. In the US alone, 1.9 million people are estimated to be diagnosed with some form of cancer, with 600 thousand succumbing to the disease in 2021 [1]. Even though treatment methods have improved over time, with over 3 million cancer deaths averted between 1991 and 2018 [1], there are still many cancers that have a high number of mortalities and/or mortality rates. For example breast cancer has a 5-year survival rate of 80% [2], but due to its prevalence was still estimated to cause 43,000 deaths in 2021 in the US alone [1]. Another is glioblastoma, an aggressive type of brain cancer, which has been found to have a 10-year survival rate of less than 1% [3]. Because of the risk and prevalence of this disease, methods are needed to improve patient outcomes, which can come in a few forms.

1.1.2 Current treatment techniques in the field of oncology

Treatment methodologies for treating cancer are dependent on various factors. These can include but are not limited to the type/aggressiveness of cancer, the

* Part of the contents in this chapter were modified and reproduced from B. Gaitan et al., "Depth-resolved imaging of photosensitizer in the rodent brain using fluorescence laminar optical tomography," *Journal of Biomedical Optics* 25(9), 2020 with permission.

location of the cancerous tissue, and the impact that the cancer/treatment will have on a patient's quality of life.

With prostate cancer, the risk of death is so low that one is more likely to die from outside causes than the diagnosed cancer [4], leading a patient, in some cases, to choose active monitoring rather than treatment until a certain threshold is reached. For example, the ProtecT Active monitoring group would not treat patients diagnosed with prostate cancer unless it was of a certain aggressiveness. Instead, they would perform active monitoring by measuring prostate-specific antigens (PSA) every 3-12 months and not perform any invasive biopsies unless a patient was found to have an increase in PSA of 50% or greater [5], after which treatment options such as chemotherapy, radiation, and surgery were considered. And even under these circumstances, there are patients who decline treatment, with some of the most cited reasons being fear of side effects and the potential high risk of treatment due to other comorbidities [6].

Another example on the opposite end of the spectrum is glioblastoma, which has an extremely low survival rate. Various modalities are currently used to treat gliomas. It has been found that when a chemotherapeutic (O6-methylguanine DNA methyltransferase inhibitor) is combined with radiative therapy, patients demonstrate an increase in 2-year survival from 10.9% to 27.2% [7]. Surgery has also been a useful tool in the treatment of gliomas. An analysis of 645 patients found that the overall survival was increased from 6.6 months to 11.3 months if complete resection was performed [8]. Although these treatment modalities have been found to extend a patient's life, the impact on a patient's quality of life can be drastic. Moreover, due to

some tumor cells/tissue being left behind in the tumor margins, recurrence is likely, which is why the patient only increases their overall survival by 4.7 months if resection is performed.

By looking at these examples, it is clear that a highly targeted treatment modality with minimal invasiveness is necessary to treat areas in which an invasive procedure may not be possible and to eliminate residual cells and tissue that can lead to recurrence. One treatment modality which may be able to fill this role is photodynamic therapy.

1.1.3 Photodynamic therapy as a cancer treatment modality

Photodynamic therapy (PDT) is a treatment modality that involves the use of a photo-activated compound, also known as a photosensitizer, that causes little to no toxicity until it is exposed to a specific wavelength of light. When this photosensitizer is exposed to a certain wavelength of light (the specific wavelength of light is compound dependent), the photosensitizer reacts with the surrounding environment to produce reactive molecular species (RMS [e.g., $^1O_2$, $\bullet OH$, $O_2^{\bullet-}$, H_2O_2]) [9], which can then be used to kill cancer tissue. Because of this unique activation condition, PDT has several advantages as a cancer treatment technique. One advantage is that this method is relatively noninvasive, as the photosensitizer does not need to be injected directly into the organ of interest but can be either delivered orally or intravenously, and the activation involves delivering light to the tissue, which is also minimally invasive. Another advantage is that effects can be very localized, as even if the

photosensitizer is non-targeted and present in various tissue, only the portion which is exposed to light will be activated.

Currently, there are many clinical trials in which PDT is being proposed/used as a cancer treatment agent. One example includes a phase 2 clinical trial to treat prostate cancer which involves the IV injection of the photosensitizer WST11 and then exposing the cancerous region to a 753nm light with a light dose of 200-300J/cm (NCT00707356). Another example is a clinical trial to treat glioblastoma by having the patient drink 5-aminolevulinic acid hydrochloride (5-ALA) 4 hours before surgery, the body converting it to the natural photosensitizer Protoporphyrin IX (PpIX) and exposing the cancerous tissue to a laser to activate the photosensitizer and treat the tumor tissue (NCT03048240). There are many other clinical trials using PDT to treat cancers such as breast (NCT02872064, NCT02939274), skin (NCT00007969), and pancreatic (NCT00003923) cancer. There have even been photosensitizers that have gained government approval, such as Visudyne®, which has been FDA approved to treat age related macular degeneration, and an IR700 conjugate, under the name of ASP-1929, which has been approved in Japan to treat head and neck squamous cell carcinomas.

Although PDT as a treatment method has been found to treat cancer in patients and has been gaining popularity, many parameters need to be quantified before a photosensitizer can go from the research lab to being used to treat a patient in the clinic.

1.1.4 Preliminary testing needed for PDT prior to clinical testing

Before a treatment can be used on a patient, several critical parameters need to be quantified. These include, but are not limited to, how much RMS does the photosensitizer produce [10-12], the distribution/accumulation of the photosensitizer in the tumor tissue/other organs [13-15], the amount of time it takes for the photosensitizer to accumulate in the area of interest [14, 15], the amount of oxygen in the tissue/surrounding environment [11, 12], the amount of light to deliver to the tissue of interest [11, 12, 16, 17], and the penetration depth and energy distribution of the activation light in the tumor [16-18]. These stated parameters can have a profound impact on if the treatment will be effective. For example, if the photosensitizer does not produce RMS in a large enough quantity, there will be no tumor-killing effect. Or even if the photosensitizer does produce enough RMS, if the tissue is exposed to light before the photosensitizer has enough time to accumulate, there will be little to no treatment effect. Because of this, extensive studies need to be performed to help quantify the stated parameters before clinical use can move forward.

1.2 Background

1.2.1 Photosensitizer

As mentioned in section 1.13, a photosensitizer causes little to no toxicity until it is exposed to a specific wavelength of light, after which it interacts with the surrounding environment to create RMS, with the two most studied kinds of RMS

being those that are produced by type 1 (•OH, $O_2^{\bullet-}$, H_2O_2) or type 2 ($^1O_2$) reactions [9], which then can cause cellular toxicity.

The way these compounds function is by absorbing a specific wavelength of light, exciting the electrons from a ground state (S0) to a higher energy state (S_1). From here, a photon can either relax back down to the ground state and emit energy in the form of fluorescence, or intersystem crossing can occur, and the electron can enter a triplet excited state (T_1). The electron can relax back down to the ground state, producing phosphorescence, or it can generate RMS. Type 1 reactions are produced through photoinduced electron transfer leading to the creation of hydrogen peroxide, superoxide, and hydroxyl radicals, while type 2 reactions occur through energy transfer, creating singlet oxygen (SO) from triplet oxygen [19]. The process involved in making these RMS can be seen in Figure 1.1.

Because of the unique features involved in the creation of RMS, most photosensitizers are also inherently fluorescent, making pharmacokinetic tracing easier and even allowing them to be used as contrast agents in fluorescence-guided resection [20-22].

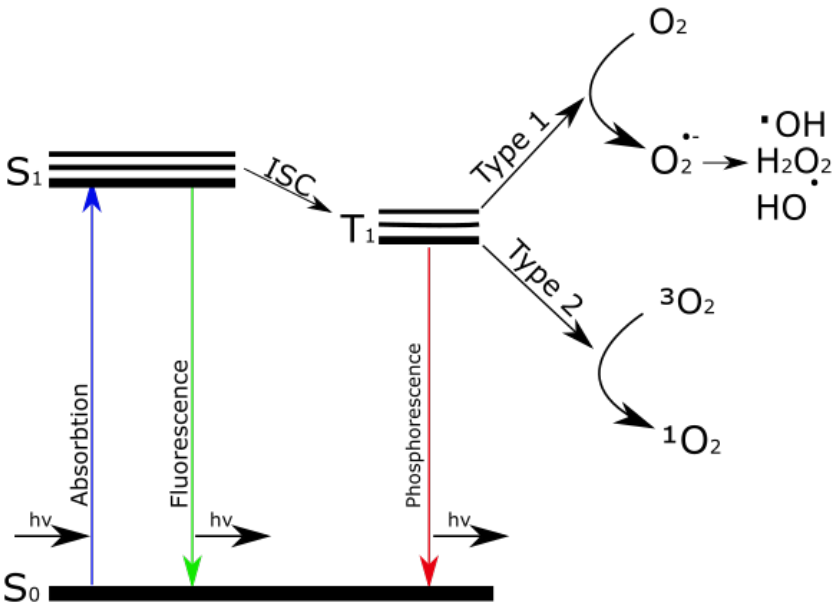

Figure 1.1: Jablonski Diagram
A diagram demonstrating the electron pathways that can lead to the creation of RMS, focusing on type 1 and type 2 reactions. $S_{0/1}$ are the singlet ground/excited states, ISC is intersystem crossing, T_1 is the triplet state, and hv is light.

After the RMS is produced, they can react with their surroundings to damage and kill cells using a variety of mechanisms. For example, RMS can interact with a cell membrane through lipid peroxidation, damaging the cell membrane and interrupting cell to cell signaling. RMS can also cause breakage in DNA, which can alter gene expression and even cause cellular apoptosis [23, 24]. In addition to lipid and DNA damage, RMS are also known to damage proteins through protein oxidation, altering their function [25]. These effects are limited to sites very close to where the photosensitizer is targeted, though due to SO's lifetime, which is found to be a maximum of 100 ns limiting its diffusion distance to 30nm in tissue [26].

1.2.2 Probe targeting

When developing an imaging or therapeutic agent, it is important to determine what targeting method is going to be used for said agent. There are three main

targeting methods: 1) vascular/tissue level changes leading to accumulation, 2) metabolic targeting, and 3) antibody targeting. Vascular targeting normally does not involve the modification of an agent but rather takes advantage of physical changes in tumor tissue to cause accumulation. One of the most popular examples is ICG (Indocyanine Green) and fluorescein, which accumulate in the tumor due to having a more permeable endothelium, leading to the probes accumulation [27]. Metabolic modalities are similar to probes that depend on tissue-level changes but depend more on cellular level metabolic changes for targeting, such as the accumulation of endogenous PpIX due to metabolic changes in tumor tissue leading to increases in ferrochelatase and decreases in coproporphyrinogen [28]. Lastly, there are antibody-targeted agents which normally involve conjugation to a targeting modality. An example of this would be the conjugation of the photosensitizer IR700 to cetuximab for tumor targeting [29].

1.2.3 Fluorescence laminar optical tomography

Fluorescence Laminar Optical Tomography (FLOT) works by taking advantage of source and detector separations and the fact that scattering is the dominant attenuation factor in most tissue [30] since photons being remitted from the tissue or phantom at larger distances from the source have most likely penetrated deeper into the tissue. By obtaining information gathered from many source-detector separations, it becomes possible to extract depth-resolved information [31]. To account for the tissue attenuation, a weighted matrix is used to predict light propagation in the tissue, with most systems choosing to use a Monte Carlo light propagation model to solve for the radiative transport equation [32, 33]. By using the

estimated light propagation with depth-resolved information obtained using the source-detector pairs, FLOT can be used to reconstruct more quantitative, 3D depth-resolved information [34-36].

1.2.4 Autofluorescent imaging of NADH and FAD

Nicotinamide adenine dinucleotide hydrogen (NADH) and flavin adenine dinucleotide (FAD) are electron carriers in various cellular metabolic cycles such as oxidative phosphorylation, the Krebs cycle, and glycolysis. Because NADH and FAD function as electron donator and acceptor, respectively, measuring these metabolites can give detailed insights into the state of the tissue, such as if there are modulations of the electron transport chain [37, 38] or if the tissue is oxygen/nutrient saturated or starved [39, 40]. Through these measurements, five different cellular states were identified. In addition, by measuring the ratio of these two molecules, known as the redox ratio ([FAD]/([FAD]+[NADH])), the relative oxidative state of the cellular metabolism can be deduced [41]. For example, state 2 can be identified when the NADH concentration is low and the FAD concentration is high [a high redox ratio], which means that the tissue is likely being starved of necessary substrates. State 4, on the other hand, corresponds to a high NADH and low FAD concentration [a low redox ratio], meaning that the tissue is in a resting state and has plenty of nutrients and oxygen [42, 43]. And because of the metabolic insights that NADH and FAD concentrations give into the tissue of interest, several researchers have also found that they can also help detect tumor tissue, as well as to map PDT treatment effects *in vitro* [44] and *ex vivo* [45].

1.3 Goals and Objectives

PDT is a treatment modality that has started to gain popularity in the past few years, with several photosensitizers gaining clinical approval, such as Visudyne, PpIX, and ASP-1929 (Japan only). With PDT gaining popularity, more photosensitizers are being developed to aid in the treatment of various forms of cancer. But as mentioned in section 1.14, many parameters need to be quantified before these agents can be used in a patient. To that end, our work has focused on developing methods, tools, and techniques to give researchers the ability to better understand a photosensitizer's potential as a cancer treatment agent and to aid in determining the optimal treatment parameters for one's photosensitizer of choice. In addition, we also investigate how one can use autofluorescent molecules to track changes in tumor metabolism to aid in quantifying PDT treatment effectiveness

Chapter 2 focuses on using the assay singlet oxygen sensor green (SOSG) to quantify the SO potential of various fluorophores and photosensitizers to determine if they are best used as a fluorescence imaging agent or as a photosensitizer. Through the development of this standardized cell-free methodology, we found that it is possible to quantify and compare the amount of SO produced by a fluorophore/ photosensitizer, specific to the wavelength, irradiance (the exposure rate at the projected interface [mW/cm^2]), and radiant exposure (total integrated time of the irradiance on the surface of the interface [J/cm^2]) used since the SO that a photosensitizer produces is directly related to these factors. By using this methodology, a user would be able to quickly quantify and compare the SO

production of various probes and determine if a compound is potentially safe to use for imaging or if it might be able to serve as a potential photosensitizer.

In chapter 3 we investigated and developed a test method to determine how deep a potential photosensitizer can be activated in the brain using either PpIX or benzoporphyrin derivative (BPD). This was done by inserting 300μm capillaries filled with either PpIX or BPD at various heights in a rodent brain, with the brain being illuminated by its corresponding laser activation light from the bottom up. Because the creation of RMS can lead to photobleaching, by measuring the degree of photobleaching, we could approximate the relative activation of the photosensitizer and the creation of RMS. Using our methodology, we found that, depending on the photosensitizer and activation wavelength, PDT's therapeutic effects can be activated 1-2cm into tissue.

After investigating the potential activation depth of a photosensitizer, it is important to determine the distribution of photosensitizer in the tissue of interest, as accumulation in the wrong location can lead not only to a lack of treatment effectiveness but could potentially harm the patient. In chapter 4, we used a FLOT system and compared it to 2D imaging to determine if it would be better able to quantify photosensitizer concentrations in the brain. We filled capillaries with a photosensitizer and placed them into phantom and *ex vivo* rodent brains, with FLOT and maximum intensity projection images obtained. The signal loss in the z-direction was quantified and compared to see which methodology could compensate better for signal loss caused by tissue attenuation. We found that by using FLOT, one can

compensate for signal loss in deeper parts of the tissue when imaging in *ex vivo* rodent brain compared to maximum intensity projection imaging.

In addition to quantifying a photosensitizer's potential RMS production, penetration depth, and distribution, it is important to also determine if PDT treatment is taking place. In chapter 5, we demonstrate the development of an endoscopic imaging device to image the autofluorescent molecules NADH and FAD. As mentioned in section 1.23, these molecules can lend insight into the metabolism of tumor/normal tissue. In our study, we demonstrate the ability of our endoscopic system to 1) image NADH and FAD in phantoms and tissue, 2) differentiate between normal tissue and tumor tissue, and 3) track the metabolic changes that PDT causes in treated tumor tissue.

Finally, in chapter 6, we focus on potential future directions for the project and ongoing work.

Chapter 2: Quantifying the Photochemical Damage Potential of Imaging/PDT Probes: Singlet Oxygen Production[†]

2.1 Introduction

Recent advances in optical imaging have the potential to significantly improve patient outcomes, with one of the most promising intraoperative approaches being contrast-enhanced fluorescence imaging. This technique has the advantage of being real-time, minimally invasive, and increasingly accepted by clinicians.

Over the past 20 years, two of the most widely used clinical fluorophores have been ICG and fluorescein. These agents have found success as non-targeted dyes, particularly for use in procedures such as retinal angiography [46, 47] and fluorescence-guided surgical resection [48, 49]. Methylene Blue is another non-targeted fluorophore, initially being found to selectively stain cells with dysplasia in Barrett's esophagus [50], but also studied as a cancer imaging agent [51, 52]. Proflavine has also been investigated as an imaging agent, particularly for its ability to image cancerous tissue, including oral carcinomas [53]. And in recent years, molecular-targeted imaging agents have begun to achieve clinical viability, such as IR800, which is normally used as a targeted imaging agent through conjugation to a monoclonal antibody, being used in over 15 clinical trials. Many of these trials are for the fluorescence-guided surgery of different types of cancer, such as glioblastoma

[†] The contents in this chapter were reproduced from B. Gaitan et al., "Quantifying the Photochemical Damage Potential of Contrast-Enhanced Fluorescence Imaging Products: Singlet Oxygen Production", *Photochemistry and Photobiology,* 2022 (Accepted Manuscript) with permission.

(NCT03510208), esophageal carcinomas (NCT03558724), and breast cancer (NCT02583568).

When exposed to light at certain wavelengths, these fluorescent probes can exhibit photochemical processes that produce phototoxicity [54]. These processes are similar to photochemical effects of tissue exposure to ultraviolet radiation, which can cause DNA damage – a scenario that is addressed in existing optical radiation safety standards such as in the IEC 60825-1:2017. As previously mentioned in section 1.2.1, the primary mechanism of phototoxicity involves the production of RMS such as SO, superoxide anions, hydrogen peroxide, and hydroxyl radicals [55, 56]. RMS can cause damage to cells directly through protein oxidation, which can inhibit certain enzymatic processes [57], lipid peroxidation, which can cause damage to cellular membranes [58], and nucleic oxidation, which can cause DNA damage and lead to necrosis and/or apoptosis [59].

The production of RMS involves the absorption of light that excites the electrons from the ground state to its excited singlet state. When the electron relaxes back down to the ground state, light can be emitted in the form of fluorescence, but another possibility is that after excitation, the electrons go to a triplet state that allows for the transfer of energy to ground state molecules, creating RMS (See Chapter 1, Figure 1.1). Perhaps the most significant RMS is SO. In addition to being the most well-studied form of RMS, SO is a commonly generated species since it represents oxygen's lowest excited state [60, 61]. Additionally, SO has one of the largest redox potentials when compared to other RMS, with a reduction potential of 0.92 E_0/V [61]; thus, it is more likely than most other RMS to react with its surrounding environment.

While prior studies have focused on developing test methods for the detection of phototoxicity and SO [62, 63], none have focused on quantifying the potential toxicity of fluorescent products using test methods that might be widely adopted.

Because the process of RMS production and fluorescence are closely related, several agents appear to be capable of dual-use, in either imaging or phototherapy. For example, 5-ALA–induced PpIX tends to selectively accumulate in tumors [64, 65]. This accumulation has been leveraged to aid in the resection of glioblastoma during fluorescence-guided surgery, with PpIX specifically allowing the surgeon to better visualize tumors compared to white light imaging [66, 67]. But PpIX has also been leveraged as a cancer treatment agent when administered at a higher irradiance and longer exposure time [68, 69]. Another was IR700 which was initially used to image colorectal cancer [70, 71] and pancreatic cancer [72] in mice but has also been found to produce high levels of RMS. This feature has been exploited to treat bladder [73], lung [74], and breast [75] cancer using PDT, acting as a targeted treatment agent through conjugation to an antibody. Methylene Blue is another agent that has found off-label use as an imaging agent but has also been found to produce RMS, leading to DNA damage *in vivo* [76, 77]. Proflavine has been investigated as an imaging agent to detect oral carcinomas [53] but has also been used as a PDT agent to inactivate the herpes simplex virus [78]. Therefore, it is important to go beyond identifying probes as phototoxic or non-phototoxic; rather, to evaluate each product as a whole – the agent, device, and dosing regimen together.

A variety of methods have been implemented to evaluate phototoxicity, including cytotoxicity assays [Neutral Red Uptake (3T3-NRU)] and markers of DNA

damage such as the comet assay [79]. Guidance documents provided by the Center for Drug Evaluation and Research (CDER) and Center for Biologics Evaluation and Research (CBER) provide recommendations for performing RMS testing. Although RMS testing methods have been defined, these methodologies have fixed concentrations, radiant exposures (H_e), and wavelengths regardless of the fluorescent probes' clinical use parameters, focusing more on phototoxicity caused by sunlight. For example, OECD/OCDE TG 432 guidelines call for the use of a solar simulator, emitting wavelengths between 290nm-700nm and a H_e of 5J/cm^2. The International Council for Harmonisation of Technical Requirements for Pharmaceuticals for Human Use (ICH) also points out the need to perform initial *in vitro* phototoxicity tests before clinical trials are performed. Although the importance of determining the potential phototoxicity of drugs has been established, no literature has been published developing or evaluating a testing methodology that focuses on phototoxicity screening of products considering the specific concentrations, irradiances, and radiant exposures that the probe will be exposed to in the clinic.

The purpose of this research is to facilitate the development and clinical translation of emerging fluorescence products through the establishment of a standardized and least burdensome methodology for phototoxicity screening. This aligns with safety evaluation needs described in a 2017 consensus Meeting Report by authors from academia, industry, and government agencies [80]. Through the use of a battery of cell-free assays, it may be possible to screen imaging products for the potential to produce substantial RMS, and thus the need for further testing (e.g., cell-based assays). In this study, our primary goal was to evaluate an approach based on a

commercial assay to quantify SO production in an objective, quantitative and consistent manner. This involved performing measurements that elucidate differences between well-known fluorescent probes under a range of clinically relevant dosing scenarios. In addition to providing insights into RMS generation in specific agents and the limitations of the assay approach, this chapter describes potential best practices for standardizing preclinical phototoxicity screening of fluorescent products.

2.2 Methods

2.2.1 Overview

This study involved three main phases: (1) determination of relevant agent concentrations, optical exposure wavelengths, and radiant exposure levels through an extensive literature search of clinical and animal studies; (2) exposure of each agent over a range of concentrations and radiant exposures and measurement of fluorescence levels generated by a commercial SO assay for each case; and (3) analysis of the results to assess agreement with the literature, differences and similarities between agents, and overall performance and limitations of the assay. Through these steps, our intent was to evaluate the potential of this approach, identify best practices for its standardized implementation and provide insight into the SO generation potential of specific agents.

2.2.2 SO Assay

The assay used to detect SO produced by the fluorophore is a commercially available product, SOSG (ThermoFisher, Eugene, OR), that has been used in

numerous prior studies [62, 81-83]. SOSG has been used for over a decade, becoming one of the most widely used methods for measuring SO due to its high specificity, being activated minimally by other reactive molecular species such as hydrogen peroxide and superoxides [84]. SOSG is used regularly to qualify the amount of SO produced by phototoxic molecules in the field of PDT [83, 85]. SOSG is likely composed of a fluorescein-based dyad that is bonded to an anthracene moiety. In its normal state, the anthracene quenches the fluorescein, inhibiting its fluorescence. When exposed to SO, the anthracene gets converted to endoperoxide, which does not cause intermolecular quenching, allowing the fluorescein to fluoresce [81, 86].

The SOSG assay was prepared by mixing a single 100μg vial with 330μL of methanol to make a final concentration of 500μM. The solution was diluted with deionized (DI) water to a SOSG concentration of 7μM in the well plate and mixed with the individual fluorophore solutions described below. The SOSG assay was found to have an absorption peak at 485nm and an emission peak at 522nm, as seen in Figure 2.3.

2.2.3 Fluorophore concentrations and illumination levels

The rate of RMS generation depends on the spectrum and H_e of the light source, as well as the concentration of the fluorescent agent. Therefore, we attempted to replicate clinically relevant scenarios – illumination wavelengths and maximum H_e's were determined from clinical studies and *in vivo* experiments for individual fluorophores. Illumination was performed from a very low level to approximately twice the likely maximum clinical H_e. After a fluorophore concentration was

identified as the most clinically relevant level, a set of values from near zero to approximately twice the maximum clinically relevant level were used to evaluate variations in SO production.

A limited review of literature enabled the identification of appropriate parameter spaces for the exposure of each agent. ICG (Adooq® BioScience, Irvine, CA) was reconstituted in DI water and diluted to a stock concentration of 1mM, and stored at 0˚C while wrapped in foil to avoid light exposure. The concentration range used was 6.5μM – 26μM, and the H_e range was 0 – 20J/cm^2 and excited at a wavelength of 785nm. ICG doses were based on blood plasma values found in human subjects [87, 88]. The H_e and wavelength of 785nm were derived from values used for fluorescent-guided surgery [89]. A concentration range of 1μM – 7.5μM for Methylene Blue (Sigma Aldrich, St. Louis, MO) was used based on pharmacokinetics data acquired after intravenous administration of 100mg in human subjects [90]. The H_e of 0 – 6 J/cm^2 was determined through camera exposure times required during open surgery [91]. The concentration range used for IR800 (LI-COR, Inc, Lincoln, NE) was between 2.5 μM – 20 μM, determined based on clinical studies using IR800 as a contrast agent for fluorescence guided surgery [92, 93]. The IR700 (LI-COR, Lincoln, NE) concentration range of 0.125μM – 1μM was based on *in vivo* studies where blood and the serum concentration were measured in rodents [94], as well as the biodistribution of IR700 measured in macaques [13]. For both IR700 and IR800, the H_e range was 0 – 6 J/cm^2, based on current imaging devices and the likely duration of imaging during surgery [95], with the wavelengths of 785nm and 685nm also taken from the excitation wavelengths of currently used devices [95]. For

proflavine (Sigma Aldrich, St. Louis, MO), we used a concentration range of 1.5μM – 12μM, a H_e ranges of 0 – 6 J/cm^2, and excited at 445nm. The concentrations, H_e's and wavelength used were based on human trials using proflavine as an imaging agent to detect oral cancer [53, 96]. Rose Bengal (Sigma Aldrich, St. Louis, MO) is not a clinical imaging agent but was included as a positive control since it is known to generate large amounts of SO, to the point where it has been used as a light-activated anti-microbial agent [97]. Rose Bengal concentrations (0.5 – 4μM), exposure levels (H_e of 0 – 1J/cm^2), and wavelength were selected to achieve similar clinical exposure levels as the other fluorophores tested, to directly compare results. For all fluorophores, 165μL of the dilution was placed into individual wells in a 96-well plate. A brief literature review of *in vivo* concentrations and illumination parameters for each fluorophore is provided in Table 2.1. The concentrations, excitations wavelengths, irradiances, and H_e's used in the experiment are summarized in Table 2.2.

Table 2.1: Literature Review of Probes

Literature review summary focusing on the clinical use of fluorescent probes: concentration, excitation wavelength, and irradiance.

Fluorophore	Model	Use Case	Conc.	Excitation Wavelength	Irradiance	Imaging time	Citation
ICG							
	Human	Lymphatic Imaging	0.2mL Injected	760nm	NA	NA	Unno, N. et al., 2007 [98]
	Human	Lymphatic Imaging	1mL of 0.5% ICG Injected	750 – 800nm	NA	30min	Takeuchi, M. et al., 2012 [99]
	Human	Blood Conc. of ICG	5-30 mg/L in plasma	805nm	NA	NA	Imai, T., 1998 [100]
	NA	Instrument Review	NA	785nm	1.9 mW/cm^2	NA	Zhu, B., 2015 [89]
	Human	lymph node Imaging	1mL Injected	760nm	4 mW/cm^2	15min	Tagaya, T., 2008 [101]
IR800							
	Human	Head and Neck Surgery	5.2 – 130 mg total injected	775nm	NA	NA	Gao, R., et al., 2018 [92]
	Human	Glioblastoma Imaging	50-100 mg injected	NA	NA	NA	Miller, S., et al., 2018 [93]
	NA	Instrument Review	NA	780nm	3-30 mW/cm^2	NA	D'Souza, A., et al., 2016 [95]
Proflavine							
	Human	Oral Cancer Imaging	0.01 % (w/v)	455nm	NA	NA	Shin, D., et al., 2010 [53]
	Human	Oral Cancer Imaging	0.01 %	455nm	NA	3-15min	NCT01269190 (2016)
	Human	Imaging of Barrett's – Related Neoplasia	0.01 % (w/v)	435/500nm	8.2mW/14.9mW	NA	Tang, Y., et al., 2016 [96]
Methylene Blue							
	Human	Intravenous Bio-availability	600 – 2000 ng/mL in blood	NA	NA	NA	Stefano, A., et al., 2018 [102]
	Swine	Uterine Imaging	0.1 mg/kg Injected	670nm	2.5 mW/cm^2	NA	Matsui, A., et al., 2010 [91]
	Human	Uterine Imaging	0.25-1 mg/kg injected	670nm	1.08 mW/cm^2	>5min	Verbeek, F., et al., 2013 [51]
	Human	Breast Cancer Imaging	1mg/kg injected	670nm	1.08mW/cm^2	NA	Tummers, Q., et al., 2014 [52]
IR700							
	Primate	Bio-distribution of injected	0.1-10 ug/g present in tissue	700nm	NA	NA	Boer, E., et al., 2015 [13]
	Mouse	EGFR targeting	100 ug injected	689nm	25mW	2-20 min	Sato, K., et al., 2014 [29]
	NA	Instrument Review	NA	680nm	3-30 mW/cm^2	NA	D'Souza, A., et al., 2016 [95]

Table 2.2: Summarized Experimental Properties
Concentration range, excitation wavelength, irradiance, and H_e values used in our experiments to generate SOSG production plots.

Fluorophore	Conc. Range (μM)	Excitation Wavelength (nm)	Irradiance (mW/cm^2)	Max H_e (J/cm^2)
ICG	6.5 – 26	785	3.8	20
IR800	2.5 – 20	785	5	6
Proflavine	0.5 – 12	445	2.8	6
MB	1 – 7.5	665	3.4	6
IR700	0.125 – 1	685	3.2	6
Rose Bengal	0.5 – 4	520	1	1

2.2.4 Optical exposure and measurement approaches

A custom setup was developed to illuminate samples in a 96-well plate (Figure 2.1). The system is composed of a laser diode controller (Thorlabs, Inc, Newton, NJ), a laser diode, a collimator(f=50mm), and a 20˚ square diffuser (ED1-S50-MD, Thorlabs, Inc, Newton, NJ). The system was set to illuminate a 7cm x 7cm area, but only a 2.5cm x 1.75cm area (six wells in a 96-well plate) was used, choosing a six-well area with a variation [(max irradiance-min irradiance)/max irradiance] of <10%. The two main reasons that a max variation of 10% was chosen is that this is approaching the limits of our setup due to certain non-uniformities in our laser diodes, and at this max variance, the conclusions drawn in this study would not be impacted. Ideally, the variance would be reduced in the future through the use of more uniform laser diodes. TO-can lasers (Thorlabs, Inc, Newton, NJ) were used to expose the different fluorophores with the following central wavelengths: 520 nm (Rose Bengal), 785 nm (ICG/IR800), 660 nm (Methylene Blue), 685 nm (IR700), and 450 nm (Proflavine). These are the wavelengths most commonly used to excite each fluorophore in a clinical setting. After each plate of samples was illuminated for the

appropriate duration to achieve the desired total H_e, assay fluorescence was measured using a plate reader (Synergy Neo2, BioTek, Winooski, VT) with an excitation wavelength of 485/18nm and an emission wavelength of 535/26nm to enable measurement of assay fluorescence, with the plate reader delivering maximum energy of 25mJ/cm^2 per reading for the excitation.

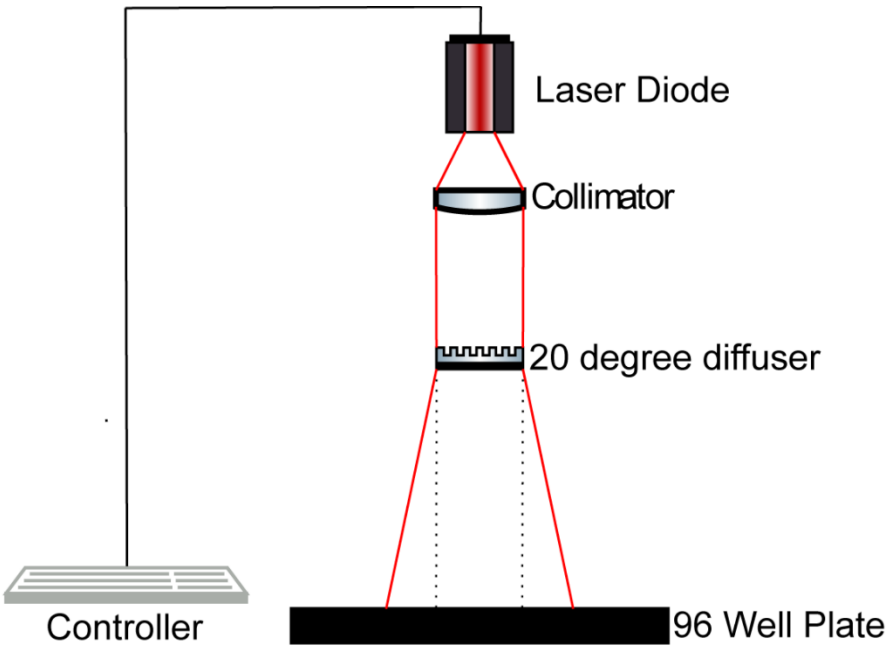

Figure 2.1: Exposure System
Schematic of the optical exposure system. A laser diode is collimated with a f = 50mm convex lens. The collimated beam passed through a diffuser to create a top-hat beam profile and thus provide uniform irradiance across the 96-well plate.

2.2.5 Phototoxicity assay procedure

Before proceeding to measurement trials, the concentration of the dilutions were all tested for accuracy using an absorbance measurement, where concentration was calculated using known molar extinction coefficients. Samples were either accepted or remade to correct any errors. The laser system was set to the appropriate irradiance level (Table 2.2) and verified using a power meter (model PMD100D,

Thorlabs, Inc., Newton, NJ). A volume of 165µL of the fluorophore of interest at 2x the desired concentration was mixed with 165µL of 14µM SOSG dissolved in DI water in a 96-well plate, resulting in a mixture of 7µM of SOSG and the exact desired concentration of the fluorophore of interest. This mixture was prepared with 5 - 6 replicates depending on the amount of evenly distributed light that can be exposed onto the plate for each given laser and its required irradiance. Three wells were filled with the fluorophore and assay mixture, but these would be covered to avoid exposure to the laser and serve as a dark, negative control. Three more wells were filled with DI water to serve as a blank. These were all placed on the edges of the plate and covered with foil. Controls included three wells that are one-part DI water and one part the fluorophore of interest, measured at the same excitation and emission wavelengths as SOSG. This control aided in the quantification of the cross-talk between the SOSG probe measurement and the fluorophore of interest, with the results in Figure 2.6c. The 96-well plate was initially read with no laser excitation. After the initial reading, the 96-well plate was illuminated to achieve the desired H_e, then it was again measured by the plate reader. When the plate was not being illuminated or measured, it was shielded from any ambient light. This process was repeated at pre-determined intervals until the maximum H_e was reached. To assess repeatability, every concentration of each fluorophore was repeated four to six times. A diagram of the process is shown in Figure 2.2.

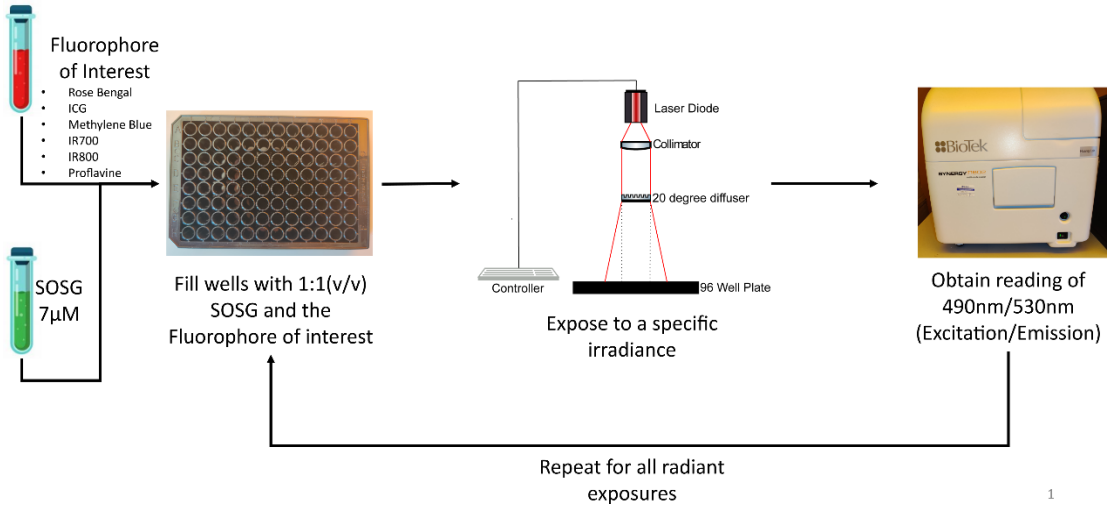

Figure 2.2: SO Assay Procedure

Schematic of procedure used to determine assay fluorescence levels for each sample. The fluorophore of interest (at a specific concentration) and assay were mixed in a well plate, exposed to clinically relevant laser illumination, then measured in a plate reader. Exposures and measurements were then repeated at all designated H_e values and fluorophore concentrations.

2.2.6 Data analysis

Fluorescence signals collected for a given concentration of a fluorophore were normalized using the formula below:

$$\boldsymbol{Normalized\ FL_{SOSG}} = \frac{\left(\boldsymbol{FL_{SOSG+Fluo.(Exp):H_e}} - \boldsymbol{FL_{SOSG+Fluo.(Dark\ Control):H_e}}\right) - \left(\boldsymbol{FL_{SOSG+Fluo.(Exp):0_J}} - \boldsymbol{FL_{SOSG+Fluo.(Dark\ Control):0_J}}\right)}{\boldsymbol{FL_{SOSG}}}$$

(1)

Where $FL_{SOSG+Fluo.(Exp):He}$ is the fluorescence intensity of the SOSG probe and fluorophore at the specific H_e, $FL_{SOSG+Fluo.(Dark\ Control):He}$ is the corresponding dark control at the same H_e equivalent time (since they are not exposed to excitation light), $FL_{SOSG+Fluo.(Exp):0J}$ and $FL_{SOSG+Fluo.(Dark\ Control):0J}$ is the experimental and control fluorescence at 0 J/cm^2 and FL_{SOSG} is the average fluorescence intensity of SOSG alone. The mean and standard deviation were calculated and graphed as a function of

H_e. This was repeated for each fluorophore concentration. The results from the repetitions were averaged to generate a final plot with variance represented by error bars. The slope of each of these lines was found using linear regression and setting the y-intercept to 0. When performing the linear regression, the R^2 value should be greater than 0.96 if the peak normalized fluorescence value for the highest concentration is above 1. If the R^2 values are below 0.96, the highest H_e value should be dropped, and the R^2 recalculated. If the peak normalized fluorescence value is below 1, then the R^2 value threshold can be dropped to 0.93 due to a loss of sensitivity of the assay at lower fluorescence values. We then plotted the calculated slope against the concentration, giving the SO production rate. This allowed all fluorophores to be viewed together in one figure (Figure 2.5). The SO production factor is then derived by taking the slope of the SO production rate vs concentration. The three wells that served as negative controls were also plotted in the same manner as the experimental data and then subtracted from the experimental data.

All data were plotted and analyzed using the graphing software PRISM (San Diego, CA) and were plotted using standard error mean.

2.3 Results

Figure 2.3 shows the normalized absorption and emission spectra of the assay and other fluorophores used in this study. SOSG assay absorption and emission peaks are seen at 490nm and 530nm, respectively. For most of the fluorophores tested, there is minimal crossover in excitation and emission with the assay. The exception to this

is Proflavine, which has considerable overlap with the assay in both excitation and emission wavelengths.

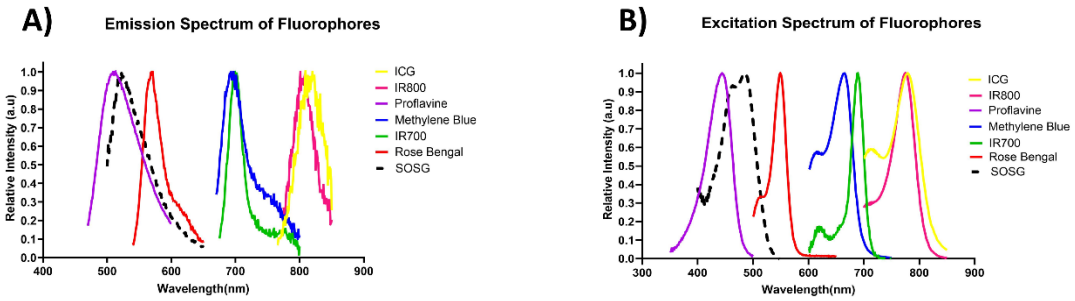

Figure 2.3: Excitation and Emission of Probes
Peak-normalized graphs of a) excitation and b) emission wavelengths of the fluorophores used in the study as well as the SOSG probe.

In Figure 2.4, we present assay fluorescence as a function of H_e for all the fluorophores used in this study. For products incorporating two of the imaging agents, IR800 and ICG, modest increases in assay fluorescence with H_e are apparent, yet the maximum normalized fluorescence level was very low, in the 0.2-0.6 range. These agents also demonstrate minimal correlation with concentration. For example, although ICG and IR800 assay fluorescence does increase with H_e, there is no difference in fluorescence across concentrations. Proflavine also shows an increase in fluorescence with H_e, yet a decrease in fluorescence with concentration is also shown. The remaining three fluorophores – Rose Bengal, Methylene Blue, and IR700 – produced a strong fluorescent signal, indicating strong production of SO. The fluorescence increase with respect to H_e is linear, demonstrating a linear relationship between the level of H_e and SO production. In addition, the slope increases in a linear manner with concentration (further explored in Figure 2.5). While the maximum normalized fluorescence produced for these cases ranged from 3 to 11, several of the lower concentration/exposure scenarios produced values less than 1.

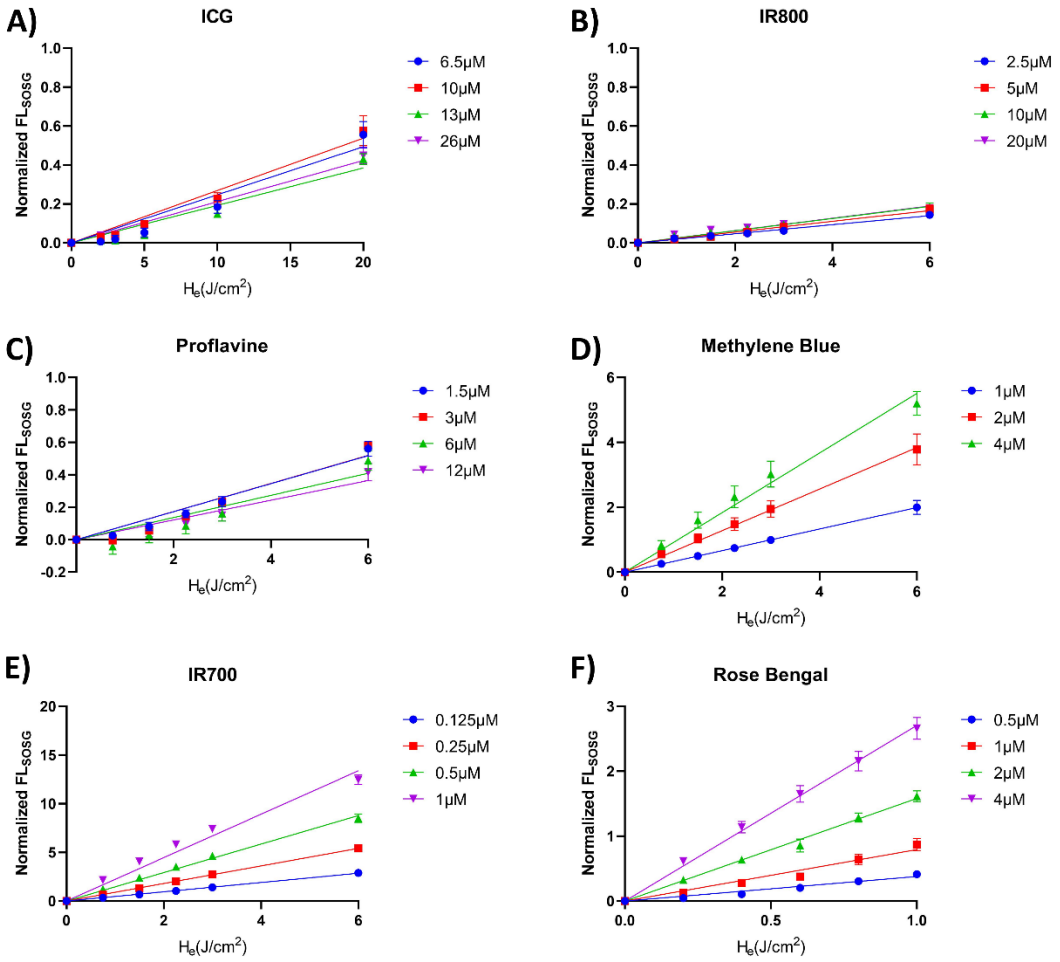

Figure 2.4: **Normalized SOSG Fluorescence at various H_e's**
Effect of He and fluorophore concentration on SOSG assay fluorescence intensity for: a) ICG, b) IR800, c) Proflavine, d) Methylene Blue, e) IR700, and f) Rose Bengal.

A graphical summary of results from all fluorophores tested is shown in Figure 2.5. These results demonstrate the dependence of SO production on the type and concentration of fluorophore, as well as H_e. Because the values in Figure 2.5 are taken from the slopes of the plots generated in Figure 2.4, the units in Figure 2.5 are in units of fluorescence divided by H_e, which we will refer to as the SO production rate. Due to the normalized fluorescence being unitless, the SO production rate has units of cm^2/J. The products tested fell into two groups based on their SO production

levels. Higher SO-generation products included those using Rose Bengal, Methylene Blue, and IR700, while products that exhibited relatively low SO production rates were ICG, IR800, and Proflavine. In Table 2.3, we present SO production factors, determined from the slopes of the SO production rates in Figure 2.4. The result was compared to previously determined values of SO quantum yield from the literature. SO quantum yield is defined as the amount of SO produced per photon absorbed, so the value is always between 0 and 1 [103, 104]. In Table 2.3, green shading indicates fluorophores with low SO production factors and SO quantum yields, while red shading indicates fluorophores with relatively large SO production and quantum yields. Yellow indicates inconclusive results for reasons that will be addressed in the discussion section. It is also worth noting that a potential discrepancy between the SO production factors and SO quantum yield exists.

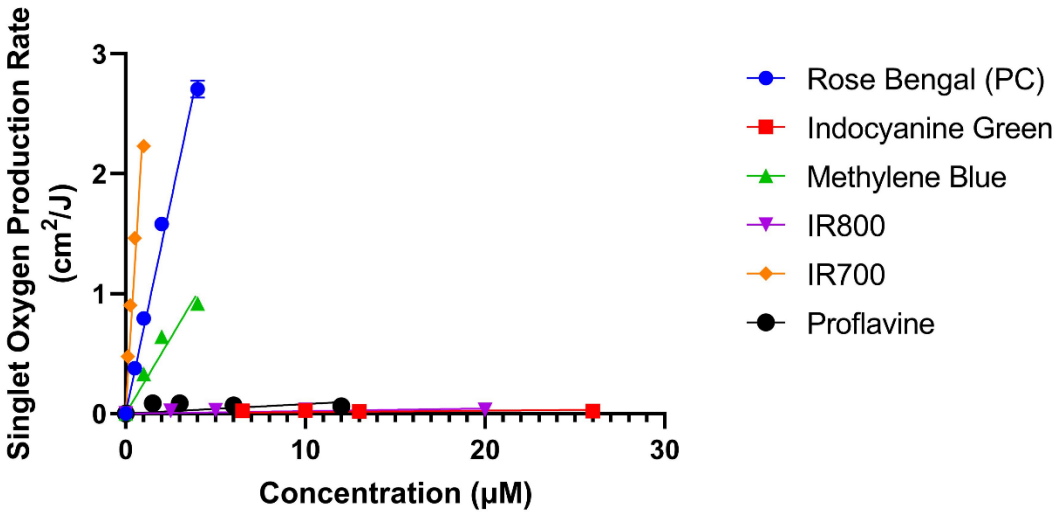

Figure 2.5: **SO Production Rates**
Summary of SO production for all agents tested. SO production rate values represent the mean slopes of the data from Figure 2.4 of the different fluorophores at their various tested concentrations. Linear regression was performed to obtain SO production factors (Table 2.3).

Table 2.3: **SO production factors of the different probes tested**
Singlet oxygen production factor determined from the slopes in Figure 2.5. These numbers were also compared to literature values of SO quantum yield. Highlighting in this table corresponds to low SO producing fluorophores (green), high SO producing fluorophores (red), and inconclusive (yellow).

Fluorophore	**SO Production Factor [(F/H_e) / µM]**	**SO Quantum Yield**
ICG	0.0012±0.0002	0.077 **[105]**
IR800	0.0021±0.00024	-
Proflavine	0.0080±0.0014	0.12 **[105]**
Rose Bengal	0.70±0.01	0.76 **[105]**
Methylene Blue	0.25 ±0.01	0.51 **[105]**
IR700	2.44±0.08	0.30 **[106]**

Most of the products demonstrated a linear trend in F/H_e vs. concentration. However, as shown in the SO production plots for a,) Methylene Blue and b) Proflavine (Figure 2.6), Methylene Blue demonstrated a linear response up to 4µM, after which the rate plateaued and started to decrease. Proflavine results were unique due to the decreasing SO production rate found. In addition to having a non-linear response, proflavine also demonstrated a large amount of crosstalk with the SOSG excitation and emission wavelengths, especially when compared to all the other fluorophores that were measured during this study, as seen in Figure 2.6c.

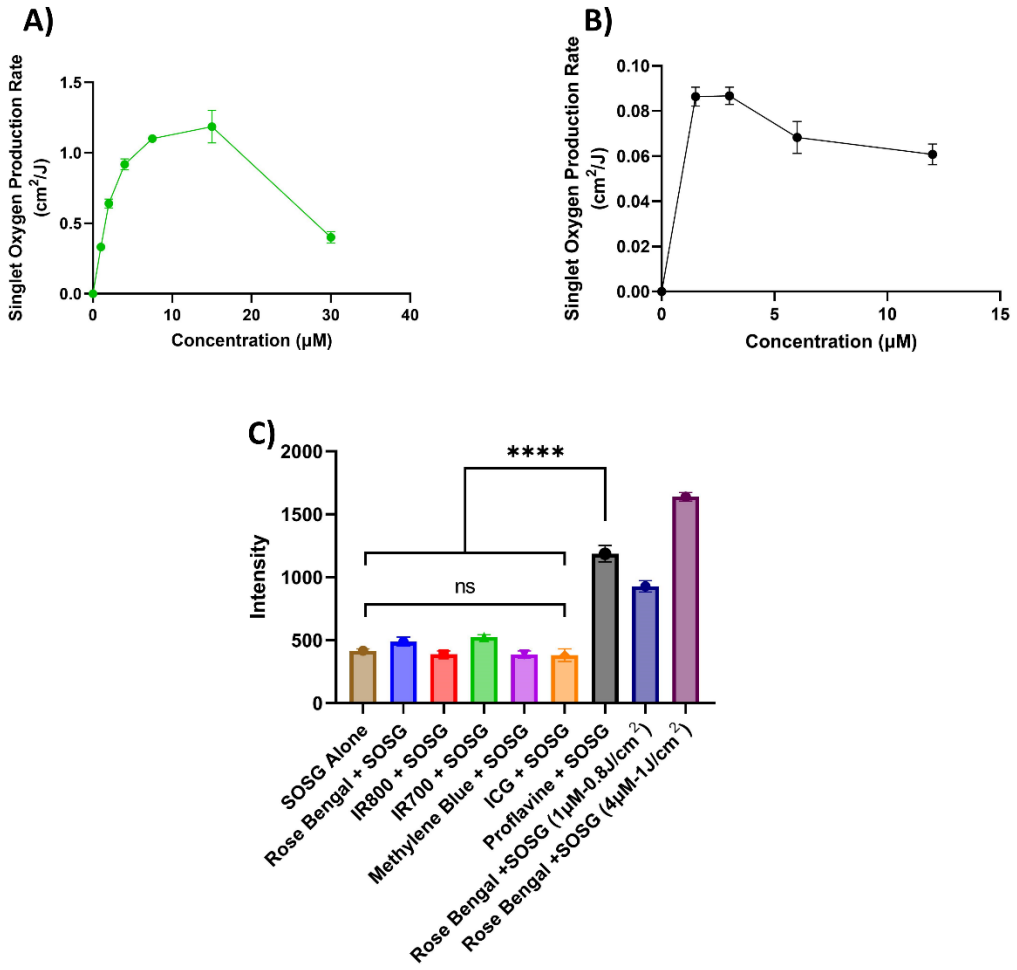

Figure 2.6: **Nonlinear production rates and cross talk**
Non-linear SO production rate plots for a) Methylene Blue and b) Proflavine. Figure 2.6c demonstrates the reading at 0J for the different fluorophores tested at the excitations/emission of SOSG, the SO signal produced by Rose Bengal, and SOSG at the Normalized FL_{SOSG} threshold of 0.6 (concentration of 1μM, $H_e = 0.8J/cm^2$ for Rose Bengal), and the signal produced by a high-SO generator, in this case, Rose Bengal at a concentration of 4μM and a H_e of $1J/cm^2$.

2.4 Discussion

2.4.1 Overview

In this study, the main goal was to assess the potential for developing an effective and reliable approach to quantify the SO produced by fluorescence products based on an established commercial assay. Our method was able to quantify the

amount of SO produced by fluorophores at a specific concentration and excitation wavelength relevant to the clinical environment it will be used in, which produces important information about the potential phototoxicity of the fluorophore of interest.

2.4.2 Phototoxic potential of tested products

Overall, our results indicate that we can measure and compare the potential SO production of fluorophores at clinical radiant exposure and irradiances. In Figure 2.4, results demonstrate that at the highest concentrations and H_e's, ICG and IR800 show peak normalized assay fluorescence values below 0.6, whereas the positive control Rose Bengal, as well as Methylene Blue and IR700, generated values between 3-10 for the highest concentrations and H_e's. The threshold between low and high SO was established based on the highest normalized fluorescence value produced by ICG, a contrast agent with a long history of safe clinical use. Because ICG is not known to cause phototoxic damage at clinically relevant H_e's, and concentrations, values below its peak normalized FL_{SOSG} of 0.6 (seen in Figure 2.4a) can be deemed as having low SO-toxicity. Values that fall above this threshold can then be classified as potentially producing SO toxicity. From the data in Figure 2.5, we calculated the SO production factor for each agent and compared them to the SO quantum yield values published in the literature (Table 2.3). Figures 2.4 and 2.5 indicated that ICG and IR800 exhibited much lower phototoxic potential than the other three agents. It is worth noting that for agents with higher phototoxic potential, using low H_e and/or concentration combinations could minimize SO generation levels to a point where potentially safe exposures can be performed if the normalized FL_{SOSG} values fall below 0.6. In Figure 2.5, while changes in SO production were dose-dependent for these agents, ICG's SO

production rate was always under 0.04, and for IR700 the SO production rate was above 0.4, even at the lowest concentration tested of 0.125μM. These findings seemed to indicate that increased drug or light doses would not significantly impact the phototoxic potential of products incorporating these agents, although additional studies at higher doses would be needed to confirm this behavior.

Additional support for our finding that the tested agents tended to fall into either a high or low SO-generating category can be found in the literature. The agents which had high SO production factors have been used as photo-therapeutic agents, including Rose Bengal as a light-activated anti-microbial agent in prior studies [97] and IR700 as a photodynamic agent to treat head and neck cancer (NCT02422979). Methylene Blue is used as a white light contrast agent during gastrointestinal chromoendoscopy procedures to enhance the detection of neoplastic lesions [107]. It has also been used as a fluorescent agent to image the uterus [51], thyroid [108], and pancreas [109]. Despite this clinical history, our results and previous literature indicate that Methylene Blue can generate significant quantities of SO, with adverse impacts ranging from patients developing skin rashes [110] to the death of preterm neonates [111, 112]. In addition, Methylene Blue is likely the source of the DNA damage documented in Barrett's esophagus noted in prior studies [77, 113]. Although our study did not explicitly address the drug and light doses involved in this study, SO production is likely a factor, which may be of particular concern given the metaplastic/precancerous state of this tissue.

The two agents found to have the lowest SO-generating potential – ICG and IR800 – are primarily used as imaging agents. ICG has been extensively used for

retinal angiography [114], vascular neurosurgery [115], and more recently, lymphatic imaging [98]. Both ICG and IR800 have been used to aid in fluorescent-guided resection [92, 116]. We are not aware of significant clinical evidence of phototoxicity with either of these agents, with studies demonstrating ICG's efficacy and safety for use in lymph node dissection [117] and clinical trials using IR800 demonstrating no serious adverse side effects in clinical imaging trials [93]. Thus, it is likely that the fluorescence assay readings produced during the testing of these agents also represent safe levels. However, it is worth noting that a prior study has indicated that ICG produces SO that rapidly oxidizes the ICG molecule, leading to decomposition and formation of cytotoxic components [118].

The SO production factors shown in Table 2.3 are derived from the SO production rates in Figure 2.4 by taking the slopes of the concentration vs the SO production rate. Because of this, the SO production factor is dependent on concentration and H_e, having the units of $cm^2/J*\mu M$. In addition, the SO production factor is still dependent on several other variables, such as the oxygen level in the surrounding region and the imaging excitation wavelength (which can also include the spectral bandwidth effect, such as using LEDs vs lasers). The SO production factor can be thought of as an easy way to compare the SO potential of different fluorophores under their own independent clinical conditions.

As noted in the results section, our SO production factor data shows only a moderate degree of quantitative correlation with published SO quantum yields. One possible reason is that the SO quantum yield is independent of environmental factors since it only takes into account the likelihood of generating SO if the compound has

already absorbed a photon. One example would be that Rose Bengal has a larger SO quantum yield than IR700, but the reverse is true when comparing SO production factors. But, by looking at the absorbance fraction of the fluorophore at the wavelength used to excite the fluorophore (520nm/685nm for Rose Bengal/IR700 respectively), we can see that the absorption fraction for Rose Bengal was 0.33, and for IR700 the absorbance fraction was 0.93. This difference in absorbance is one key factor that could explain the differences between the SO production factor and SO quantum yield.

2.4.3 Potential method limitations

Since the SOSG assay is based on visible wavelength fluorescence, it is not unexpected that there would be an inherent limitation due to interference from test fluorophores that are active in this range. The assay incorporates a fluorescein-based dyad [20, 21] and thus has the same excitation and emission as fluorescein (485nm/535nm respectively). In our study, the effect of optical interference is seen in the test for Proflavine. Although Proflavine exhibited substantial cross-talk with the assay when measured with a plate reader (Figure 2.6c), our current method takes into account cross-talk effects by implementing a background subtraction using unexposed measurements of fluorophore-only control samples and assay-fluorophore mixtures. By implementing this simple correction approach, we were able to effectively mitigate the presence of Proflavine cross-talk and establish that for the concentrations and radiant exposures used, SO production was low. If Proflavine were to have produced significant SO, the level of increase in assay fluorescence should have been detectable, based on the change in SOSG signal produced by Rose

Bengal at higher drug/light doses. However, if higher concentrations of Proflavine were used or another fluorophore with higher fluorescence yield, the level of cross-talk and variability in detected signals might increase to the point where results would be compromised regardless of the correction approach.

An example of a way to determine if the cross-talk variance is too large is to compare the variance of the cross-talk value at $0J/cm^2$ to the fluorescence intensity produced by SOSG at the High/Low-SO threshold. This threshold can be seen in Figure 2.6c, looking at the fluorescence produced by Rose Bengal and SOSG at a concentration of 1μM and H_e of $0.8J/cm^2$ (this is similar to the normalized FL_{SOSG} value of 0.6). If the cross-talk increases the variance to the point that there is no significant difference between no generation intensity and this threshold value, the cross-talk might be too large to draw conclusive results from the assay. In addition, users should be aware of the potential for shielding if a fluorophore of interest has an overlapping absorbance spectrum with SOSG emission. The test fluorophore could potentially absorb the SOSG signal, leading to erroneously low estimates of SO.

Another unusual result is that of Methylene Blue SO production. After initially increasing linearly with concentration up to 4μM, assay fluorescence abruptly plateaued, then decreased above 7.5μM. Unlike the proflavine result, there is little to no interference caused by SOSG and Methylene Blue, as in Figure 2.6c we can see that Methylene Blue creates very little cross-talk in the SOSG channel. This means that the issue is likely not the assay itself. A possible reason for the plateau could be specific to Methylene Blue, as studies have shown that it can be converted to the non-fluorescent compound Leucomethylene due to pH and concentration changes.

A study by Matsui et al. found that in PBS, Methylene Blue fluorescence increases with concentration up to 7.5μM, then decreases with concentration [91]. Since SO production is tied to the mechanism that causes fluorescence, factors that affect Methylene Blue fluorescence can affect SO production.

2.4.4 Implications for phototoxicity evaluation

Our findings provide evidence that when implemented according to a standardized set of best practices, it may be possible to use commercially available assays to screen fluorescence probes for photochemical safety/efficacy. With our methodology, researchers can quickly identify the SO production rate by a probe under expected clinical conditions, using cost-effective materials and equipment available in most labs. Benchmarking optical measurements against well-established fluorophores such as Rose Bengal and ICG may also help to optimize consistency in test outputs.

Initially, it is critical to identify the relevant fluorophore concentration range and H_e. The identification of exposure levels that significantly exceed the clinical values can be used to provide a factor of safety. The fluorophore illumination, source irradiance and exposure duration can typically be adjusted to achieve the appropriate H_e. As long as thermal and multi-photon effects are avoided, photochemical effects are not highly time-dependent (except possibly under conditions of transient environmental conditions). However, it should also be noted that the H_e levels implemented in cell-free assays may need to be greater than clinical exposure levels to account for the true maximum fluence levels that cells would be subject to in turbid

biological tissue. As prior studies have shown, subsurface fluence levels can greatly exceed H_e levels due to tissue scattering/backscattering and resultant isotropic propagation of light [119, 120]. The cell-free assay approach studied here may obviate the need for cellular and *in vivo* phototoxicity testing in many fluorescent products. However, if initial tests demonstrate a high level of SO generation (a value above 0.6 for the derived normalized SO fluorescence generation), the product would be considered potentially phototoxic, and additional testing would be required with more involved methods, such as an *in vitro* photo-cytotoxicity assay. While the current study focuses on the detection of singlet oxygen, an RMS generated through type 2 reactions, other assays will be needed to detect other RMS produced by type 1 reactions, such as hydroxyl radicals and superoxides. These assays will form the basis of a comprehensive test method. By quantifying other key RMSs, a more thorough understanding of a product's phototoxic potential will emerge.

Our future work will focus on two primary needs: 1) cell-free assays to quantify other RMS that can be produced by fluorescent probes and 2) assays to quantify photo-cytotoxicity of agents that have been shown to produce significant RMS. By developing a battery of simple tests to assess phototoxicity, we can provide a least burdensome approach to help ensure patient safety and encourage innovation in developing imaging/ phototherapeutic fluorophores for a variety of clinical applications.

2.5 Conclusion

In this study, we have developed and evaluated methods based on a commercial cell-free assay for assessing the potential of imaging/ phototherapeutic fluorophores to generate SO under clinical conditions. Our findings on light/drug dose-response of several well-known fluorophores align well with limited published data available on SO production and phototoxic effects of these agents. While spectral overlap of the assay and fluorophores may impede the effectiveness of this approach, initial results indicate that our method can be largely robust to these challenges under certain conditions. Overall, this study provides evidence of the potential of approaches based on commercial assays as screening methods for fluorescent compounds' potential phototoxicity.

Chapter 3: Determination of Photosensitizer Activation Depth in the Brain‡

3.1 Introduction

As mentioned in section 1.2.1, PDT is a photochemistry-based treatment modality in which a biologically inert agent is activated by the application of light at specific wavelengths into a cytotoxic therapeutic (i.e., photosensitization). The fluorescent signal generated from the excited state photosensitizer can also be harnessed for tumor imaging and fluorescence-guided surgery (FGS) [67, 121, 122], with one example being PpIX. Upon excitation with ultraviolet/blue light (375-440nm), gliomas that contain the 5-ALA-induced PpIX emit a violet-red fluorescence, which can be readily visualized for resection. In 2017, the US Food and Drug Administration (FDA) approved 5-ALA (Gleolan®) for use as an intraoperative imaging agent in patients with suspected high-grade gliomas [123].

PDT is being evaluated in clinical trials for patients with brain cancer (e.g., NCT03048240, NCT03897491, NCT00003788, NCT01966809, NCT00002647, NCT01682746). Glioblastoma multiforme (GBM) is the most common and lethal adult primary brain cancer, and the median patient survival continues to be less than 18 months despite major advancements in our understanding of GBM biology and efforts to develop new therapeutic strategies [124]. A single PDT dose has been

‡ Part of the contents in this chapter were reproduced from C. Inglut, B. Gaitan, et al., "Predictors and Limitations of the Penetration Depth of Photodynamic Effects in the Rodent Brain", *Photochemistry and Photobiology* 96(2), 301–309, 2020 with permission.

shown to add up to 3-18 months to the lifespan of GBM patients [125]. Optimized light delivery for effective PDT can be achieved through intra-operative, endoscopic, or balloon catheter-based fiber optics. The combination of FGS and PDT using different types of photosensitizers (e.g., BPD, 5-ALA, Photofrin®, temoporfin, and hematoporphyrin derivative) have substantially improved survival outcomes in GBM patients [121]. In a small-scale study, the mean survival of GBM patients was increased from 24.6 to 52.8 months when PDT was combined with FGS, compared to surgery alone [126]. We and others now believe that the most advantageous, safe initial application of PDT is following tumor resection while in the operating room and prior to the standard of care chemoradiation therapy [127]. However, long-term survival has not been achieved due in part to the limited light penetration in brain tissues, as well as the poor selectivity and delivery of the appropriate photosensitizers.

Light penetration effects due to tissue optical properties are one of the most important factors when it comes to PDT activation, and light dosing [128] as a tissue's optical properties will affect how deep into the tissue you can activate and be effective at treating tumor tissue. Many studies have looked at the potential penetration depth of different wavelengths of light, finding, for example, that red light penetration depth is typically 0.1-0.3cm in tissues, with light penetration being defined as when the incident energy drops to 1/e [129]. Although light penetration is limited to these distances, the remaining fraction of 37% can be used to activate a photosensitizer enough to potentially extend the activation depth, with *in silico* studies demonstrating that photosensitizers can potentially penetrate 2-5cm into tissue [130-136]. Studies have also demonstrated that a 630nm light could activate a

hematoporphyrin derivative enough to cause cell killing and even tumor necrosis 0.8-1.5cm into the brain [137-139].

With the activation depth of photosensitizers being such an important factor in PDT treatment, it is very important to understand and compare the penetration depth of various fluorophores. For example, one study found that when PpIX was activated with a 630nm light, cerebral tissue damage was only seen up to 0.4cm in depth [140]. Another potential photosensitizer that has been investigated is BPD, a compound that has been FDA approved (as Visudyne®) for patients suffering from wet age-related macular degeneration [141, 142] and has undergone clinical trials to treat brain tumors (NCT00002647) [143]. Because BPD has an activation wavelength of 690nm, it might be able to activate deeper in tissue if used to treat GBM, which could potentially lead to a more effective treatment modality compared with using PpIX as a PDT agent for GBM.

In this chapter, we look to 1) compare and contrast the potential activation depth of BPD and PpIX in the rodent brain using clinical irradiances/radiant exposures and 2) develop a method to compare photosensitizer activation depth.

3.2 Methods

3.2.1 Characterization of BPD and PpIX

PpIX and BPD were both inserted inside liposomes to create nanoliposomal (Nal) PpIX and BPD to increase the stability of the compounds since aggregation can occur with these compounds *in vitro* [144-146]. To create the Nal-PpIX and Nal-

BPD, a freeze-thaw extrusion method was used as described in previous publications [147-151]. The fluorescence-based optical characterization of BPD (Ex/Em: 435/600-800nm) and PpIX (Ex/Em: 405/600-800nm) was determined using a multi-mode microplate reader (Synergy Neo2, BioTek, Winooski, VT). BPD and PpIX were diluted to 5μM for all absorbance and fluorescence measurements in DMSO. SO production was monitored indirectly using the probe SOSG. Within 96 well plates (black wall, transparent base), BPD or PpIX were mixed with SOSG (Thermo Fisher Scientific, Eugene, OR) to a final working solution of 0.5μM of photosensitizer and 25μM of SOSG in PBS. Samples were irradiated with 635nm light (100mW/cm^2) for PpIX and 690nm light (100mW/cm^2) for BPD at a radiant exposure range of 0-40J/cm^2 (ML6600 series laser module with 635nm and 690±5nm lasers with 1.5W output power each. SMA fiber output with SMA905 connector, Modulight, Tampere, FI). Fluorescence intensities of SOSG (Ex/Em: 504/525nm) were acquired using a Synergy Neo2 microplate reader prior to and following irradiation.

3.2.2 Photobleaching of photosensitizers in *ex vivo* rat brains

Glass capillaries (300μm in diameter; 1cm in length) filled with 5μM of BPD or PpIX were inserted in Sprague Dawley rat brains (Innovative Research, Novi, MI) at varying depths (0-2cm). Brain tissues were then illuminated on the surface using red light (635nm, for PpIX) or NIR light (690nm, for BPD) at a fixed irradiance of 100mW/cm^2 and with radiant exposures of 10J/cm^2 and 40J/cm^2 using a diode laser (ML6600, Modulight, Tampere, FI). After light illumination, capillaries were removed, and the fluorescence emission from BPD (or PpIX) was measured by placing the capillaries on a flat black surface to minimize reflectance. Fluorescence

images were acquired using a reflectance fluorescent microscope equipped with a 375nm laser diode (L375P70MLD, Thorlabs, Newton, NJ). The light from the laser was then collimated, with 6mW of light arriving on the sample. The emitted fluorescence and scattered light were then collected through another objective lens. The fluorescent and scattered light then passed through a 710nm filter (FF01-710/40-25, Semrock, West Henrietta, NY). The remaining filtered fluorescent light was collected by a 12-bit CCD camera (EM-CCD, PCO Imaging, Kelheim, DE). All images were processed using ImageJ software (NIH) [152]. Results are mean ± standard error of the mean. Statistical tests were carried out using GraphPad Prism (San Diego, CA). All experiments were carried out at least in triplicate.

3.3 Results and Discussion

3.3.1 Characterization of BPD and PpIX

Figure 3.1 demonstrates the absorption and emission spectra of BPD and PpIX. With BPD, we can see that there are two large absorption peaks, with a major peak at a lower wavelength at 430nm and another peak at 690nm, with the fluorescent peak being seen at 700nm. PpIX shows a major absorption peak at 405nm, with other smaller absorption peaks at 505nm, 540nm, 575nm, and 630nm, as well as demonstrating fluorescent peaks at 630nm and 700nm.

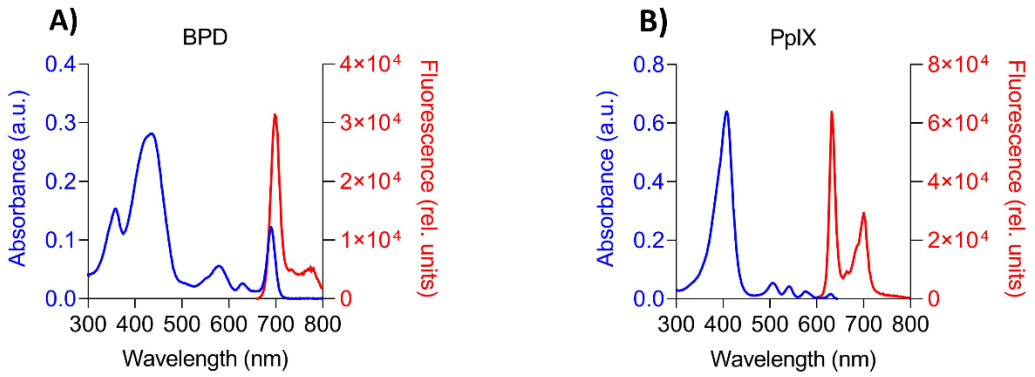

Figure 3.1: Absorption (blue)and emission (red) spectra of BPD and PpIX
a) BPD has a strong absorbance peak at 435nm and 690nm. BPD also has a peak emission in the NIR range (λ_{max} at ~700nm). b) PpIX shows a strong absorbance peak at 405nm, with multiple absorption peaks in the green to red range. The fluorescence signal emitted by PpIX is in the red/NIR range between 635 and 700nm.

Light activation of photosensitizers could result in type 1 and/or type 2 reaction products [153]. Under normoxic conditions, type 2 photosensitization is the dominant process in BPD-based PDT and PpIX-based PDT, which produce highly reactive SO that confers toxicity to nearby targets [153]. It is well-established that the SO quantum yield of BPD ($\Phi\Delta$= 0.86) is significantly higher than that of PpIX ($\Phi\Delta$= 0.56) [154-157]. Here, using the SOSG fluorescent probe, we test if 690nm light activation of BPD could produce SO more efficiently compared to 635nm photo-activated PpIX. Upon light activation, the SOSG fluorescence intensity generated by BPD was markedly higher than that generated by PpIX and in a light fluence dependent manner (Figure 3.2a). This data indicates that BPD produces SO more efficiently than PpIX upon light activation under our experimental conditions. It is important to note that the higher SO production rate of BPD does not necessarily translate into more pronounced toxic effects, as the phototoxicity of the photosensitizer depends on the specific parameters, such as pharmacokinetics,

biodistribution, cellular uptake, and subcellular targets of the photosensitizer, as well as the tumor microenvironment [153, 158, 159].

3.3.2 Depth dependent photodynamic effects of BPD and PpIX

When a photosensitizer releases RMS, photochemical reactions can occur, causing damage and/or covalent modifications to the photosensitizer itself, leading to a loss in fluorescence. Measuring the fluorescence decrease as the photosensitizer is photobleached is one of the most common ways to monitor dosimetry in preclinical and clinical settings [160-163] since SO is known to alter the original confirmation of certain photosensitizers such as PpIX, leading to less fluorescence being generated as more SO is produced [164]. To determine the effective penetration depth of the investigated photosensitizers, we monitored the loss in fluorescence as the respective photosensitizer is photobleached due to laser irradiation. As mentioned in section 3.2.2, capillaries with either BPD or PpIX were inserted into the rodent brain. After laser irradiation, the photobleaching was measured by comparing the fluorescence of the irradiated capillaries inserted into the brain to a negative control that was not exposed to any laser irradiation. In Figure 3.4a/b, we can see that the deeper the photosensitizer is in the brain relative to the source, the lower the level of photobleaching. BPD demonstrated up to 5-20% photobleaching between 1-1.5cm, while with PpIX almost no photobleaching (0-1%) could be observed 1cm into the brain tissue (see Figure 3.3), which is supported by previous findings [165, 166]. For example, photofrin, which is activated using 632nm light, was found to induce necrosis up to roughly 0.35cm in depth in rat brains [165]. In contrast, talaporfin,

which is activated using 664nm, caused measurable damage up to 0.8cm in clinical studies to treat gliomas [166].

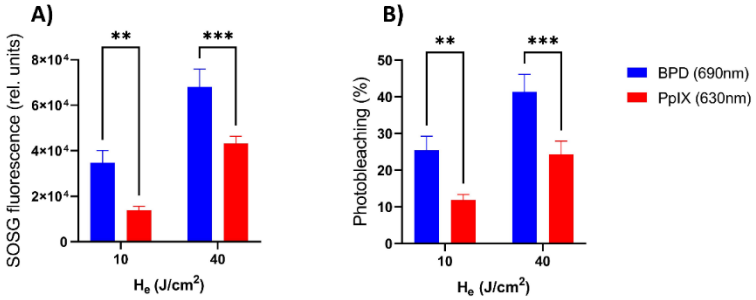

Figure 3.2: SO production and photobleaching of photosensitizers
a) SOSG fluorescence and b) percent photobleaching of BPD and PpIX. BPD was excited with 690nm light while PpIX was excited with 630nm light. Although we exposed the photosensitizer to various H_e's, the irradiance was kept constant at 100mW/cm^2.

In Figure 3.4a/b, we observed that the degree of photobleaching across different powers begins to converge as depth increases. This is because the loss of light intensity is non-linear. Simple 1-dimensional (1-D) modeling of light penetration has been described with the equation $\phi(z) = Eke^{-\mu z}$ [167]. Where $\phi(z)$ is the fluence rate (W/cm^2) dependent on z, which is depth (cm). E is the irradiance delivered on the surface of the tissue (W/cm^2), k is backscattered light that augments irradiance on the surface of the tissue, and μ is the attenuation coefficient (cm^{-1}). Looking at the 1-D approximation, one thing to take note of is that the amount of energy lost in the tissue is dependent on $e^{-\mu z}$, which shows an exponential decay in light intensity. Based on the above equation, it is expected that the photodynamic effect would be proportional to $\phi(z)$. Therefore, the depth versus degree of photobleaching should have shown an exponential decay. Looking at Figure 3.4a/b this is not the exact case. Instead, the overall trend demonstrated was a plateau followed by an exponential decay. The main factors involved in the observed trend

are due to the specular reflectance when the light hits the brain and the boundary condition of the air-brain barrier.

Light scattering in tissue has been defined as being anisotropic, specifically regarding forward scattering. The magnitude of scattering is defined as g, with values being between -1 (backscattering) and 1 (forward scattering). Tissue is shown to have a g factor of 0.9, which means that while most light is forward scattering, some of the light is scattered back [168]. This means that some light that has penetrated the tissue possesses the potential to be scattered back into the air. Air has been defined as having a refractive index of 1, while the brain has a refractive index of 1.36 [169]. Because of the mismatch in refractive index, some of the light that gets backscattered to the air-brain barrier will get reflected into the brain rather than escape back into the air due to internal reflection. This is based on the angle at which the scattered light approaches the air-brain barrier. The angle at which light will be internally reflected is based on the equation $n_1 sin(90) = n_2 sin(\theta_c)$, where n_1 is the refractive index of air, n_2 is the refractive index of brain tissue, and θ_c is the critical angle. Therefore, any backscattered light that hits the air-brain barrier at a 47.3-degree angle will be reflected back into the brain. This, coupled with the fact that a small amount of light gets reflected when the light first hits the brain, signifies that for around 0-0.2cm of the light initially penetrating the brain, the fluence will increase slightly as depth increases [120, 170, 171]. As the light penetrates farther into the brain, the light will start to demonstrate the typical exponential decay pattern. Due to the depth intervals taken, the photodynamic effect was not measured between 0-0.2cm, meaning that the

initial increase in fluorescence cannot be seen in Figure 3.4a/b. The effect instead manifests itself as an initial plateau, proceeded by an exponential decay.

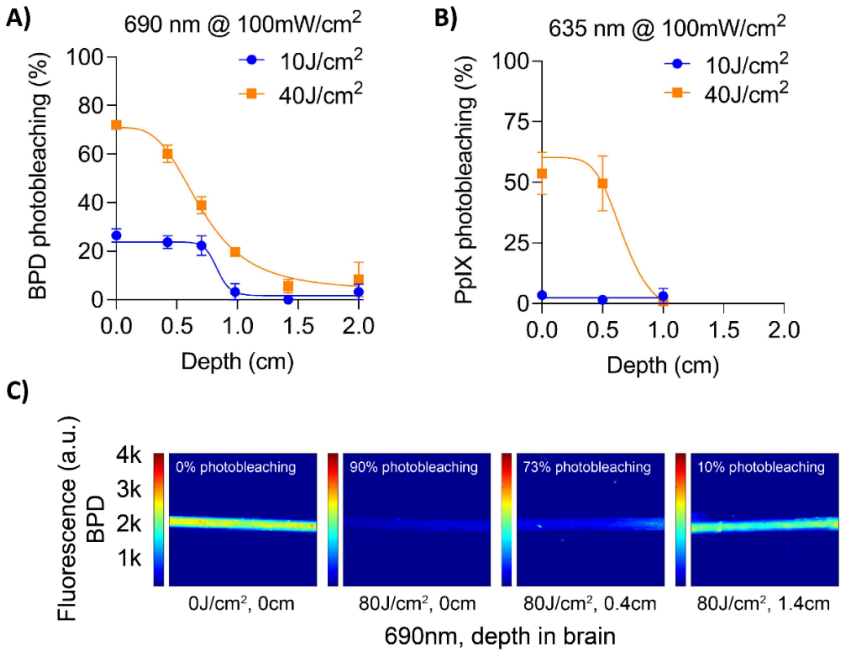

Figure 3.3: Photobleaching of photosensitizers in the rodent brain
Photobleaching plots of a) BPD and b) PpIX as a function of depth (cm). Photosensitizers were exposed to an irradiance of either 10J/cm^2 or 40J/cm^2. BPD was activated with a 690nm wavelength, while PpIX was activated with a wavelength of 635nm, and both were exposed to the same irradiance of 100mW/cm^2. Figure c) demonstrates fluorescent images of capillaries filled with BPD showing various levels at photobleaching at various depths.

The deeper penetration of BPD, when compared to PpIX, is expected, as the excitation wavelength is 60nm longer for BPD than for PpIX (630nm vs. 690nm respectively), with this shift leading to a drop in the reduced scattering coefficient (μ_s') by 40-50% [172-174]. In addition, we can see that BPD and PpIX have similar activation depths at 10J/cm^2 and 40J/cm^2, respectively, meaning that to reach the same penetration of 1cm, PpIX needs to be irradiated with x4 the energy as BPD. This can be explained by referencing the equation below [120] meant to model the maximum activation depth of a photosensitizer:

$$z_{rx} = \delta \ln\left(\frac{Etk}{H_{th}}\right) \quad (1)$$

With Z_{rx} being the depth penetration of the photodynamic effect, δ being the optical penetration depth in cm, t being the exposure time in seconds, and H_{th} being the minimum energy needed to activate the photodynamic effect (J/cm^2). By looking at equation 1, we see that increasing E and radiant exposure (E*t) only results in a logarithmic change in penetration depth. Alternatively, increasing the optical penetration depth, which can be done by using probes that are excited at wavelengths that undergo less tissue scattering, causes a linear increase in the maximum penetration depth. That means if you increase the optical penetration depth by x2, the penetration depth would increase by x2, but increasing the radiant exposure by x2 would only lead to an increase in penetration depth of x1.7.

While BPD shows greater potential for depth penetration and production of SO in deeper tissue, PpIX still has high utility due to the ability to be used as a visual guide for tumor removal. Figure 3.4 shows a comparison of two capillary tubes. The top capillary was filled with BPD, and the bottom capillary was filled with PpIX. Both samples were placed at similar heights, 0.04-0.05cm below the surface of the brain. The images were taken with a phone camera (OnePlus 5, Shenzhen, CN). Visual inspection of the capillaries shows that PpIX can be seen easier compared to BPD. This is likely due to the higher fluorescence quantum yield of PpIX (ΦF= 0.155) and its fluorescence at 630 nm, while BPD fluoresces at 700 nm with a much lower fluorescence quantum yield (ΦF= 0.051) [154-157]. Due to human spectral sensitivity, the emitted 630 nm light is seen with 10 times greater sensitivity than the 690-710 nm light, allowing for easier visualization of PpIX even with the same amount of energy being emitted [175].

In addition, it might be possible to extend the activation depth of PpIX or BPD. For example, X-rays penetrate deeper in tissue and, through the use of Cerenkov radiation [176] or nanoscintillators [177], can generate blue/red light to activate photosensitizers. Upconversion nanoparticles are another method to increase penetration depth through the use of NIR light to activate the nanoparticle, which can then generate blue/red light that can activate photosensitizers [178].

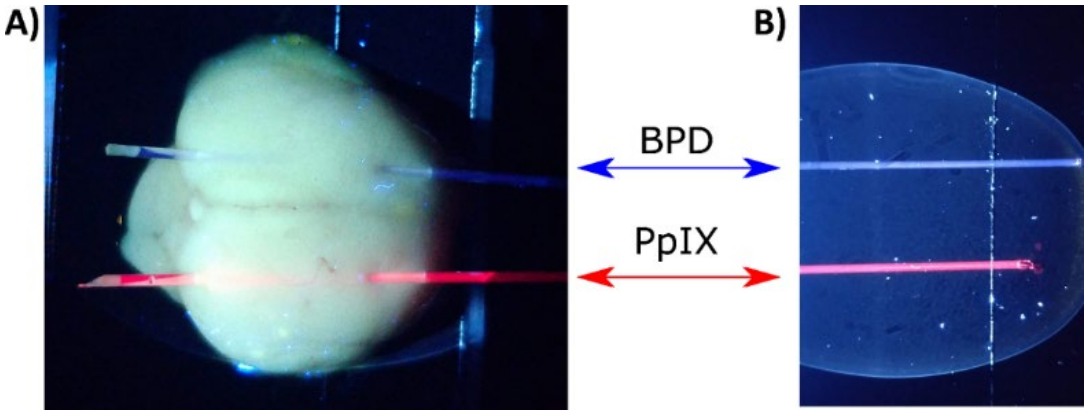

Figure 3.4. Color image of BPD and PpIX in a capillary
A color image of 300µm BPD and PpIX capillaries a) inserted 400-500µm deep into the rodent brain and b) the same capillaries being illuminated on a blank background. The capillaries were excited using a 375nm laser light.

3.4 Conclusion

Our results have demonstrated that the activation of BPD leads to the generation of SO, which in the rodent brain can lead to photobleaching up to 1.5cm into the brain at a radiant exposure of 40J/cm^2, which is a 50% increase in penetration depth compared to PpIX which has a maximal penetration depth of 1cm at the same radiant exposure. These results demonstrate the utility of BPD as a photosensitizing agent for GBM since recurrent brain tumors typically occur 1-2cm from the site of the original tumor [179-181]. In addition, this method can also be used to compare the potential penetration/activation depth of other potential photosensitizers.

Chapter 4: Depth Resolved Imaging of Photosensitizer in the Rodent Brain using Fluorescence Laminar Optical Tomography[§]

4.1 Introduction

Since Heimstaedt and Lehmann developed the first fluorescent microscope in the early 20th century [182, 183], it has become a critical tool for biological research. The use of fluorescent probes has allowed scientists and physicians to increase contrast and signal from a region of interest, allowing for the study of biological systems that could not previously be imaged. One of the most common uses for fluorescence is in the diagnosis, planning, and treatment of cancer. For example, fluorescence imaging has been used for the resection of brain tumors. As mentioned in section 3.1, Gliolan® (5-ALA) is an FDA-approved imaging agent used for fluorescence-guided surgery of GBM. 5-ALA is a hemoglobin precursor, with PpIX being a fluorescent intermediary molecule [184, 185]. Changes in various metabolic pathways, such as the upregulation of coproporphyrinogen and downregulation of ferrochelatase, lead to an accumulation in glioma cells, but not healthy brain tissue [186]. By exciting the PpIX in tumor tissues with wavelengths between 375-420nm during surgery, tumor margins are highlighted for better detection and resection [187], increasing patient mean overall survival by an average of 3 months when compared to white light techniques [188].

[§] The contents in this chapter were reproduced from B. Gaitan et al., "Depth-resolved imaging of photosensitizer in the rodent brain using fluorescence laminar optical tomography," *Journal of Biomedical* Optics 25(9), 2020 with permission.

Another innovation is to use fluorescence imaging to optimize PDT. As stated in section 1.2.1, PDT is a photochemistry-based modality that involves the wavelength specific activation of molecules called photosensitizers. The activated photosensitizers produce reactive molecular species to modulate and damage the surrounding tissue [159, 189]. In addition to generating photochemistry, an excited-state photosensitizer can also emit fluorescence, which is useful for optical imaging without any additional dyes or tags [153]. The time between the administration of the photosensitizer and the peak accumulation in the target site (e.g., tumor) is known as the photosensitizer-light interval. Previous clinical and preclinical studies have shown that having an inappropriate photosensitizer-light interval can lead to less ideal treatment outcomes [190, 191]. The amount of light to deliver to the tissue of interest is another critical parameter used to optimize PDT, which can depend on various factors, such as photosensitizer-light interval and local photosensitizer concentration [192-194]. Due to the fluorescent properties of photosensitizers, fluorescent-based imaging is an ideal candidate to measure these important factors.

Various imaging modalities leverage fluorescence for photosensitizer imaging. Confocal imaging is a popular modality when imaging cells and tissue in the microscopic regime. The ability to restrict the light being imaged to a thin slice allows for high resolution when imaging thicker samples due to the mitigation of out of focus fluorescence. The main drawback of these imaging modalities is a small field of view (~1mm^2) and a shallow penetration depth (~50-200μm) [195, 196]. Widefield imaging is the most common modality used in the clinic for fluorescence imaging and is routinely used in 5-ALA-assisted FGR. The advantages are apparent with this

modality in that it is well studied and easy to set up, having micrometer resolution (under certain conditions), a wide field of view, and a large array of consumer grade products to choose from. The main disadvantage comes when imaging thicker samples such as human organs, with out of focus fluorescence and attenuation caused by the tissue reducing depth penetration, resolution, and signal-to-noise ratio [197].

Some methods have been developed to extract 3D information from brain tumor tissue. One methodology that has gained popularity in recent years is spatial frequency domain imaging (SFDI), which was originally developed by Cuccia et al. [198]. SFDI is an imaging method where line pairs are illuminated on the surface with at least three different frequencies, with each frequency being illuminated at various phases. The reflectance information is then used to extract scattering and absorption information of the tissue, and it has been used previously to reconstruct 3D tomographic information [199]. This information has been used to link variations in tissue absorption and scattering to map stromal, epithelial, and adipose tissue in the breast tumor tissue [200]. More recently, SFDI has been adapted to image photosensitizers, specifically PpIX, to locate the depth and concentration of a fluorophore by determining the optical scattering coefficient and either using a modulated light signal [201] or two distinct emission wavelengths [202] to extrapolate the 3D coordinates and concentration of the photosensitizer. SFDI has been found to confer certain advantages, such as current configurations being able to image a large FOV (9cmx9cm) and obtain signals up to 9mm [201, 202].

LOT imaging was first developed by Hillman et al. in 2004 to help overcome attenuation, compensating for signal loss as one images an object deeper in the tissue

in a similar fashion to diffuse optical tomography (DOT). Hillman et al. demonstrated LOT's ability to image an absorptive object in a scattering medium over a 9mm^2 area with a depth penetration of 1.2mm [203]. Afterward, Hillman adapted her LOT system to image fluorescent signals using LOT (FLOT). Specifically, FLOT was used to image the propagation dynamics of electrical waves in the heart over a 13.7mm^2 area using voltage sensitive dyes [204]. Chen et al. later developed an integrated system that combined FLOT with optical coherence tomography (OCT) to take advantage of FLOT's ability to image molecular information such as fluorescence and OCT's ability to image structural and functional information (blood flow, etc.) [205]. FLOT has also been used to measure neural activity in the brain [36] and has even been used in photoimmunotherapy (PIT) to image IR700 fluorescence distribution in a tumor at different depths to non-invasively measure therapeutic effects [35].

Although various studies have investigated using FLOT to image fluorescence in tumors to inform treatment, no research has been done to image the distribution of photosensitizer in the brain using FLOT. Building off on previously performed studies, the benefits of using FLOT to measure photosensitizer are clear, with the ability to compensate for signal loss caused by tissue attenuation and the ability to image in three dimensions. With clinical studies investigating the treatment of brain cancer with several photosensitizers, including Gliolan®, Photofrin, and BPD (NCT03897491, NCT03048240, NCT00870779, NCT00002647), the need for accurate photosensitizer measurements in the brain has gained greater relevancy.

In this study, we found that by using FLOT to image the clinically used photosensitizer, BPD, we could maintain a non-significant change in resolution up to 600μm in depth. Upon comparing FLOT signal loss in the z-direction to maximal intensity projections (MIP) in phantoms, we found that 2D imaging showed an exponential decay in signal, while FLOT imaging was able to maintain up to 80% of the original signal up to 500μm. E*x vivo* measurements displayed similar patterns as the phantom experiment.

4.2 Methods

4.2.1 Liposome synthesis and characterization

BPD was incorporated into the bilayer of nanoliposomes via freeze-thaw extrusion as described previously [147-150]. Briefly, lipids, dipalmitoylphosphatidylcholine (DPPC), cholesterol, and 1,2-distearoylphosphatidylethanolamine-methoxy polyethylene glycol (DSPE-PEG), and 1,2-dioleoyl-3-trimethylammonium-propane (DOTAP) (Avanti Polar Lipids, Alabaster, AL), were co-dissolved with BPD (50nmoles, U.S. Pharmacopeial) at 0.15mol% BPD-to-lipid ratio in chloroform. A thin film, created on a rotary evaporator, was rehydrated with deionized water, subjected to freeze-thaw cycles (4-45°C), and extruded through polycarbonate membranes (0.1μm pore size) at 42°C. Unencapsulated BPD was removed by dialysis against 1X PBS overnight. The final concentration of BPD within the liposomes was determined by measuring its absorbance and using the established molar extinction coefficient in DMSO (~34,895$M^{-1}cm^{-1}$ at 687nm) on a multi-mode microplate reader (Synergy Neo2,

BioTek, Winooski, VT). The retention of BPD's fluorescent emission was verified by the multi-mode microplate reader.

4.2.2 FLOT setup

The FLOT system can be seen in Figure 4.1. A 690nm laser diode was used to excite the BPD. The laser diode was then collimated by a 50mm lens. The collimated beam was then coupled to a cylindrical lens and focused to a line beam, with a full line-width half max of roughly 20μm. The fluorescence was collected through an objective lens, bandpass filter (735nm, FF01-735/28-25, Semrock, West Henrietta, NY), and then onto a 12-bit CCD camera with a pixel size of 2.9μm (EM-CCD, PCO Imaging, Kelheim, DE). The illumination angle was set at 135° on the surface of the substrate, with the CCD camera placed normal to the surface. A motorized stage was used to move the substrate perpendicular to the line illumination, taking a total of 300 images. OCT (Telesto, Thorlabs, Newton, NJ) was used to provide 3D structural information with a micrometer resolution. The *ex vivo* rat brain was first scanned with the OCT system to get 3D images, which provided the structural information. The OCT system utilized a swept laser source, which generated a broadband spectrum of 100nm full width at half maximum (FWHM) centered at 1310nm as previously described [35].

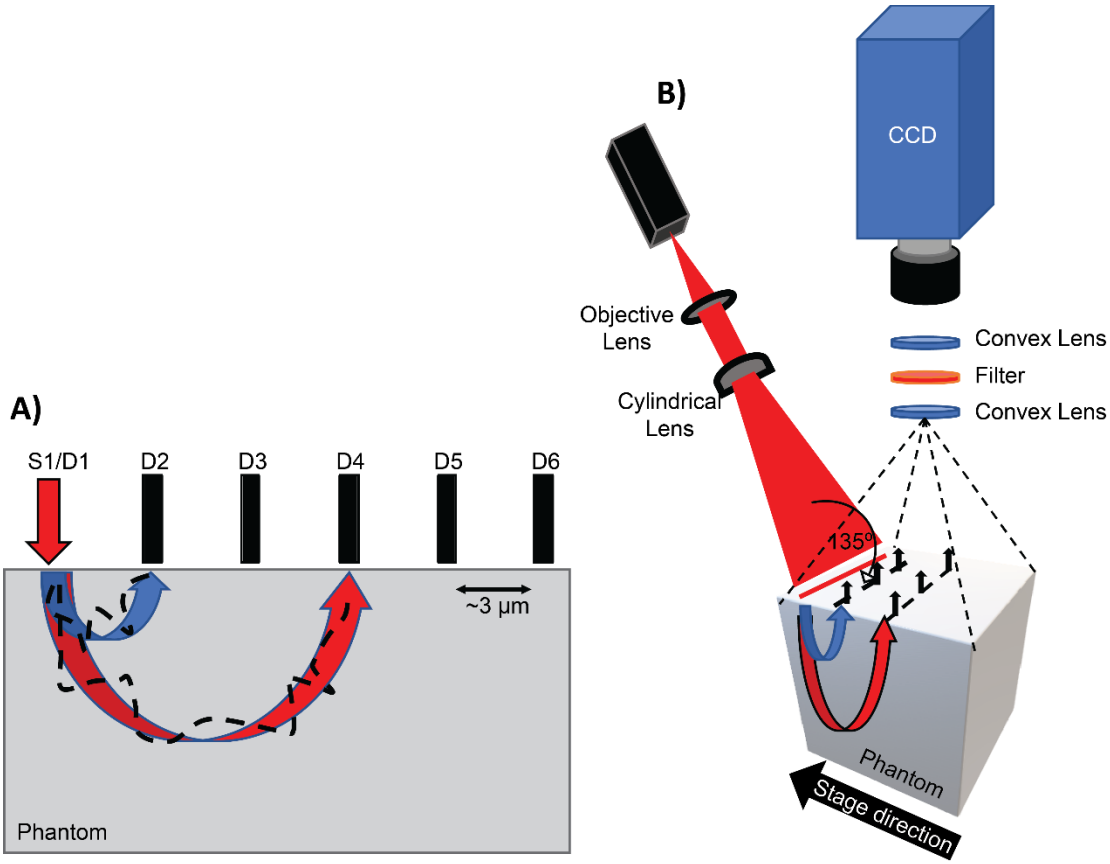

Figure 4.1: (F)LOT schematic

Schematic diagrams of different imaging techniques. a) Schematic of LOT demonstrates that wider source (S1) and detector (D#) offsets increase the photon migration pathway and the depth that is being imaged. b) Schematic of the FLOT system displays a line beam (source) that allows a large region to be imaged simultaneously.

4.2.3 FLOT reconstruction methodology

The FLOT system we used in these experiments is based on the laminar tomographic imaging developed by Hillman et al. [203, 204]. The design of the system is based on tomographic imaging methods such as DOT, taking advantage of source and detector separations, and the fact that photon scattering by structures in the brain is the dominant attenuation factor. Photons being remitted from the tissue or phantom at larger distances from the source have most likely penetrated deeper into the light scattering media, as seen in Figure 4.1a. Through the measurement of various source and detector separations, it is possible to reconstruct an entire 3D

image based solely on the fluorescence measured on the surface. As the incident light beam propagates through the tissue, some of the scattered light will be absorbed by the fluorophores of interest found in the tissue. An array of photomultiplier tubes or a charged coupled device (CCD) are used to collect photons that are emitted by the fluorescent molecules.

Various FLOT systems configurations have been developed previously. Some use point sources and detectors, using galvos to raster scan and illuminate a large area. Our FLOT system used a line field illumination, as seen in Figure 4.2. The main advantage of this system is the simplified setup since raster scanning with galvos is not needed. The FLOT system in our lab takes a laser, which was then collimated and focused into a line beam onto the tissue. As the laser light propagates throughout the tissue, fluorescence was generated where the photosensitizer was present. The fluorescent signal was then filtered to reduce the signal caused by the excitation beam, and the remaining fluorescent signal was collected by a Black/White CCD camera. Because there was always some light leakage, a line beam can be seen on the CCD camera. The observed line beam is then designated as the surface on the image. All other points on the CCD camera are then designated as detectors. This allowed us to collect many source and detector separations all at once. The tissue sample was then moved by using a motorized stage at a constant velocity, allowing for different source locations on the sample.

After obtaining the images, we solved the following equation, assuming the first-order Born approximation:

$$\Delta F(\vec{r_s},\vec{r_d}) = \int G(\vec{r_d} - \vec{r'}) \cdot O(\vec{r'}) \cdot \phi(\vec{r'} - \vec{r_s}, w) d^3\vec{r'}\,, \quad (1)$$

where ΔF is the fluorescence distribution in tissue, G is the probability density function that the fluorescence in position $\vec{r'}$ will be detected by the detector in position $\vec{r_d}$. ϕ is the distribution of the photons over $\vec{r'}$ coming from the source position $\vec{r_s}$, with w being the angular momentum. O is the position of the fluorophore in the tissue.

Equation 1 can also be referred to as:

$$\Delta F = W_{s.d.}\Delta O(\vec{r}), \quad (2)$$

where W is a weighted sensitivity matrix. After determining what the parameters are, we can conclude that by using the obtained ΔF and calculated $W_{s.d.}$, we can determine the actual object position in tissue ($\Delta O(\vec{r})$).

The weighting matrix can be determined by solving the radiative transfer equation. A common way to solve the radiative transfer equation is using the diffuse approximation. This method is normally used for DOT due to its simplicity in implementation and because it is computationally inexpensive [32]. The main drawback is that it is difficult for this method to resolve objects close (within scattering length) to the surface of the tissue being measured. Another method that can be used to solve the radiative transfer equation and obtain the required sensitivity matrix is using a Monte Carlo (MC) photon simulator. Although this stochastic method is more computationally intense, it provides a more accurate solution at shallower depths near the surface of the tissue. Because of this, we used an MC simulation to determine W by using MCX, a software suite developed by Fang et al.

[33]. With W estimated using an MC simulation, the inverse problem was solved using Tikhonov regularization, with the regularization parameter determined by the L-curve criterion [206, 207].

4.2.4 FLOT vs. MIP

To perform the best comparison, a MIP of the oblique stack was performed on the images before reconstruction to simulate a 2D image. MIP is a volume rendering image processing technique that is generated by projecting the volume of interest onto a viewing plane, in our case, the x and y plane. This gives us optimal contrast when imaging our phantom. A process flow for this can be seen in Figure 4.2.

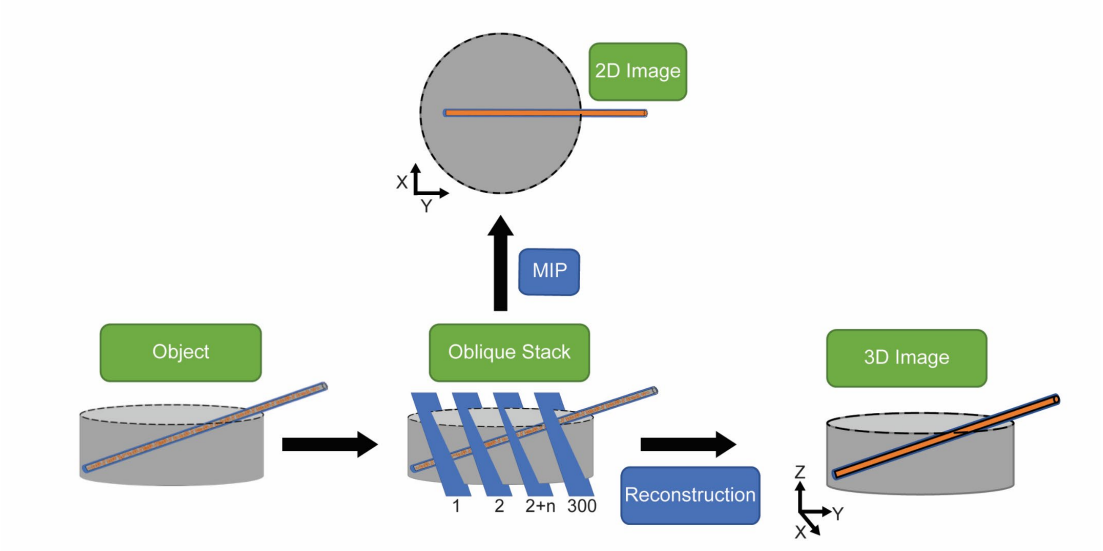

Figure 4.2: Overview of the process flow to make 2D and 3D images
A 2D (MIP) image is created by imaging the object with the FLOT system and orthogonally stacking the 300 images and taking the maximal value projected in the x and y direction. A 3D (FLOT) image is constructed by taking the oblique stack and using it to solve the inverse problem using MCX.

4.2.5 Liquid phantom preparation

To demonstrate the capability of the FLOT system to image photosensitizers, we filled a 100µm glass capillary (ID: 0.10mm, OD: 0.17mm, VitroCom Inc.,

Mountain Lakes, NJ) with 2.5μM of Liposomal BPD. This capillary was then placed at a 23.5˚degree angle inside of a 37mm petri dish and was sealed and fixed to the plate with an adhesive (5-Minute Epoxy, Thorlabs, Newton, NJ). Next, 2mL of 20% intralipid solution (Sigma Aldrich Inc., St. Louis, MO) and 48-mL PBS (Sigma Aldrich Inc.) were mixed and placed into the petri dish. In order to determine the scattering coefficient of the phantom, we used oblique-incidence spectroscopy [208] and found that the phantom has a scattering coefficient (μ_s) of ~15mm^{-1} (g = 0.9, n = 1.33, μ_a = 0.01mm^{-1}, μ_s' = 1.5mm^{-1} at 690nm). A schematic can be seen in Figure 4.3.

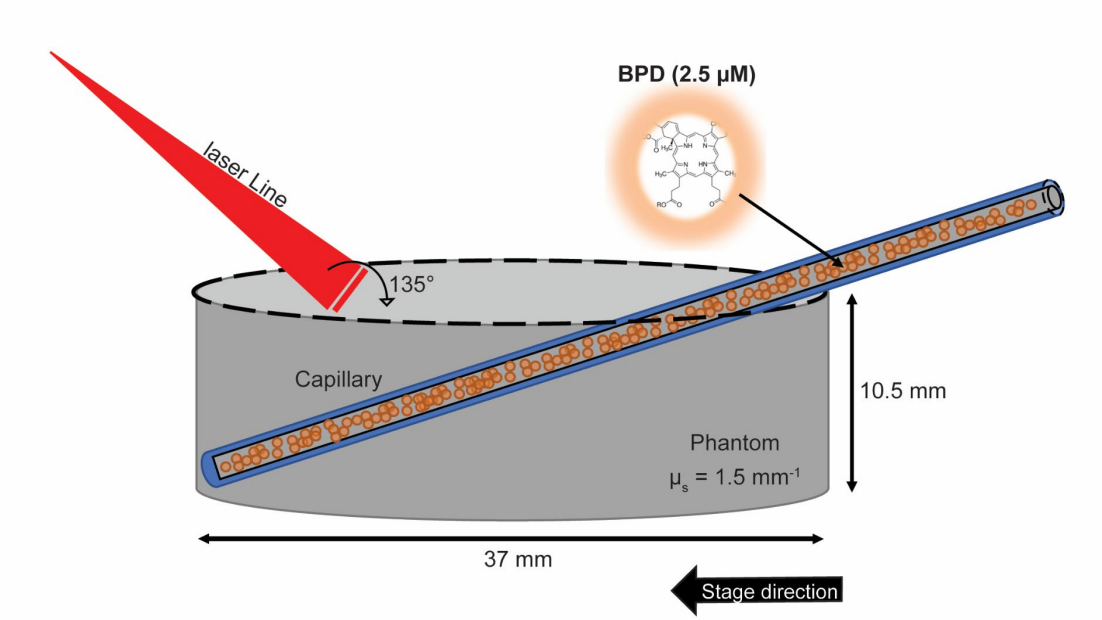

Figure 4.3: Schematic diagram of the liquid phantom set-up
A 100μm diameter capillary filled with 2.5μM of BPD is inserted into the phantom at 23.5˚. The stationary laser line intersects the phantom at a 135˚ angle. The phantom sits upon a motorized stage that moves perpendicularly to the laser line. Not to scale.

4.2.6 *Ex vivo* preparation

The *ex vivo* portion was carried out similarly to the phantom experiment, with BPD having a concentration of 2.5µM. The BPD was then inserted into a glass capillary (ID: 0.15mm, OD: 0.2mm, VitroCom Inc., Mountain Lakes, NJ) and inserted into a rat brain (Innovative Research, Inc, Novi, MI). Rat brains were ordered snap-frozen in liquid nitrogen and thawed at 4˚C before being used. The brains were first imaged by the OCT system and then by the FLOT system. The images were then co-registered. A schematic can be seen in Figure 4.4.

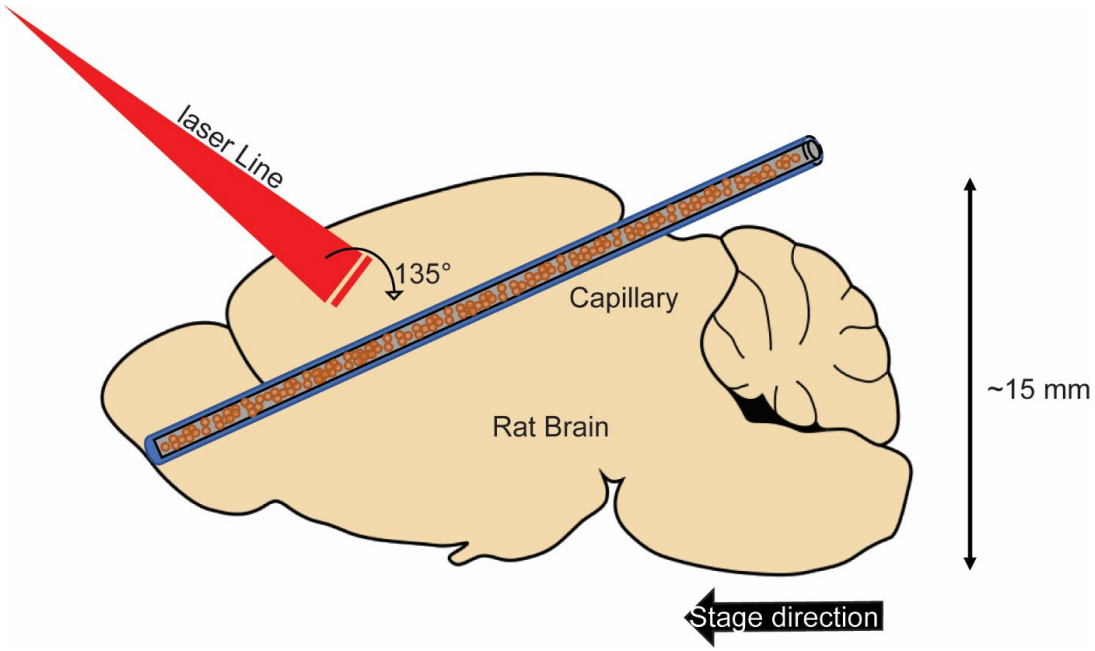

Figure 4.4: Schematic diagram of FLOT imaging of the rodent brain
A 100µm diameter capillary filled with 2.5µM of BPD is inserted diagonally into the rat brain. The laser line intersects the top of the brain at a 135˚ angle. The phantom sits upon a motorized stage that moves perpendicularly to the laser line. Not to scale.

4.3 Results

4.3.1 FLOT resolution tests in the lateral and axial direction

Initial phantom tests demonstrate that the FLOT system can detect BPD in a high contrast environment (2.5μM) up to a depth of 1.0-1.2mm until the signal to noise drops below the limit of detection, which is defined as $N + 3\sigma$, where N is the signal of the phantom with no capillary, and σ is the standard deviation of a blank image (standard deviation of noise) [209]. The shape of the capillary is preserved as it goes deeper into the phantom, demonstrating the ability to reconstruct the distribution of BPD faithfully when scanned perpendicular to the line beam. The resolution was determined by finding the FWHM of the capillary. The phantom test demonstrated a resolution of 116±5μm in the x and y direction (Figure 4.5b). To see what effect depth can have on the resolution of the system, the FWHM of the capillary was taken at different depths. The resolution at a depth of 0μm was 143±15μm, while at a depth of 600μm the FWHM was 178±30μm (Figure 4.5c). Although there is an increase in the resolution as we image deeper, the difference is non-significant up to a depth of 600μm (Figure 4.5d). It must be noted that this is when the object is imaged perpendicular to the line beam, as the imaging method is not perfectly isotropic. Objects can be imaged parallel to the line beam, but this results in an expansion of the point spread function in the lateral direction.

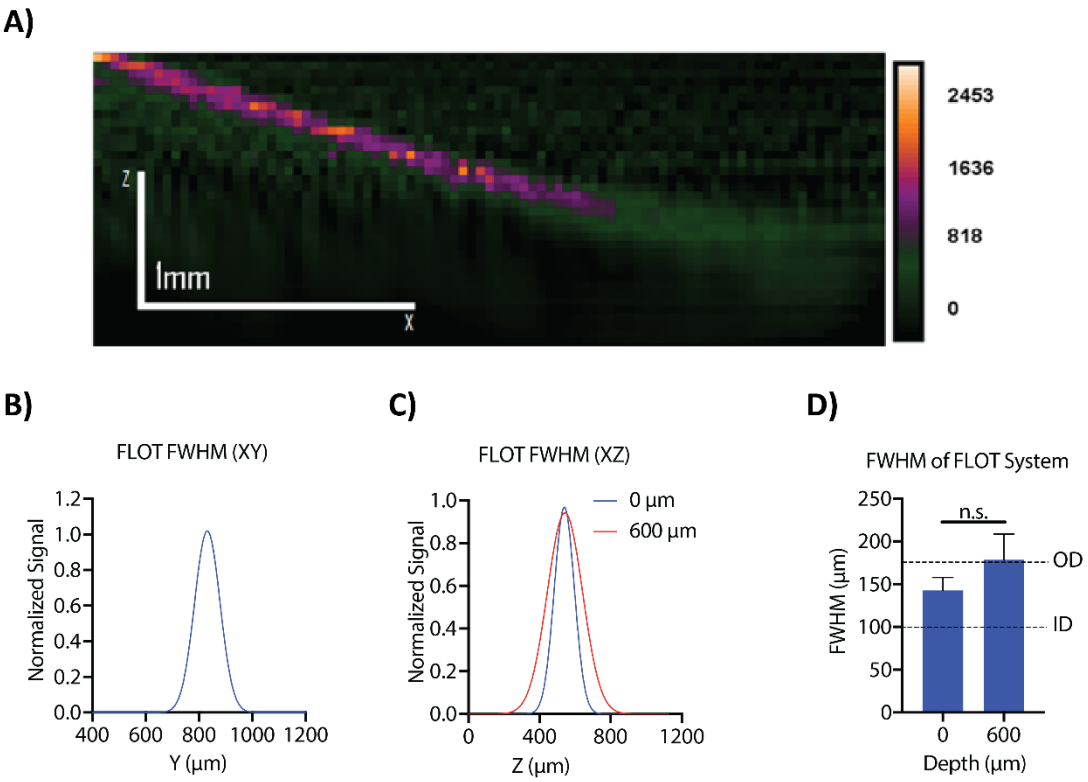

Figure 4.5: FLOT resolution and depth penetration
FLOT imaging of BPD within the phantom maintains a high degree of resolution at low depths. a) XZ image of a reconstructed FLOT image shows BPD fluorescence up to 1mm below the surface. b) Resolution of the FLOT system in the XY direction. c) Resolution of the FLOT system in the XZ direction at the surface (0 µm) and 600 µm beneath the surface. d) Comparison of XZ resolution at the surface and 600 µm beneath the surface.

3.2 MIP vs. FLOT comparison in a phantom

The same phantom setup that was used to determine the resolution of the system was also used to compare signal loss in the z direction between MIP imaging and FLOT imaging. Both MIP and FLOT images were normalized to the fluorescent signal at z = 0µm. Figure 4.6 shows the FLOT, MIP, the ideal signal, and 1/e intensity plots (e: Euler's number). The ideal intensity is when no signal attenuation occurs as one images deeper through a perfectly clear medium, as ideally, the FLOT system would correct to this line. The 1/e line represents a signal loss of 63%(1/e), which gives a method to compare MIP signal loss to 3D signal loss. The MIP demonstrates

an exponential decay pattern versus depth, which is expected for light loss in tissue. In contrast, the FLOT system demonstrates a double polynomial decay pattern, compensating for typical signal loss caused by the phantoms' attenuation. To perform a more direct comparison between FLOT and MIP imaging, the depth at which each modality reached a signal loss of 1/e was quantified. For the MIP image, the depth at which a signal of 1/e was reached was 588±27μm, while with the FLOT system, we did not see the signal decay to 1/e until 1073±118μm beneath the surface of the phantom($p<0.05$).

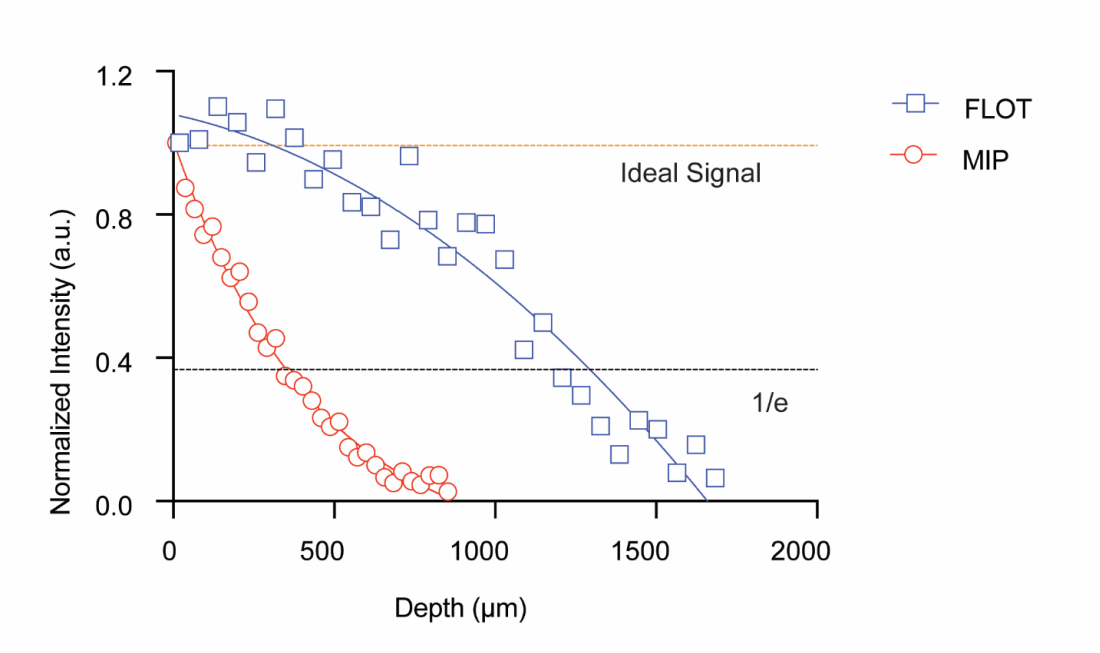

Figure 4.6: FLOT and MIP comparison in an agar phantom
Comparison of MIP and FLOT signals at various depths in a phantom. FLOT imaging can capture BPD fluorescent signals at a 2-fold greater depth than MIP. The ideal signal demonstrates what the signal should appear as if the reconstruction was perfect. The 1/e line shows the point where MIP and FLOT decay to 37% of their original value.

4.3.3 *Ex vivo* comparison of MIP and FLOT in a rodent brain

Ex vivo tests in the brain were done similarly to the phantom experiments, with a glass capillary filled with 2.5μM BPD. A larger capillary (ID: 0.15mm, OD:

0.2mm) was used as the 100μm capillary was too pliable, causing slight curvatures in the capillary, making the FLOT image more difficult to co-register with OCT. The OCT system was used to determine the ground truth for the angle of insertion of the capillary and the depth at different locations for both FLOT and MIP imaging. Decay patterns for MIP imaging demonstrate a similar decay pattern to that seen in the phantom experiments, with FLOT exhibiting signal compensation below the tissue surface as seen in Figure 4.7. FLOT and OCT imaging shows the ability to reconstruct the capillary faithfully. As in the phantom test, we compared the depth at which each modality reached a signal level of 37% (1/e). For the MIP image, the depth at which a signal of 1/e was reached was 334±38μm, while with the FLOT system, the signal did not decay to 1/e until 591±126μm ($p<0.05$).

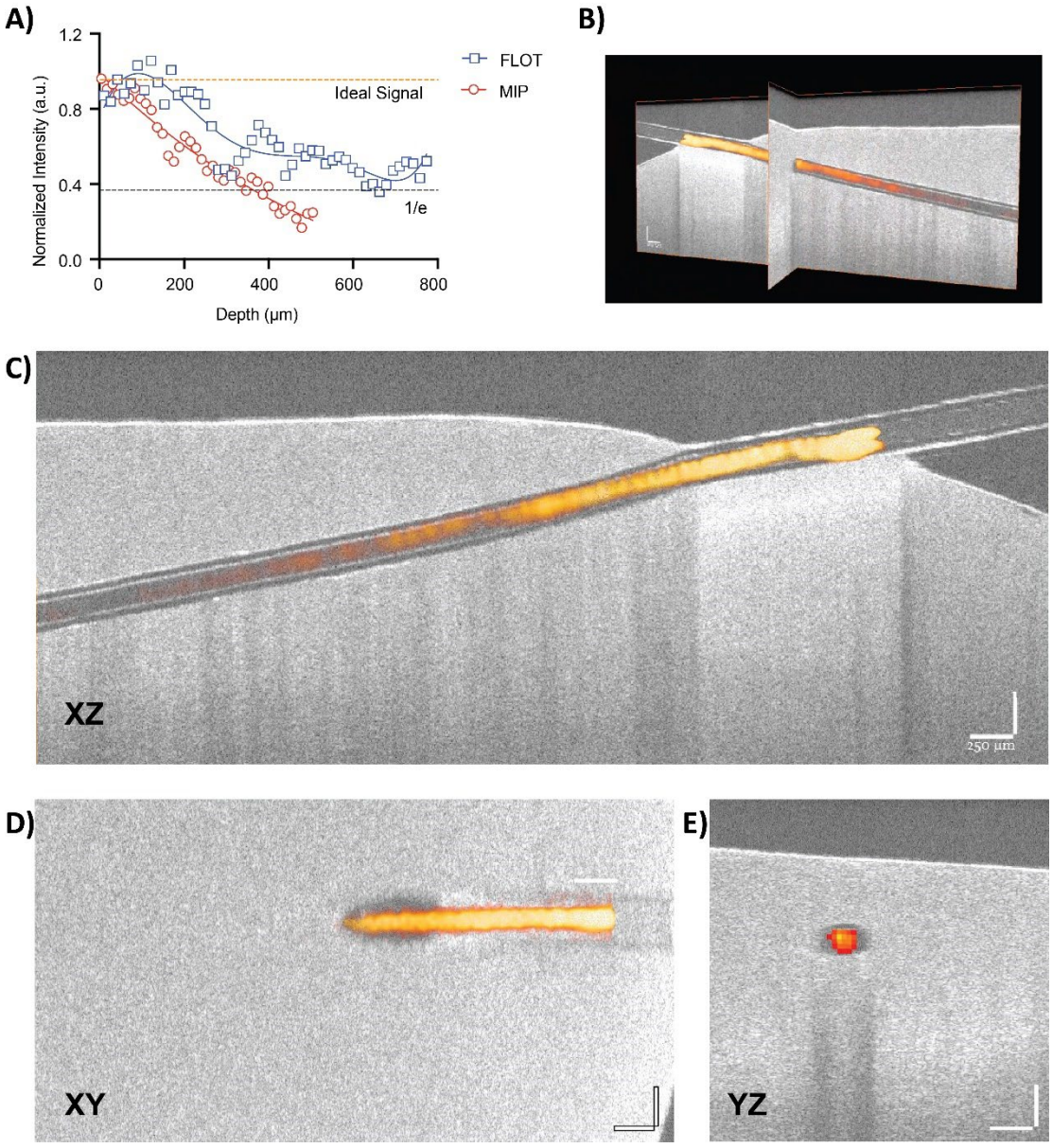

Figure 4.7: FLOT and MIP comparison in the rodent brain

Comparison of MIP and FLOT signals at various depths in the rodent brain. a) Normalized BPD signal captured by MIP and FLOT at various depths in an *ex vivo* rodent brain. b) *Ex vivo* rodent brain with a FLOT capillary image (orange) co-registered with an OCT image (grayscale). c) XZ slice of an OCT and FLOT overlay in an *ex vivo* rodent brain with a 250μm scale bar in white. d) XY slice of an OCT and FLOT overlay 250μm beneath the surface of an *ex vivo* rodent brain. e) YZ slice of an OCT and FLOT overlay 490μm beneath the surface of an *ex vivo* rodent brain.

4.4 Discussion

Photosensitizers, such as PpIX and BPD have been investigated for FGS. In this study, the use of BPD was used due to its larger maximum activation wavelength, leading to a deeper penetration depth. While Gliolan® has a maximal excitable wavelength of 630nm and an emission peak at 690m, BPD demonstrates a maximum excitation peak at 690nm and emission at 700nm [85]. Also, BPD gained FDA approval in the United States in 2002, specifically to treat wet age-related macular degeneration [141]. Several studies have looked into the use of BPD in the brain, in addition to developing mathematical tools to measure the amount of RMS produced by BPD for accurate dosimetry [210]. Our previous work demonstrated that 690nm light-activation of BPD induces PDT effects at further depths in the rodent brain (1.5-2cm), compared to 635nm light activation of PpIX (0.5-1cm) [85]. When imaging, we do not expect to achieve similar penetration depths when comparing the induction of PDT effects in the brain to imaging penetration, as inducing PDT effects only requires an excitation photon to reach the photosensitizer. Fluorescence imaging of a photosensitizer, on the other hand, involves several steps, including the absorption of a photon by the photosensitizer, the fluorescence to be generated (only a small fraction of the power input to the photosensitizer), the generated fluorescence to reach the surface of the tissue, and enough photons must then reach the surface to be read by a photodetector.

BPD has a low water solubility (i.e., inability to form sufficient hydrogen bonds with water), and it oftentimes requires solubilization or incorporation into a drug delivery platform for biological applications. Freeform BPD aggregates in

aqueous solutions and self-quenches, resulting in inadequate bioactivity and biodistribution. Liposomal encapsulation of BPD (Visudyne®) allows for the retention of its fluorescent emission due to its more monomerized molecules. Although liposomal encapsulation allows for improved photosensitizer delivery compared to free form BPD, one drawback is the heterogeneous pharmacokinetics and biodistribution of liposomes in normal tissues. The side effects of PDT on normal tissues could potentially help explain why the clinically used formulation has only modestly improved patient outcomes, as seen through numerous clinical trials (NCT00002647, NCT00049959, NCT00007969). This further demonstrates the need for an imaging system that can quantify the amount of BPD present at not only the disease site, but also in fragile normal tissues, like the brain.

In this study, we have demonstrated the capability of the FLOT system to better detect the distribution of BPD in the brain compared to MIP. The first advantage is that FLOT gives a full 3D image up to a depth of ~1mm in the brain, while MIP imaging gives a depth-integrated signal of a 3D volume that is heavily weighted toward surface readings. FLOT also helps to maintain resolution as one images deeper in tissue. Due to the scattering, the deeper light penetrates into the tissue, the greater the light spreads [173], decreasing resolution. Niu et al. developed a depth compensation algorithm to make a weighted matrix (W) to improve depth localization, defined as:

$$\mathrm{W} = [diag[M(A_l), M(A_{l-1}) \ldots M(A_2), M(A_1)]]^{\gamma} \quad (3)$$

where M(A) is the max single value for the forward matrix from the first to the l^{th} layer, and Υ is an adjustable power and is varied from 0-3, with a value of 0

representing no use of a depth compensation algorithm [211]. Using this algorithmic depth compensation, they found that when measuring objects with a 0.6cm diameter separated by 1.5cm, they could still be resolved when imaging up to 4cm below the surface with a ϒ of 1.3, while the objects could not be individually resolved with a ϒ of 0. These same advantages are likely the reason why we see a similar trend when comparing the resolution at the surface to that at 600μm below the surface. We do see that the resolution decays to a greater and significant degree after this point, likely because as the depth increases, the compensation that can be achieved using MCX decreases [36, 203].

The main advantage of FLOT is the signal compensation deeper in the tissue. The FLOT system without using a weighting/reconstruction method would simply be an oblique (30˚) stacking. Although this would allow for 3D visualization, due to attenuation, the signal would be weighted towards the surface of the tissue. The MIP image demonstrates an exponential decay pattern which has been reported through various simulations and experiments. The decay pattern in tissue is, in its most simplified form, described with the equation:

$$I(z) = I_0 e^{-(z*\mu_{eff})} \quad (4)$$

with z being the depth, I(z) is the intensity at the specific depth, I_0 is the intensity on the surface, and μ_{eff} is the effective attenuation coefficient, wherein conditions where $\mu_s >> \mu_a$, then $\mu_{eff} \approx \mu_s$ [212]. In Figures 4.6 and 4.7 an exponential decay pattern can be seen, fitting prior results. The weighted matrix allows us to compensate for some of the signal lost as we image deeper into the tissue, which can be seen in Figures 4.6 and 4.7. This depth compensation could be seen in similar systems, such as in

Hillman and Tang's previous work [35, 203, 204]. Although the FLOT system does compensate for some signal loss, this compensation does deteriorate as we image deeper in the tissue. The main reason is that to reconstruct the signal, the imaging system still needs to pick up photons. Even with a perfect reconstruction method, if there are no photons collected from a specific depth, then reconstruction is impossible. This means that we are still limited by scattering as we are dependent on a photon reaching the object and for the emitted photons to reach the surface.

With the system showing clear advantages over MIP imaging, there are still some improvements that could be implemented. Currently, the brain is assumed to have a uniform attenuation coefficient, but it has been demonstrated that the brain scattering coefficient varies with depth [213]. An MC simulation that would consider different layers of the brain would allow for a more faithful reconstruction. The brain also has curvatures that can increase the complexity of the boundary conditions not considered with the current iteration of the FLOT system. This can be mitigated through the integration of a mesh-based MC system and would also cut down on computational complexity [214].

Another concern that needs to be addressed is making the FLOT system more clinically compatible. Two main issues need to be solved before the device is ready for the clinic. The first is that the FLOT system needs to be made more flexible. For example, the setup would need to be altered so that it does not depend on the sample being moved to acquire images, as moving a patient would not be feasible during a surgery. Another issue that would need to be solved is the co-registration of the FLOT image with conventional 2D images. The FLOT is not meant to replace

conventional imaging, but to enhance it. Overlaying FLOT with 2D imaging would give the surgeon the most accurate spatial information possible without having to switch between different imaging modes.

Although adaptations still have to be made to make the device clinically viable, the ability to image in full 3D and compensate for signal loss gives this system the ability to give a better image of the real distribution of photosensitizer in the brain. Another benefit compared to some other similar imaging modalities is the relatively simple hardware, as there are only five main components (lenses, laser, camera, filters, motorized stage), and the alignment of the system is relatively simple. This makes the device likely to have a high tolerance, allowing it to be transported without worry of misalignment. Even with these adaptations, there will be some inherent limitations compared to conventional wide-field imaging that is used in the clinic. The largest limitation is the processing time necessary to make the 3D FLOT image. Because we rely on Monte Carlo simulations and reconstruction, it can take 30 seconds to 1 minute to reconstruct an image. Because of this, FLOT is not meant to be used during the entire surgery but rather used if the surgeon wants more information about the fluorescence distribution of a specific area in tissue.

Future work also needs to be done comparing the ability of the system to measure depth and compensate for signal loss when compared to other depth imaging modalities that are meant to be used for clinically imaging photosensitizers. A possible imaging modality to compare FLOT to is SFDI which, as mentioned in the introduction, has certain configurations that use the extracted scattering and absorption coefficient to find the depth of a fluorescent inclusion in brain tissue [201,

202, 215]. These systems have a similar field of view and clinical use case, so the comparison would help contrast both systems and aid in determining which modality is best for which scenario in the clinic.

4.5 Conclusion

We investigated the 3D distribution of BPD in phantoms and in rodent brains using FLOT imaging. The FLOT system was able to obtain images with a resolution of 110μm in the x and y direction and a resolution of 127-205μm in the z direction. We also compared FLOT to a MIP of oblique stacked images to perform the best possible comparison between 2D and 3D imaging. We found that we can compensate for signal loss deeper in both phantoms and in *ex vivo* brain tissue compared to MIP imaging. Although this method has shown to hold advantages over MIP, several steps must be taken to make the device more clinically compatible, such as adapting the device into an endoscope, making it easier to image in the brain cavity.

Chapter 5: Development of an Endoscopic AutoFluorescent Sensing System to Aid in Breast Cancer Imaging and Inform PDT Treatment

5.1 Introduction

One of the most popular optical imaging modalities used is fluorescence imaging due to its low cost, potentially compact size, and real-time imaging capabilities. Although fluorescent imaging has proven extremely useful, there are some drawbacks. For example, for many clinical imaging procedures, an exogenous contrast agent needs to be used to increase the signal of the area of interest. Although FDA-approved contrast agents are safe for patients, side effects can still occur. For example, Fluorescein, an FDA-approved imaging agent, can potentially lead to low birth weights when used on pregnant women [216]. And if a new contrast agent is developed, the approval process can be long and costly.

One fluorescent imaging method that has started to gain popularity is imaging autofluorescent molecules to circumvent the need to inject fluorescent probes. For example, tissue autofluorescence has been used to detect cancerous oral [217] and colorectal [218] lesions early in patients. There are many autofluorescent molecules such as collagen, tryptophan, and elastin that can aid in extracting information about cellular activity, with some of the most well studied and characterized molecules being NADH and FAD.

NADH and FAD are molecules that were first identified as auto-fluorescent biomarkers in the 1930s [219]. Later in the 1950 and ’60s NADH and FAD concentrations were found to inform the metabolism of cells and tissue [220, 221].

NADH and FAD are electron carriers in various cellular metabolic cycles such as oxidative phosphorylation, the Krebs cycle, and glycolysis. Because NADH and FAD function as electron donators and acceptors, respectively, measuring these metabolites can give detailed insights into the metabolic state of the tissue, such as if there are modulations of the electron transport chain [37, 38] or if the tissue is oxygen/nutrient saturated or starved. In addition, by measuring the ratio of these two molecules, known as the optical redox ratio [ORR ([FAD]/([FAD]+[NADH]))], the relative oxidative state of the cellular metabolism can be deduced [41].

There are many distinct ways that cancer tissues act in comparison to normal tissues. These can include, but are not limited to, rapid division and high cellular density. These distinctions in how cancerous tissues act lead to a distinct metabolic footprint in comparison to normal tissues. For example, normal tissues under normal external conditions go through oxidative phosphorylation to generate energy, while under certain conditions, cancer cells go through aerobic glycolysis in a process known as the Warburg effect [222, 223]. This and other metabolic changes in cancerous tissue can lead to significantly different metabolic footprints in each. For example, NADH and FAD concentrations are larger in cancerous breast tissues in comparison to normal breast tissues [224-226].

NADH and FAD not only differentiate tumor and normal tissue but can also inform various oncological treatment modalities. For example, by measuring autofluorescence *in vitro*, it was found that BGT226 (a PI3K/mTOR inhibitor) and cisplatin led to a decrease in redox ratio [227]. NADH and FAD signals have also been found to inform PDT treatment. For example, Broekgaarden et al. investigated

the effects of PDT treatments on cellular metabolism in 3D cell cultures. They found that in 3D cell culture and in *ex vivo* tissue, four days after PDT treatment, there was an increase in ORR. Because of the ability of NADH and FAD to image metabolic perturbations in tissue for cancer treatment methods such as PDT, imaging tissue metabolism could potentially inform a patient's response after treatment, aiding in determining if treatments are taking effect.

Because of the auto-fluorescent qualities of NADH and FAD, as well as the insights that these compounds lend to tissue metabolic activity, research has been done to construct imaging systems to determine cellular metabolic footprints. One of the first systems constructed for this purpose is a low-temperature scanning system, first developed by the Britton Chance lab, relying on freezing tissues, shaving the tissue to a flat surface, and raster scanning a probe on the surface to collect NADH and FAD fluorescence [228, 229]. This type of system has been used in recent years to detect if mitochondrial states change in the heart [230] and kidneys [231] when injured, as well as to study the metabolic footprint of cancerous tissues [224-226, 232, 233]. In addition to the freeze-scan method developed by the Chance lab, other imaging modalities have been used to study cancer in a laboratory environment, with one prominent example being two-photon microscopy. For example, two-photon has been used to find changes in breast cancer tumor microenvironment after chemotherapy [234] and to differentiate normal and precancerous epithelia [235].

Because of the wealth of information that can be gathered about metabolism, there have been many efforts to use NADH and FAD autofluorescent imaging to aid in patient diagnostics. For example, widefield redox imaging has been leveraged to

aid in developing an automated high throughput system for determining patient treatment response using 3D organoid cultures [236, 237]. Although widefield imaging of autofluorescence does lend insights into cancer aggressiveness and potential treatment response, the low fluorescence quantum yield of NADH and FAD and the relatively large form factor of widefield fluorescence imaging devices sensitive enough to image NADH and FAD limits clinical adoption. One method to overcome this limitation is to develop a handheld endoscopic imaging device to allow for easier maneuvering in the clinic. Due to the reduced distance between the surface and imaging probe, these systems can also capture more emitted photons emitted from NADH and FAD. For example, two-photon endoscopes have been developed to aid in the delineation of basal cell carcinomas in patients [238] and to extract histological information from a mouse kidneys ischemia-reperfusion model *in vivo* [239].

Although two-photon endoscopic devices have been developed to image NADH and FAD clinically and have been found to deliver high sensitivity and resolution images, most of these devices are relatively complex and intricate, leading to potential difficulty when being set up and used clinically. One way to overcome this complexity is to develop a simpler, one photon endoscope for NADH and FAD imaging. These devices have been previously developed to aid in cervical cancer detection [240] and to measure the metabolic states of different organs [241]. As such, we have developed an easy to use one photon endoscopic imaging system meant to be integrated into clinical workflow, with the current design meant to be

seamlessly accommodated into a breast cancer biopsy/diagnosis procedure by making the endoscope fit into a 12-gauge breast cancer biopsy needle.

In this paper, we describe the endoscopic imager that we developed and tested to measure NADH and FAD. We performed initial validation tests using tissue phantoms containing NADH and FAD to determine the limits of detection of the endoscopic system. Afterward, we performed tissue modulation experiments using Carbonyl cyanide 4-(trifluoromethoxy)phenylhydrazone (FCCP) and rotenone/antimycin A and compared the metabolically modulated results to those found in the literature. Afterward, we measured the quantity of NADH and FAD in tumor tissue, as well as compared the quantity of NADH and FAD in tumors that have been treated with PDT. We have found that our system can detect NADH and FAD in tissue, as well as detect metabolic changes in the tumor environment after PDT treatment.

5.2 Methods

5.2.1 Developing the endoscopic imaging system

Before the endoscope was developed, NADH and FAD absorption and fluorescence spectra were taken using a plate reader (Synergy Neo2, BioTek, Winooski, VT), with the NADH and FAD being excited with 375/10nm and 473/10nm (using a filtered white light source) respectively for the fluorescent readings.

A 375nm laser diode (L375P70MLD, Thorlabs, Newton, NJ) and a 473nm laser diode (L473P100, Thorlabs, Newton, NJ) were used to excite NAD and FAD,

respectively. Each diode laser was connected to a laser diode current controller (LDC202C, Thorlabs, Newton, NJ). A dichroic short pass mirror (T450SPXRXT, Chroma Technology Corporation, Bellows Falls, VT) was placed at a 45° angle with respect to the optical axis of the 473nm light to transmit the 375nm light and reflect the 473nm light and couple the lasers to the excitation fiber bundle. The excitation fiber bundle was made up of polyimide buffer with a 400μm diameter and a numerical aperture of 0.22 (Spectraconn, Rockaway, NJ). To couple the 375nm laser light to the excitation fiber, a collimating lens (f=25mm) and a focusing lens (f=50mm) was used. Similarly, a collimating lens (f=25mm) and a focusing lens (f=75mm) were used to couple the 473nm laser to the excitations fiber bindle. To switch between the two lasers, a shutter (SH1, Thorlabs, Newton, NJ) was used and controlled using a K-cube controller (KSC101, Thorlabs, Newton, NJ). The emission imaging fiber bundle (Model No: 1533451, Schott North America, Inc. MA) has a diameter of 1mm, with each fiber having an 8.2μm with a 13.5k total fiber count. The excitation and emission fibers were separated due to the autofluorescence that is generated by coherent fiber bundles when excited at the UV range [242], decreasing the signal-to-noise ratio. By separating the excitation and emission fibers, we reduce the emission light passing through the imaging fiber, reducing the noise caused by the autofluorescence, leading to an increase in signal to noise. The endoscope tip and shaft had a maximal diameter of 2.7mm so that the endoscope could fit easily inside of a 12-gauge needle, one of the most commonly used needle sizes used for breast cancer core biopsies [243-245]. The system was designed so that the light collected from the imaging fiber would pass through an objective lens (f=25mm), a filter wheel

(FW102C, Thorlabs, Newton, NJ), and then a tube lens (f=75mm). The filter wheel had contained a 469/35nm filter (FF01-469/35-25, Semrock, West Henrietta, NY) to capture the NADH signal and a 520/35nm filter (FF01-520/35-25, Semrock, West Henrietta, NY) to capture the FAD signal. After passing through the tube lens, the signal was captured by a CCD (Model: Pixis1024 -16bit, Teledyne Princeton Instruments, Trenton, NJ). The shutter system, filter wheel, and CCD were controlled using a LabVIEW (Austin, TX)/Matlab (Natick, MA). The resolution of the system would be tested through the imaging of a negative USAF 1951 test target (Thorlabs, Newton, NJ).

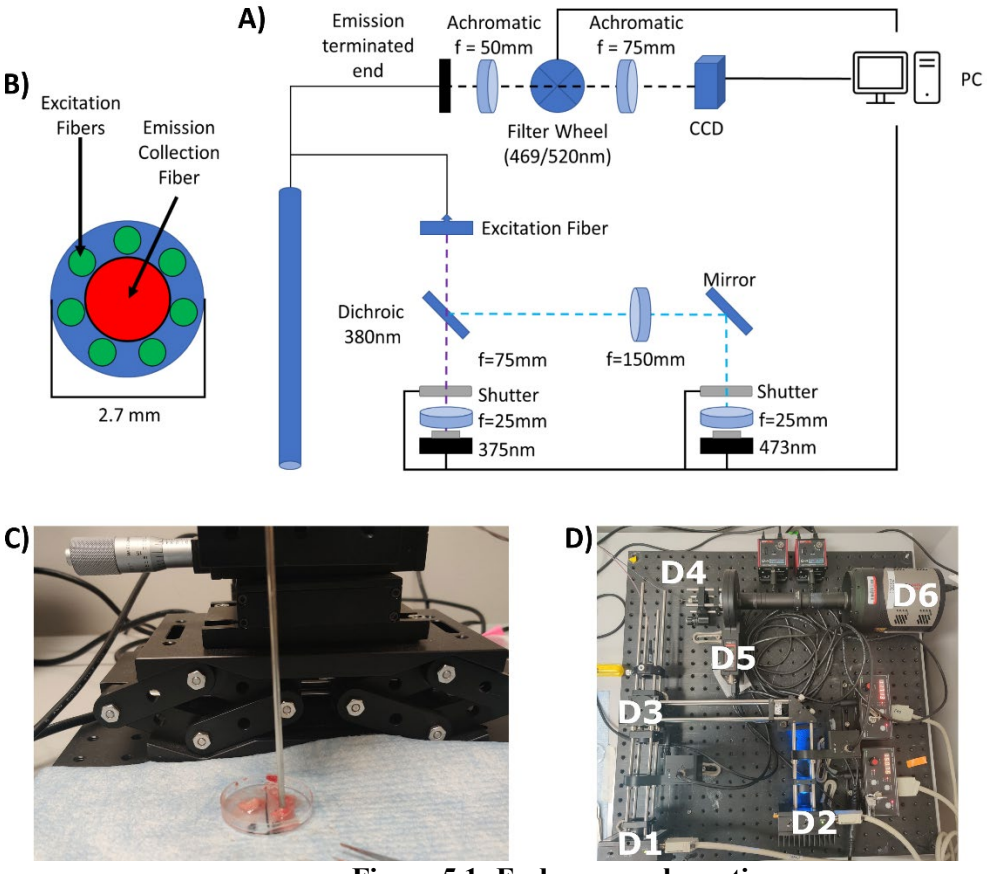

Figure 5.1: Endoscope schematic

a) schematic of the developed endoscope, b) a zoomed-in version of the endoscope tip, c) a picture of the endoscope shaft, and d) an image of the inside of the internal components of the endoscope system with the following components being denoted by the following labels: D1)

375nm laser D2) 473nm laser D3) excitation fiber bundle D4) terminal end of the imaging fiber bundle D5) filter wheel and D6) CCD.

5.2.2 Validation of endoscopic device using phantoms

To test and quantify the ability of our developed endoscopic system to image NADH and FAD, the endoscope was tested using liquid phantoms. The phantom was made with a combination of PBS (10010023, ThermoFisher, Waltham, MA), Intralipid (I141 Sigma-Aldrich, St. Louis, MO), NADH (N8129, Sigma-Aldrich, St. Louis, MO) or FAD (F6625, Sigma-Aldrich, St. Louis, MO). The intralipid phantom was meant to mimic the optical properties of human breast tissue, which has a μ_s' of 15-20cm^{-1} at wavelengths between 350-500nm [128, 168, 246], so the intralipid was diluted to a final concentration of 3.3%v/v using PBS to produce the μ_s' of 18cm^{-1} for NADH and 16cm^{-1} for FAD [168, 247]. Seven-different concentrations (0, 6.25, 12.5, 25, 50, 100, and 200μM) of NADH and FAD were prepared. Of the prepared liquid, 330μL was pipetted into a black bottom 96 well black bottom plate (655076, Greiner Bio-One, Kremsmünster, AT) and imaged in the well. During the measurements, the tip of the endoscopic device was placed inside the liquid phantom, and the images were obtained using 300ms, and 1000ms, exposure times. After obtaining the signals, they were background-subtracted using the 0μM reading. In the present study, we estimate the limit of detection by the protocol approved by the International Council of Harmonization [248]. Based on the sub-section "Validation of analytical procedures text and methodology", the limit of detection (LOD) is calculated using the following formula:

$$LOD = \frac{3.3\sigma}{S} \quad (1)$$

where S is the slope of the calibration curve, and σ is the standard deviation of the blank.

To measure the penetration depth of the NADH and FAD channels, a solid resin phantom was developed. The resin phantom (EasyCast, Environmental Technology Inc., Fields Landing, CA) was prepared by mixing the resin and hardener at a 1:1 ratio (by weight) and mixing in NADH or FAD so the final mixture would have a concentration of 100μM of either NADH or FAD. The mixture was then stirred for 10 minutes and allowed to cure in a low-pressure environment for 24 hours to harden and remove any air bubbles. The thickness of the resin phantom was 3mm. The endoscope would then be used to image the resin phantom. Afterward, a mixture of PBS and intralipid, with a final concentration of 3.3% v/v, was added to the top of the resin phantom, and was imaged using optical coherence tomography (OCT [Telesto, Thorlabs, Newton, NJ]) to confirm the thickness of the liquid layer, and then imaged with the endoscope. This process was repeated until a 1mm and 4mm depth was reached for the NADH and FAD phantom respectively.

To further validate the endoscope, we compared the endoscopic imaging system to a redox scanner developed by the Chance lab (in this publication, we will refer to this system as the Chance scanner). To compare the two systems, a series of standards were measured with both systems. NADH and FAD phantom matrices were made with concentrations of 3.9, 7.8, 15.6, 31.2, 62.5, 125, and 250μM, being diluted with a mixture of PBS + Intralipid (3.3% v/v). The details for phantom matrix preparation and the Chance redox scanner instrumentation at the University of Pennsylvania can be found in previous publications [228, 233]. The phantom matrices were snap-frozen and

milled flat before scanning/imaging with both the Chance redox scanner and the endoscope. Similar to the operation of the Chance redox scanner, the endoscope was positioned 80μm above the surface of the phantom using a precision motor equipped with the Chance redox scanner. The endoscope was set to a power of 5mW for both the 375nm and 473nm lasers, with the exposure time being set at 200ms.

5.2.3 *Ex vivo* constant parameters

For all *ex vivo* experiments, we collected five images per individual point measured, the exposure time was kept at 1000ms, and the power was set at 10mW for the 375nm and 473nm laser respectively.

5.2.4 *Ex vivo* modulation

To ensure that the signals that were being measured were the autofluorescent molecules NADH and FAD, we performed tissue modulation experiments to determine if our endoscope could detect induced changes in tissue metabolism. The modulations were performed on MDA-MB-231 tumors that were implanted into female BALB/c mice (Charles River Laboratories, Wilmington, MA). This cell line was chosen due to previously being characterized by the Chance scanner and having an elevated NADH and FAD concentration [225]. These mice were injected subcutaneously in the flank with 1E7 cells and were left to grow until a diameter of 12±3mm was reached. After this size has been reached, the mouse was euthanized, and the tumor was harvested.

Before the experiments were performed, three different solutions were prepped. One was an 8mM glucose (49163, Sigma Aldrich, St. Louis, MO) solution.

The second was a 50μM solution of FCCP (C2920, Sigma Aldrich, St. Louis, MO) and 8mM glucose. The last solution was a mixture of 50μM and 20μM of rotenone (R8875, Sigma Aldrich, St. Louis, MO) and antimycin A (A8674, Sigma Aldrich, St. Louis, MO) respectively.

After harvesting the tumor, the pieces were divided into two to three equal-sized pieces. The pieces were initially placed into the 8mM glucose solution for five minutes. After five minutes, the same tumor pieces were removed from the solution and imaged with the endoscope. The pieces were then placed in the FCCP solution for five minutes and imaged with the endoscope. And lastly, the tumor pieces were placed in the rotenone and antimycin A solution for five minutes, then imaged.

In total three different mice tumors were used, with seven different tumor pieces being individually imaged.

5.2.5 *Ex vivo* tumor imaging

To measure the ability of the endoscopic system to differentiate normal tissue and tumor tissue, we performed experiments measuring breast cancer tumors, specifically MDA-MB-231 tumors. We measured the rim and core of the tumor, as previous publications have demonstrated that in MDA-MB-231 cell lines, the tumor core (inside of the tumor) and rim (outside of the tumor) have distinct auto-fluorescent metabolic profiles [225].

Tumors were prepared using the same method outlined in section 5.2.4. Female BALB/c mice were injected subcutaneously with 1E7 cells with tumors grown until a diameter of 12±3mm was reached. After the adequate tumor size was

reached, the mouse was sacrificed, and the tumor was removed from the mouse. The tumor rim was then imaged, taking two to four unique and non-overlapping locations. The tumor would then be removed and cut in half, with each half having the core imaged. The skin would then be removed from the mouse quadriceps, with two unique locations being imaged on the quadricep.

Four total mice tumors and quadriceps were used, with 22 rim, 19 core, and 18 quadricep images taken in total.

5.2.6 PDT treatment and subsequent metabolic imaging

To determine how PDT exposure would affect the tumor microenvironment, we performed PDT on tumors implanted on nude Female BALB/c mice. Same as in sections 5.2.4 and 5.2.5, 1E7 of MDA-MB-231 cells were injected into the flank of the mice and allowed to grow until a size of $12\pm3mm^2$ was reached.

After the adequate tumor size was reached, benzoporphyrin derivative [(BPD) US Pharmacopeia] was injected via tail vein injection at a concentration of 0.5mg/kg. The procedure to produce BPD can be found in previous publications [85, 147-149]. After 24hours, the mouse was anesthetized and covered with a black cloth, except for the tumor, which was left exposed. BPD was then activated using a laser with a wavelength of 690nm (ML6600, Modulight, Tampere, FI) at an irradiance of $100mW/cm^2$ for a total radiant exposure of $100J/cm^2$. After PDT exposure, the mouse rim, core, and quadriceps were imaged in the same method described in section 5.2.5.

Control mice were also imaged, with the methodology being the same as in the previous paragraphs in this section, except that the tumors on the mice were not exposed to the 690nm activation light.

To determine the concentration of BPD in the tumor, fluorescent images were acquired using a top-down fluorescent imaging system. The excitation laser was a 685nm laser diode (HL6750MG, Thorlabs, Newton, NJ). The light from the laser was then collimated, with 8mW of light being delivered to the sample. The fluorescence was then collected through an objective lens, passing through a 735nm filter (FF01-735/28-25, Semrock, West Henrietta, NY), with the remaining light passing through an imaging lens and being collected with a 12-bit CCD camera (EM-CCD, PCO Imaging, Kelheim, DE) with an exposure time of 100ms. To determine the approximate concentration, a standard curve was made with concentrations ranging from 0-1000nM.

Six mice were used in total, three experimental and three control. For the experimental group, a total of 15 rim, 14 core, and 6 quadricep images were taken. For the control group, a total of 9 rim, 11 core, and 6 quadricep images were taken.

5.2.7 Data processing

All graphs and plots were made using Prism (San Diego, CA), with all graphs being plotted using standard error mean. Results were calculated using either a one- or two-way ANOVA.

3. Results

Figure 5.2 demonstrates the normalized emission and absorption spectra of both NADH and FAD. The lines in Figure 5.2a demonstrate the excitation wavelength used to excite NAHD (375nm) and FAD (473nm) in the plate reader and

the endoscope. The boxes in Figure 5.2b demonstrate the central wavelength and bandpass of the filter used on the endoscope. NADH and FAD crosstalk is minimal when measuring the emission of these two fluorophores at the corresponding excitations of NADH and FAD.

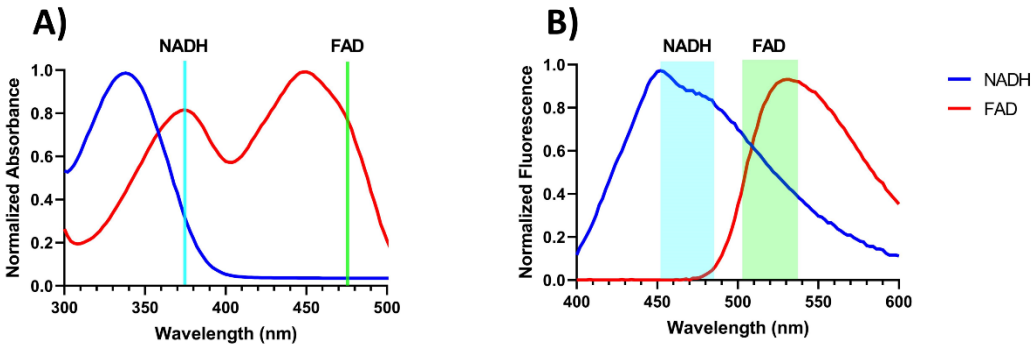

Figure 5.2: Absorption and emission spectrum of NADH and FAD
a) demonstrates the normalized absorption spectrum of NADH (blue) and FAD (red). The blue and green lines represent the excitation wavelength used to excite the NADH and FAD. b) demonstrates the normalized emission spectrum NADH (blue) and FAD (red), with the blue and green boxes representing the bandpass window of the endoscope for NADH and FAD, respectively.

Figure 5.3 investigates performing a simple validation of the endoscopic system using NADH and FAD phantoms outlined in section 5.2.2. The curve was obtained using NADH and FAD concentrations between 0 and 200µM. For NADH, the signal remained linear up to 200µM, while some nonlinearity can be seen for FAD. One reason for this non-linearity in the FAD channel is oversaturation, especially for the 1000ms exposure time. When imaging FAD in 3.3% intralipid above a 35µM the signal began to oversaturate the sensor at an exposure time of 1000ms. Although saturation is one cause of non-linearity in the FAD channel, it is not the only reason since plateauing can still be seen in the FAD channel even without oversaturating the sensor, with the linearity dropping below an R^2 value of

0.97 at concentrations above 100µM. Looking at the LOD for NADH, we found that at an exposure time of 300ms the LOD was 47µM, while at a 1000ms exposure time the LOD was 44µM. For the FAD channel, the LOD at an exposure time of 300ms was found to be 1.5µM, while at a 1000ms exposure time the LOD was found to be 1.3µM. Resolution tests have found that under ideal conditions, the NADH channel had a resolution of 31µm and the FAD channel had a resolution of 11µm.

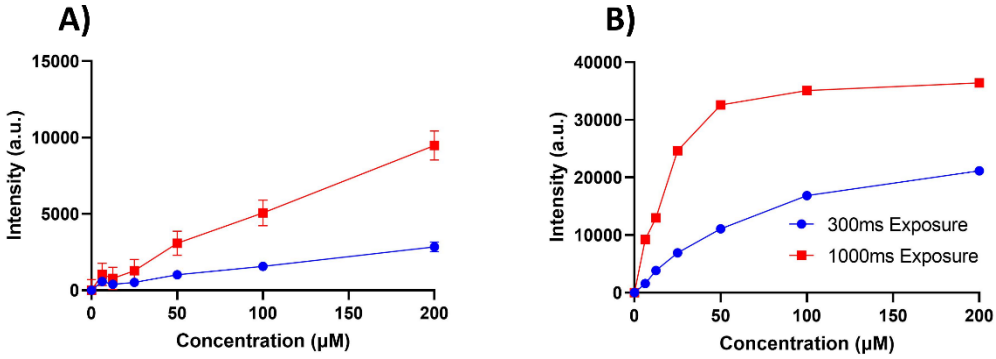

Figure 5.3: NADH and FAD standard curves
a) NADH and b) FAD standard curves with a concentration range between 0-200µM with 3.3% intralipid at 300ms and 1000ms exposure times. The signal was background subtracted using the 0µM readings.

Figure 5.4 demonstrates the depth sensitivity of the endoscope when imaging NADH and FAD. Figures 5.4a and 5.4b show the 3mm 100µM NADH and FAD resin phantom respectively, with the 3.3% (v/v) intralipid solution being layered on top of the resin phantom. Figure 5.4c shows the obtained signal normalized to the surface reading. The imaging depth was defined as when the signal intensity dropped to 1/e [129], which for NADH was 0.6mm and for FAD was 3.3mm.

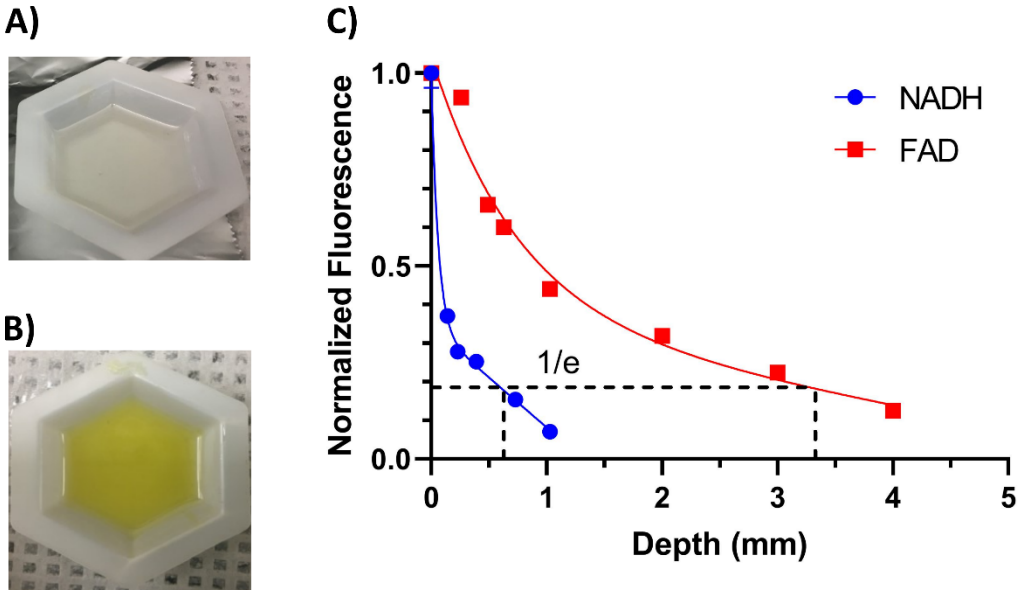

Figure 5.4: Depth sensitivity of the endoscopic system
Representative images of the 100μM a) NADH and b) FAD resin phantoms. Figure c) demonstrates the depth sensitivity of the NADH and FAD channel in liquid phantoms, with the intensity dropping to 1/e of the surface height being defined as the penetration depth.

To further validate the system, we compared the endoscope to the Chance scanner, the results of which we can see in Figure 5.5. Figures 5.5a/b are the NADH/FAD signals obtained by the endoscope, and Figures 5.5c/d are the signals obtained by using the Chance scanner. To directly compare the signals obtained by the Chance scanner and the endoscopic imaging system, we plotted the signals obtained through the Chance scanner and endoscopic imager on the same plot in Figures 5.5e/f. The cross-comparison demonstrated good linearity, having an R^2 value of 0.98 and 0.99 for the NADH and FAD channels respectively.

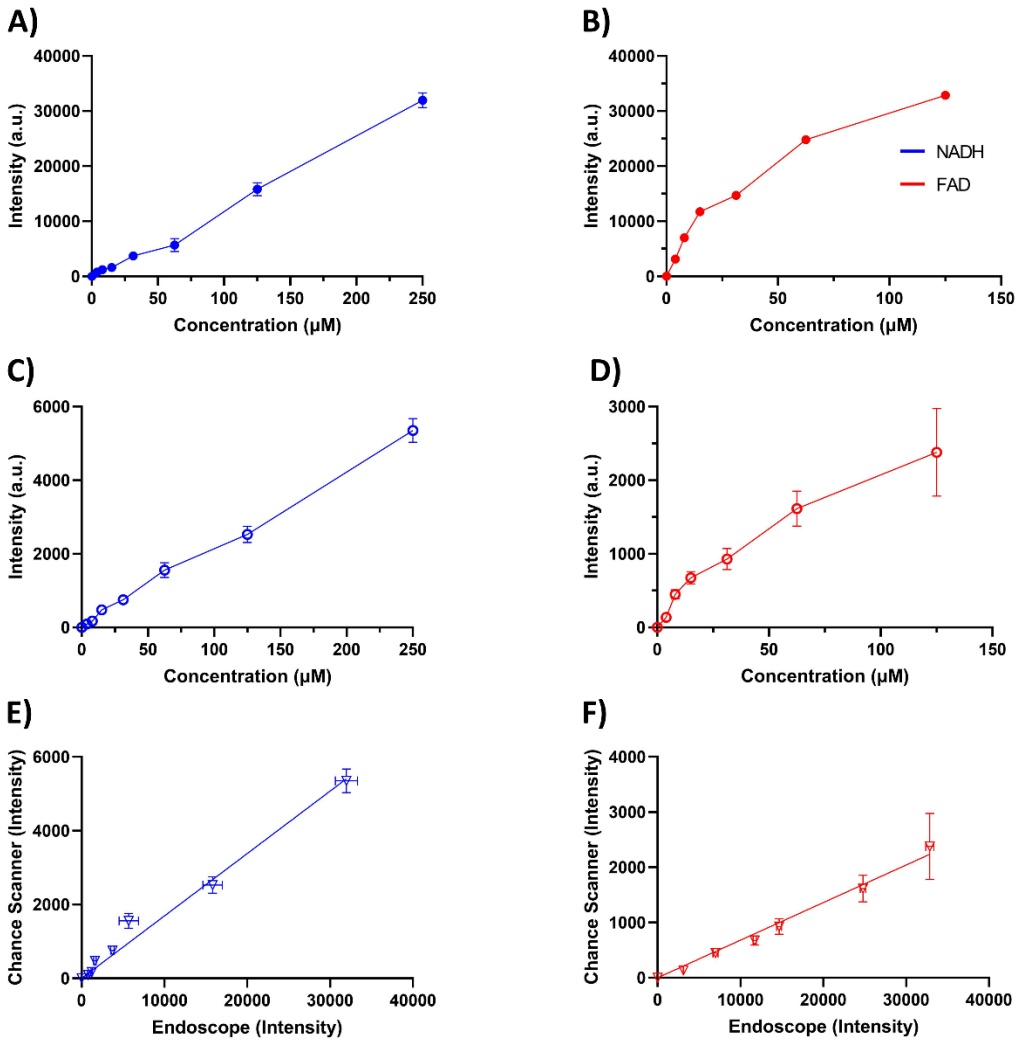

Figure 5.5: Endoscope and Chance scanner comparison
The a) NADH and b) FAD signals of the endoscopic imaging systems are displayed. In addition, the c) NADH and d) FAD signals were obtained from the same standards using the Chance scanner. Figures e/f are the cross-comparisons between the endoscope and the Chance scanner. All blue lines denote NADH plots and red lines denote FAD plots. In addition, closed circles (●) denote signals obtained using the endoscope and open circles (○) denote signals obtained using the Chance scanner. Triangles (▼) represent the cross-comparison plots.

In Figure 5.6 we see the acquired NADH and FAD signals after certain tissue modulations are performed. No drug represents the tumor being placed into an 8mM glucose solution with no mitochondrial modulators present in solution. When comparing the tumor pieces after being placed in the no drug solution and after being

placed in the FCCP solution, we saw a 36% decrease in NADH**, and** a 31% increase in FAD, which led to a rise of 12% in the calculated ORR. When comparing the tumor pieces imaged after being in the FCCP solution to images after the tumor pieces were placed in the rotenone and antimycin A solution, the NADH signal rose slightly by 6%, while the FAD signal decreased by 15%, leading to a drop in the ORR of 6%. Although we can see trends in the data, the only significant difference is seen when looking at the difference in ORR between the no drug images and the FCCP images ($p = 0.023$).

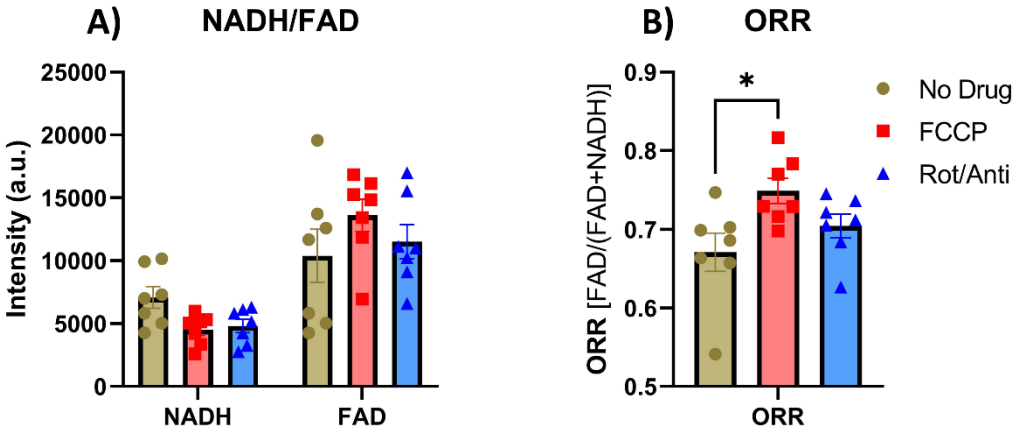

Figure 5.6: Endoscope modulation data
Modulation data for the a) NADH and FAD channels and b) calculated ORR. No drug is when the tumor pieces were imaged after being placed in 8mM glucose. FCCP is when endoscope images were taken after tumor pieces were submerged in a 50µM FCCP/8mM glucose solution. Rot/Ani represents when the tumor pieces were imaged after being submerged in a 50µM /20µM/8mM rotenone, antimycin A, and glucose solution. All tumor pieces were imaged after being in their respective solutions for five minutes.

Figure 5.7 demonstrates the signals collected from the tumor and muscle tissue, with the tumor tissue having the core and the rim imaged, as well as imaging muscle tissue from the quadriceps. Figure 5.7 is divided into a) the NADH signals measured, b) the FAD signals measured, and c) the calculated ORR. The core of the

tumor was found to have a 30% lower NADH signal, a 55% higher FAD signal, and a 29% higher ORR signal than the tumor rim. These differences seen between the core and the rim are significant ($p \leq 0.007$) except when comparing the rim and core NADH signals, where the rim has a larger NADH signal than the core, but the change is not significant ($p = 0.077$). The muscle tissue demonstrated a higher NADH, lower FAD, and lower ORR than both the tumor rim/core ($p \leq 0.0001$).

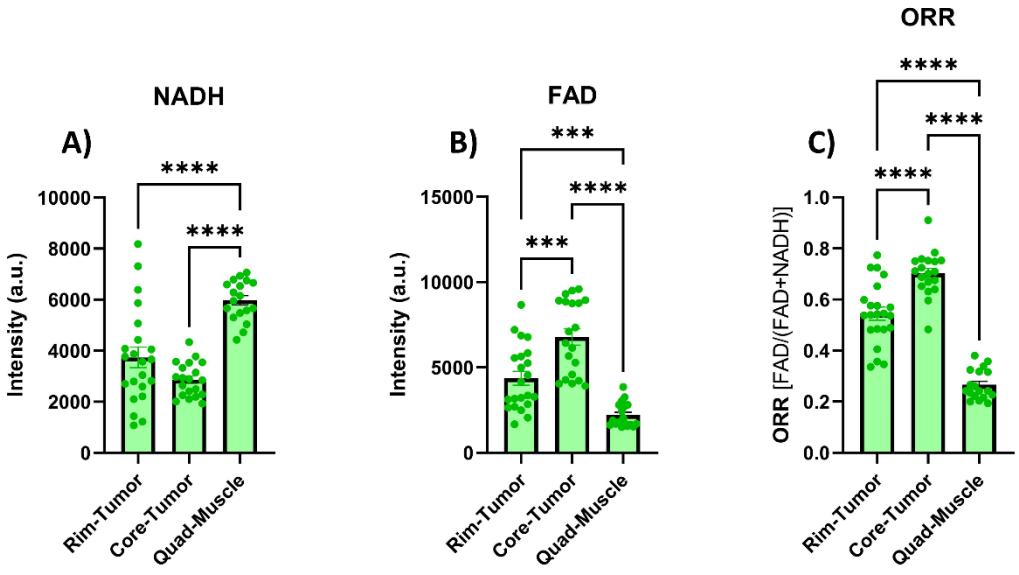

Figure 5.7: Core and rim tumor imaging
a) NADH b) FAD and c) ORR readings for MDA-MB-231 tumors and mice quadricep tissue.

Figure 5.8 shows the endoscopic signal obtained from tumor tissue that has been injected with BPD and treated with 690nm light at an irradiance and radiant exposure of 100mW/cm^2 and 100J/cm^2 respectively. The control mice were injected with BPD, but no exposure was performed. In addition, for both the experimental and control groups, the muscle tissue was not exposed to the 690nm laser light. Figures 5.8a demonstrated an increase of 39% NADH in the rim of the tumor ($p = 0.015$) as well as an increase in NADH signal of 46% in the core of the tumor after PDT

exposure, but this difference was non-significant ($p = 0.08$). In Figure 5.8b, the FAD signal on the rim demonstrated a non-significant drop of 17%, while the core saw a significant jump in signal of 25% after PDT activation. Figure 5.8c shows that the calculated ORR in the rim dropped after PDT treatment by 23%, while the core demonstrated a non-significant drop in ORR of 8% after PDT activation. And when comparing the control and experimental quadricep tissue, no significant difference was seen between the control and experimental groups. In addition, in Figure 5.8d, we can see an example of a mouse being irradiated with 690nm light, while Figure 5.8e demonstrates a representative color image of tumor pieces that were imaged using the endoscope. Figure 5.8f is a fluorescent image looking at the accumulation of BPD in the tumor, with the concentration of BPD in the tumor being calculated at 830±120nM.

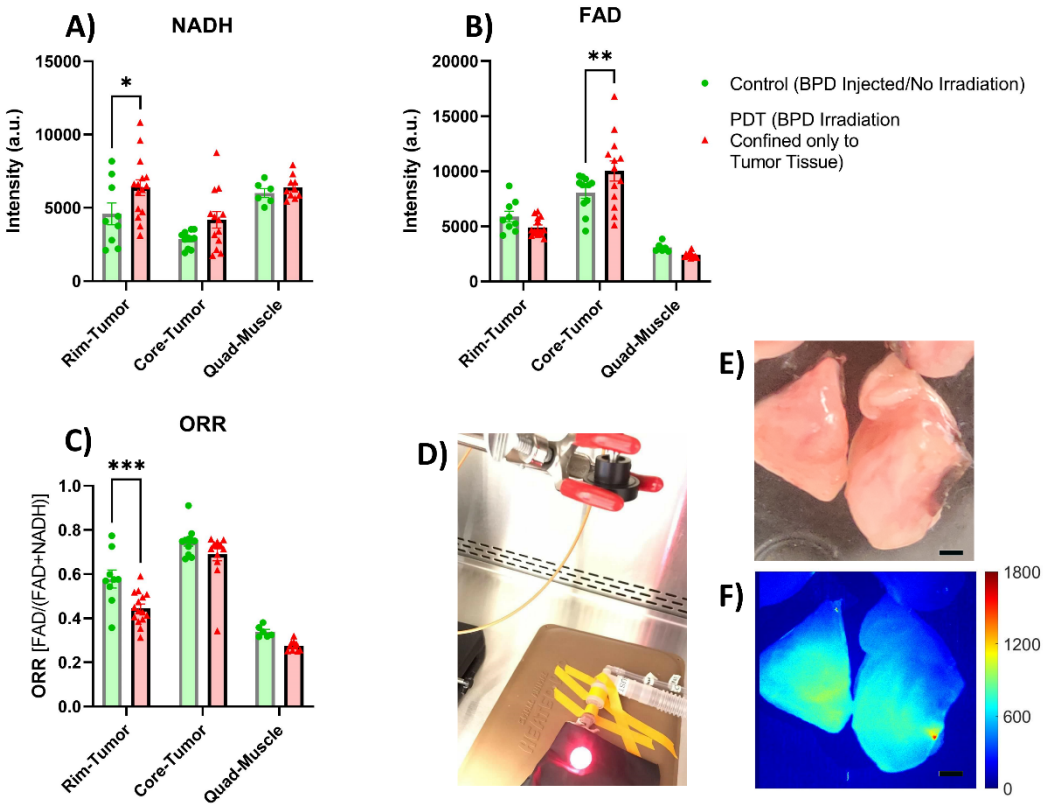

Figure 5.8: PDT treatment of mouse tumor and subsequent endoscopic imaging
a) NADH b) FAD and c) ORR readings for MDA-MB-231 tumors that have been exposed to a 690nm laser light and100J/cm^2 (red), except for the muscle tissue which was not exposed. The control mice (green) were injected with BPD, but not exposed to the 690nm laser light. We also see an d) image of a tumor being exposed to the 690nm laser light. In e) we see a color image of a subdivided tumor and in f) we see the BPD fluorescence in the tumor, with the color bar representing the concentration of BPD in nM. The black scale bar is equal to 1.5mm.

5.4 Discussion

5.4.1 Phantom Device Validation

The initial validation of the endoscopic device demonstrates that we can detect NADH and FAD present in a scattering medium similar to that of tissue, along with having penetration depths between 600-3000µm depending on the excitation channel, although this is likely a slight overestimation in penetration depth since we

only took into account scattering, and at wavelengths in the UV/blue range, blood absorption is high, limiting penetration depth [168, 249]. The NADH channel was found to have a LOD of 44μM, and the FAD channel was found to have a LOD of 1.3μM at an exposure time of 1000ms. The signal obtained from the NADH channel is low likely due to the endoscope using an excitation wavelength of 375nm when NADH has a central wavelength of 335nm, as seen in Figure 5.1a. Although this excitation wavelength does allow us to image NADH, due to the off-peak excitation, the generated fluorescence is potentially reduced by 67% when comparing the absorption fractions at 335nm and 375nm. Although exciting at 335nm is ideal, the reason an excitation of 375nm was chosen was due to the limitations of UV lasers. UV lasers that can excite at wavelengths closer to 335nm have a larger footprint when it comes to laser heads and controller boxes. For example, a Duetto 349 UV laser head has a surface area (length x width) of 363cm^2, while the 375nm laser we used had a surface area of 45cm^2 (this includes the temperature-controlled mount) which is an 88% reduction in size. In addition, with a LOD of 42μM, NADH should still be able to detect normal tissue and tumor tissue since previous work has demonstrated that in normal tissue, NADH has an average concentration of 84μM, while tumor tissue has a concentration of 217μM [224]. FAD's LOD is also sensitive enough to differentiate between normal tissue and tumor tissue, with a LOD of 1.3μM, whereas patient samples were found to have an average FAD concentration of 83μM and 308μM for normal and tumor tissue, respectively [224].

Another issue that needs to be addressed is FAD's nonlinearity. As discussed in section 5.3, after reaching a concentration of 100μM, the FAD's linearity begins to

decrease. This is likely due to the inherent quenching of FAD, leading to a decrease in fluorescence as concentrations get higher in the solution. The reason for this quenching is believed to be due to the photoreduction of oxidized flavoquinon, with the attached adenine acting as a reducing agent [250, 251]. This mechanism has been found to lead to a decrease in absorption, which leads to a corresponding decrease in fluorescence, with this mechanism being exasperated depending on environmental conditions such as pH.

To further validate the endoscopic system, we compared NADH and FAD phantoms to the Chance scanner. As mentioned in section 5.1, the Chance scanner is an imaging system used specifically to image NADH and FAD in tissue by freezing tissue, milling it flat, and raster scanning the surface with a probe. This method of imaging NADH and FAD has become a standard and well-accepted imaging method, being used in several studies to obtain information about the NADH and FAD distribution [224-226, 228-233]. The NADH and FAD phantoms demonstrated good linearity when comparing the signals between the endoscope and the Chance scanner, which can be seen in Figure 5.4e/f. The NADH signals across both systems demonstrate the same linear pattern, while the FAD signals on both systems demonstrated a drop in linear response after 16μM. An aspect that must be noted is that the NADH and FAD signals obtained from the endoscope during this comparison are higher than the signals obtained under normal conditions, to the point where we had to use a smaller power and exposure time to avoid potential saturation with the sensor, with this being especially true for the NADH channel. The main reason for this is that the endoscope imaged the NADH and FAD phantoms under the same

conditions as the Chance scanner, which involves imaging at temperatures of -80ºC, and at these low temperatures, NADH and FAD can increase their fluorescent signal up to x10 [252].

5.4.2 *Ex vivo* tissue measurements

To ensure that the endoscope could image NADH and FAD signals, tissue modulations were performed using FCCP and rotenone/antimycin A. FCCP is a mitochondrial uncoupler that has been found to decrease NADH concentration, increase FAD concentration, and increase the ORR when added to the tissue [41, 253, 254]. On the opposite end, rotenone and antimycin A inhibit complex 1 and 3 respectively, typically leading to a rise in NADH concentration, a fall in FAD concentration, and a fall in the ORR [41, 253-255]. The results that we have obtained follow the previously established trends, except for the concentration of NADH when going from FCCP to rotenone/antimycin A. After moving the tumor tissue from the FCCP solution to rotenone/antimycin A solution, we would expect a drop in NADH concentration, while in the figure we see no concentration change. Although the trends we see do align with what has been previously published, it must be noted that these changes are not significant, except for the ORR signals when transitioning between going from the glucose solution to the FCCP.

The tumor core and tumor rim were imaged because, in MDA-MB-231 cell lines, tumor cores have been found to have a lower NADH, higher FAD, and a higher ORR signal compared to the tumor rim [225]. The exact reason for this core-rim differential is not yet known, but there is some evidence that the tumor core is more aggressive, being exposed to less oxygen than the rim, and potentially having

damaged blood vessels [225, 256]. Previous work has described five metabolic states that can be determined through the measurement of NAD, FAD, and the calculated ORR. For example, state 2 can be identified when the NADH concentration is low, and the FAD concentration is high [a high redox ratio], which means that the tissue is likely being starved of necessary substrates. State 4 on the other hand, corresponds to a high NADH and low FAD concentration [a low redox ratio], meaning that the tissue is in a resting state and has plenty of nutrients and oxygen [42, 43]. The core, due to having (potentially) fewer substrates and being poorly perfused, could be in state 2, leading to a high NADH signal, low FAD signal, and high ORR. On the other hand, the rim is likely supplied with more nutrients and oxygen than the core, leading to a larger NADH signal, lower FAD signal, and lower ORR, which was seen in previous studies when looking at aggressive cancers [225, 256]. In addition, prior studies have demonstrated that muscle tissue is much more reduced (lower ORR) than most other tissue [241, 257-259], which is backed up by the results obtained using our endoscope, where the NADH signal was larger and FAD signal was lower than that of both the tumor core and rim, which led to an overall lower ORR than the tumor tissue.

In this study, we also look into the NADH, FAD, and ORR changes that occur after PDT treatment. After the PDT excitation, we saw an increase in NADH signal from the tumor rim and core, although the change to the tumor core was non-significant. Previous work has demonstrated that the inhibition of lactate dehydrogenase (LDH), which causes the interconversion between lactate and pyruvate, can cause a decrease in NADH signal detected in cells [38], with work also

demonstrating that LDH leakage can be caused through cellular necrosis [260], with PDT activation demonstrating an increase in LDH leakage [261, 262]. This trend of an increase in NADH signal and a non-significant decrease in FAD signal that leads to a decrease in ORR can also be linked to a hypoxic environment produced by PDT. PDTs main method of toxicity is the conversion of O_2 into a more reactive form of oxygen (SO, superoxides, etc.). This oxygen consumption leads to a more oxygen deprived environment, decreasing oxidative phosphorylation and increasing glycolysis to create ATP, as oxygen is needed to drive the election transport chain, acting as an electron acceptor. Although it must be noted that previous studies investigating PpIX have previously demonstrated decreases in NADH after PDT activation [44, 263]. The FAD channel demonstrated a non-significant drop in FAD in the rim, while the core showed a significant 25% rise in signal, with some prior studies demonstrating an increase in FAD when RMS are introduced into the cellular environment [38, 264]. The mouse quadricep tissue demonstrates no significant difference, which falls in line with expected results since most of the BPD is expected to accumulate in the tumor and compared to muscles tissue [265], and the mouse quadriceps were not exposed to the activation light, so the results are expected to be the same in the control and experimental groups.

In all of the ex-vivo measurements, we also see a larger variation in the tumor signal, especially when comparing the quadriceps tissue. This can be explained through mouse quadriceps tissue signal for NADH and FAD being relatively homogenous and stable across different mice, with standard deviations between 2-17μM [257]. Tumor tissue, especially MDA-MB-231 cell lines, have demonstrated a

great amount of heterogeneity, and NADH/FAD concentrations vary from 27μM to 127μM [225].

5.4.3 Limitations and future work

Although the system can image NADH and FAD in tissue, there are still limitations and potential future optimizations that can be performed. One such issue is the limitations of the spatial resolution of the system. Although under ideal conditions, a resolution of 11μm could be reached for the NADH and FAD channels, this resolution is not representative of the resolution of the endoscope when used on tissue. This is likely due to two main reasons. One is that when imaging thick tissue samples out of plane fluorescence can lead to out-of-focus signals causing a decrease in resolution [197]. The second reason is the source-detector separation of the excitation and emission fibers. These source-detector separations lead to light passing through deeper parts of tissue, leading to more re-scattered light/fluorescence to be picked up by the detector, leading to a drop in resolution [30, 260, 266]. Another limitation of the system is the low signal obtained from the NADH channel. Although at the moment, there is no potential laser replacement, as UV laser technology continues to advance, a smaller and more cost-effective UV laser system may be available for a future iteration of the endoscopic system, or potentially, a UV-LED may be used, although the endoscope design would need to be altered to accommodate the use of an LED rather than a laser since LED's are more difficult to couple to lenses.

Future work with the endoscopic device will involve not just comparing tumor tissue to mouse quadricep tissue, but imaging cancers of varying aggressiveness levels. This can include the testing and comparison of the very aggressive MDA-MB-231 cell line to less metastatic cell lines such as MCF-7 or 67NR. These comparisons would allow us to determine if the endoscope can not only differentiate between normal and tumor tissue, but also different aggressiveness levels. Another area to test is longer drug-light intervals, as our initial test does demonstrate that we can detect PDT activation, but longer-term studies need to be performed to test the ability of the endoscope to image and inform longer-term treatment response, ensuring that the treatment is taking effect. In addition, an updated endoscope can be developed to not only image NADH and FAD, but also to image/activate PDT through the addition of a separate laser system specifically to excite a photosensitizer of choice, since optical fibers are a common way to excite photosensitizers in the clinic. In addition, it would allow for the simultaneous imaging of a photosensitizer, giving the clinician the ability to localize PDT distribution in tissue, activate, and determine treatment efficacy using a single system.

5.5 Conclusion

In this study, we developed an endoscopic imaging system to image NADH and FAD in tissue. We found that the endoscopic system had a LOD of 44μM and 1.3μM for the FAD and NADH channels respectively. Comparisons to the Chance scanner demonstrated a high degree of linearity. In addition, our modulation results and MDA-MB-231 measurements align with previously published results. We also

found that the endoscope could measure the metabolic impacts of PDT activation, finding that for the MDA-MB-231 cell line there was an increase of NADH and a non-significant decrease in FAD in the rim, as well as a non-significant decrease of NADH and an increase of FAD in the core. Future work will focus on increasing the sensitivity of the NADH channel, imaging the change in NADH and FAD for longer periods after PDT treatments to investigate how a tumor responds metabolically to treatment in the long term, and integrating a PDT imaging/activation channel to the newly developed endoscope.

Chapter 6: Conclusion and Future Directions

6.1 Summary

In chapter 1 we presented the significance of this work to aid in the characterization of photosensitizer and PDT treatment, as well as going over important background. We also presented the goals and objectives for each chapter.

In chapter 2 we demonstrated a newly developed method to quantify the amount of SO produced by a fluorophore and photosensitizer using SOSG. This method takes into account the clinical conditions, such as concentration, irradiance, and radiant exposure when determining the phototoxicity levels, allowing for the direct comparison of the potential SO created by specific fluorophores under specific conditions. This allows for the rapid screening of the phototoxic potential of photosensitive probes under clinical conditions.

In chapter 3, we developed another method to compare the potential depth penetration of photosensitizers in the brain. We specifically focused on the testing and comparison of PpIX and BPD. Out results indicate that PpIX can be activated up to 1cm into the tissue when excited with 630nm light, while BPD can be activated up to 1.5cm in the brain when activated at 690nm, with both photosensitizers being activated at the same radiant exposure of $40 J/cm^2$. This same methodology can be used to quickly quantify the effective depth penetration of other photosensitizers of interest.

Chapter 4 looks into using the FLOT system to better map photosensitizer distribution in tissue, with this study focusing on determining photosensitizer

distribution in the brain. We also compared the imaging system to 2D imaging. We found that, when imaging in 2D, the imaging depth was limited to 334μm, while the FLOT system's imaging depth was able to reach 591μm, demonstrating the FLOT's ability to better image photosensitizers in the brain.

In Chapter 5 we developed an endoscopic imaging system to image the metabolic markers NADH and FAD in tumor tissue and determine the effects that PDT has on tumor metabolism. Our endoscope system was found to have a LOD of 44μM and 1.3μM for the NADH and FAD channels respectively. The endoscope also was able to detect an increase in NADH of 39% in the rim of the tumor and a jump in signal of 25% in FAD in the core of the tumor after PDT activation, with these changes potentially being due to the change in oxygenation and LDH caused by PDT treatment. The ability of the endoscope to measure these metabolic signals demonstrates its potential use to ensure that PDT has been activated and that the treatment has been effective.

6.2 Future Work

6.2.1 *In vitro/vivo* phototoxicity testing of potential fluorophores and photosensitizers

Several methods have been implemented to evaluate phototoxicity, with current guidance documents provided by CDER/ CBER recommending the use of *in vitro* 3T3-NRU Phototoxicity Test to assess the potential phototoxicity of drugs, including fluorescent probes [267]. This test evaluates phototoxicity by mapping the reduction of viable cells exposed to the compound of interest when exposed to light

and comparing the results to dark controls. This assay functions because when RMS is generated there is a reduction in the pH gradient, which increases the permeability of the lysosomal membrane. This leads to a decreased uptake and accumulation of NR, which helps to distinguish viable and damaged/dead cells.

Current guidance for *in vitro* phototoxicity evaluation, which is defined in the OECD 432 guidance document, recommends using a fixed radiant exposure ($5J/cm^2$) and wavelengths between 290-700nm, which are emitted by a solar simulator to test for potential phototoxic effects. While solar sensitivity is a concern, the growing use of fluorescent and photodynamic probes in the clinic means that now there exists the potential for photochemical damage to tissues and/or organs during intraoperative/ endoscopic imaging procedures is a possibility that must be accounted for. Because of this, the goal of future work is to address the lack of standardized testing methodologies for assessing the phototoxicity of photoreactive chemicals and to evaluate the utility of the 3T3 NRU phototoxicity assay under clinical conditions.

Another future direction is investigating the in-vivo distribution of RMS to better study tissue level distribution and determine how this can affect potential toxicity. Previous work has used Cell-ROX Deep Red to measure RMS *in vivo,* which fluoresces after binding to RMS [268]. This would allow for a better understanding of the quantity and distribution of RMS in tissue and the impact that this can have on toxicity.

6.2.2 Development of a compact FLOT system for real-time clinical imaging

Because we have demonstrated the FLOT's ability to image photosensitizers in the brain, the next step is to make a more clinically compatible version of the FLOT system. This would involve reducing the footprint of the FLOT system and integrating it with an existing imaging system that clinicians are accustomed to, with exoscopes being one such example.

Exoscopes are highly flexible imaging systems, capable of imaging with a large field of view and a high resolution. This system focuses a CCD on the areas of interest, with the CCD being attached to a stereotactic frame. These microscopes have gained popularity since they can give a clinician a high-resolution image, variable zoom without adjusting the working distance, and hand-free controls using foot pedals [269, 270]. By integrating the FLOT system into an exoscopic system, it would allow for the ability to image photosensitizers more quantitatively and in a more clinically friendly format.

In addition, we will look into the benefit of performing additional resection with the FLOT. This will be accomplished by implanting a diffusive tumor cell line into the mouse brain, performing a resection on the bulk tumor, and then imaging the margins with the FLOT and 2D imaging system. After performing resection, we would then look at recurrence and overall survival of the mice, allowing us to determine the effectiveness of using the FLOT system in a surgical setting.

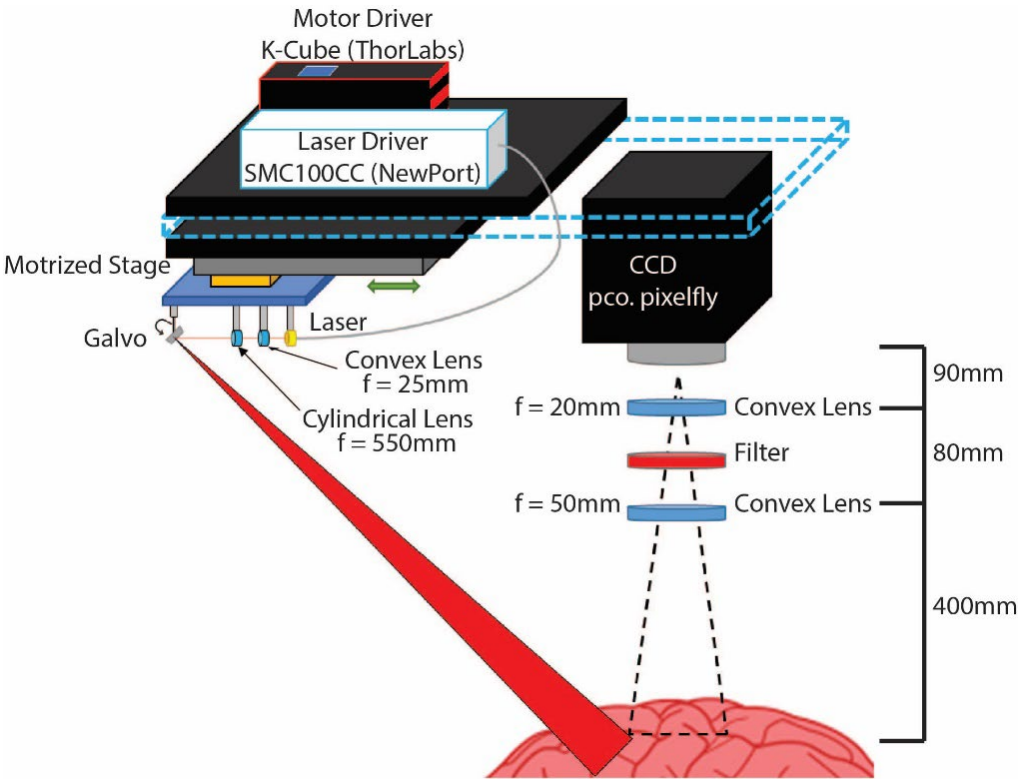

Figure 6.1: Exoscopic FLOT Schematic
A schematic for a miniaturized version of the FLOT system that can be attached to an exoscope for co-registered FLOT and color widefield imaging.

6.2.3 Design and implementation of an endoscopic metabolic imaging device with simultaneous PDT activation

Because of the ability of NADH and FAD to not only help in cancer detection but also to give information on changes in cell metabolism due to external factors such as treatment response, future work will focus on developing a metabolic imaging endoscope that can aid in the localization of cancer, as well as provide real-time feedback on treatments performed on said cancerous tissue. The new system would have excitation and emission channels to excite the NADH and FAD, just like the current system. In addition, this endoscope would contain a treatment activation channel that can be used to excite and image a third fluorophore or activate a

therapeutic agent such as a photodynamic or photothermal agent. Through the construction of this device, we would not only be able to image and activate therapeutic agents but also measure how the tissue is responding to said treatment, allowing for real-time treatment adjustments.

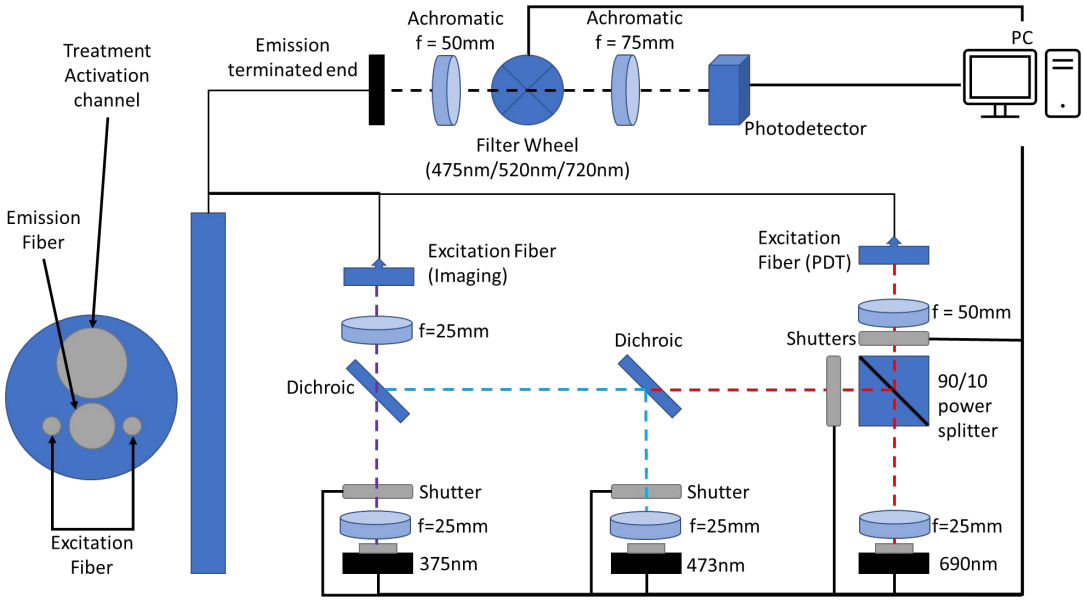

Figure 6.2: Schematic of metabolic and PDT imaging/activation device
Schematic for an endoscopic device to measure NADH and FAD, as well as image and activate a photosensitizer(lasers and filters in this schematic are geared towards BPD activation).

Publications

B. Konkel, C. Lavin, T. Wu, E. Anderson, A. Iwamoto, H. Rashid, **B. Gaitan**, J. Boone, M. Cooper, P. Abrams, A. Gilbert, Q. Tang, M. Levi, J. Fujimoto, P. Andrews, Y. Chen, "Fully automated analysis of OCT imaging of human kidneys for prediction of post-transplant function", *Bio. Opt. Exp.*, vol. 10, pp.1794-1821, Apr 2019, doi: 0.1364/BOE.10.001794

C. Inglut, **B. Gaitan**, D. Najafali, I. A. Lopez, N. P. Connolly, S. Orsila, R. Perttilä, G. F. Woodworth, Y. Chen, H. Huang, "Predictors and Limitations of the Penetration Depth of Photodynamic Effects in the Rodent Brain", *Photochemistry and Photobiology*, vol. 96, pp. 301-309, Mar 2020, doi: 10.1111/php.13155 , *Co-first author*

B. Gaitan, C. T. Inglut, Y. Liu, Y. Chen, and H. C. Huang, "Depth-resolved imaging of photosensitizer in the rodent brain using fluorescence laminar optical tomography," *J. Biomed. Opt.*, vol. 25, pp. 096007, Sep 2020, doi: 10.1117/1.JBO.25.9.096007

Z. Chen, V. Tsytsarev, Y. Finfrock, O. Antipova, Z. Cai, H. Arakawa, F. Lischka, B. Hooks, R. Wilton, D. Wang, Y. Liu, **B. Gaitan**, Y. Tao, Y. Chen, R. Erzurumlu, H. Yang, E. Rozhkova, "Wireless optogenetic modulation of cortical neurons enabled by radioluminescent nanoparticles", vol.15, pp.5201-5208, *ACS nano*, Feb 2021, doi: 10.1021/acsnano.0c10436

X. Qin, B. Wang, D. Boegner, **B. Gaitan**, Y. Zheng, X. Du, Y. Chen, "Indoor localization of hand-held OCT probe using visual odometry and real-time segmentation using deep learning", vol. 69, pp. 1378-1385, *IEEE Trans. on Bio. Eng.*, Sep 2021, doi: 0.1109/TBME.2021.3116514

B. Gaitan, L. Frankel, S. Vig, E. Oskoui, M. Adwan, Y. Chen, R. Elespuru, H. Huang, J. Pfefer., "Quantifying the Photochemical Damage Potential of Contrast-Enhanced Fluorescence Imaging Products: Singlet Oxygen Production", *Photochemistry and Photobiology*, 2022, doi: 10.1111/php.13638, *Accepted*

J. Yang, C. Ma, **B. Gaitan**, A. Farooqui, H. Huang, J. L. Mueller, "Leveraging photosensitizers to monitor local delivery of ethyl cellulose-ethanol and enable photodynamic therapy in tissues", *JOVE*, 2022, *Submitted*

B. Gaitan, C. Inglut, U. Kanniyappan, H. Xu, L. Li, Y. Chen, H. Huang, "Development of an endoscopic auto-fluorescent sensing device to aid in the detection of breast cancer and inform PDT treatment", *To be Submitted*

S. Vig, **B. Gaitan**, L. Frankle, K. Kruger, Y. Chen, R. Elespuru, J. Pfefer, H. Huang "In-vitro phototoxicity assessment of clinical fluorescent imaging products.", *To be Submitted*

C. Inglut, J. Quinlan, I. Rahman, J. Stable1, **B. Gaitan**, P. Srivastava, W. Chiou, B. Karim, N. Connolly, R. Robey, G. Woodworth, M. G. Gottesman, H. Huang, "Amorphous verteporfin nanosuspensions for photodynamic cancer therapy and brain drug delivery", *To be Submitted*

Bibliography

[1] R. L. Siegel, K. D. Miller, H. E. Fuchs, and A. Jemal, "Cancer Statistics, 2021," *CA Cancer J Clin,* vol. 71, no. 1, pp. 7-33, Jan 2021, doi: 10.3322/caac.21654.

[2] Y. S. Sun *et al.*, "Risk Factors and Preventions of Breast Cancer," *Int J Biol Sci,* vol. 13, no. 11, pp. 1387-1397, Dec 2017, doi: 10.7150/ijbs.21635.

[3] T. Tykocki and M. Eltayeb, "Ten-year survival in glioblastoma. A systematic review," *J Clin Neurosci,* vol. 54, pp. 7-13, Aug 2018, doi: 10.1016/j.jocn.2018.05.002.

[4] T. J. Wilt *et al.*, "Radical prostatectomy versus observation for localized prostate cancer," *N Engl J Med,* vol. 367, no. 3, pp. 203-213, Jul 2012, doi: 10.1056/NEJMoa1113162.

[5] F. C. Hamdy *et al.*, "10-Year Outcomes after Monitoring, Surgery, or Radiotherapy for Localized Prostate Cancer," *N Engl J Med,* vol. 375, no. 15, pp. 1415-1424, Oct 2016, doi: 10.1056/NEJMoa1606220.

[6] M. T. Puts *et al.*, "A systematic review of factors influencing older adults' decision to accept or decline cancer treatment," *Cancer Treat Rev,* vol. 41, no. 2, pp. 197-215, Feb 2015, doi: 10.1016/j.ctrv.2014.12.010.

[7] R. Stupp *et al.*, "Effects of radiotherapy with concomitant and adjuvant temozolomide versus radiotherapy alone on survival in glioblastoma in a randomised phase III study: 5-year analysis of the EORTC-NCIC trial," *Lancet Oncol,* vol. 10, no. 5, pp. 459-466, May 2009, doi: 10.1016/S1470-2045(09)70025-7.

[8] M. M. Chowdhary, C. I. Ene, and D. L. Silbergeld, "Treatment of Gliomas: How did we get here?," *Surg Neurol Int,* vol. 6, no. Suppl 1, pp. 85-88, Feb 2015, doi: 10.4103/2152-7806.151348.

[9] G. Laustriat, "Molecular mechanisms of photosensitization," *Biochimie,* vol. 68, no. 6, pp. 771-778, Jun 1986, doi: 10.1016/s0300-9084(86)80092-x.

[10] H. Y. Wu, Q. J. Song, G. X. Ran, X. M. Lu, and B. G. Xu, "Recent developments in the detection of singlet oxygen with molecular spectroscopic methods," *Trac-Trend Anal Chem,* vol. 30, no. 1, pp. 133-141, Jan 2011, doi: 10.1016/j.trac.2010.08.009.

[11] T. C. Zhu *et al.*, "Comparison of singlet oxygen threshold dose for PDT," Feb 2014: SPIE, doi: 10.1117/12.2039719.

[12] M. M. Kim, A. A. Ghogare, A. Greer, and T. C. Zhu, "On the in vivo photochemical rate parameters for PDT reactive oxygen species modeling," *Phys Med Biol,* vol. 62, no. 5, pp. R1-R48, Mar 2017, doi: 10.1088/1361-6560/62/5/R1.

[13] E. de Boer *et al.*, "Biodistribution Study of Intravenously Injected Cetuximab-IRDye700DX in Cynomolgus Macaques," *Mol Imaging Biol,* vol. 18, no. 2, pp. 232-242, Apr 2016, doi: 10.1007/s11307-015-0892-y.

[14] P. Cramers, M. Ruevekamp, H. Oppelaar, O. Dalesio, P. Baas, and F. A. Stewart, "Foscan uptake and tissue distribution in relation to photodynamic

efficacy," *Br J Cancer,* vol. 88, no. 2, pp. 283-290, Jan 2003, doi: 10.1038/sj.bjc.6600682.
[15] S. S. Dhillon *et al.*, "A Phase I Study of Light Dose for Photodynamic Therapy Using 2-[1-Hexyloxyethyl]-2 Devinyl Pyropheophorbide-a for the Treatment of Non-Small Cell Carcinoma In Situ or Non-Small Cell Microinvasive Bronchogenic Carcinoma: A Dose Ranging Study," *J Thorac Oncol,* vol. 11, no. 2, pp. 234-241, Feb 2016, doi: 10.1016/j.jtho.2015.10.020.
[16] J. Cassidy, V. Betz, and L. Lilge, "Treatment plan evaluation for interstitial photodynamic therapy in a mouse model by Monte Carlo simulation with FullMonte," *Front Phys,* Methods vol. 3, Feb 2015, doi: 10.3389/fphy.2015.00006.
[17] C. Dupont, A. S. Vignion, S. Mordon, N. Reyns, and M. Vermandel, "Photodynamic therapy for glioblastoma: A preliminary approach for practical application of light propagation models," *Lasers Surg Med,* vol. 50, no. 5, pp. 523-534, Jul 2018, doi: 10.1002/lsm.22739.
[18] L. H. Murrer, J. P. Marijnissen, and W. M. Star, "Light distribution by linear diffusing sources for photodynamic therapy," *Phys Med Biol,* vol. 41, no. 6, pp. 951-961, Jun 1996, doi: 10.1088/0031-9155/41/6/001.
[19] J. M. Dąbrowski, "Reactive Oxygen Species in Photodynamic Therapy: Mechanisms of Their Generation and Potentiation," in *Inorganic Reaction Mechanisms*, Advances in Inorganic Chemistry: Elsevier, 2017, pp. 343-394.
[20] J. J. Bravo, J. D. Olson, S. C. Davis, D. W. Roberts, K. D. Paulsen, and S. C. Kanick, "Hyperspectral data processing improves PpIX contrast during fluorescence guided surgery of human brain tumors," *Sci Rep,* vol. 7, no. 1, p. 9455, Aug 2017, doi: 10.1038/s41598-017-09727-8.
[21] J. Guyotat, J. Pallud, X. Armoiry, V. Pavlov, and P. Metellus, "5-Aminolevulinic Acid-Protoporphyrin IX Fluorescence-Guided Surgery of High-Grade Gliomas: A Systematic Review," *Adv Tech Stand Neurosurg,* no. 43, pp. 61-90, Jan 2016, doi: 10.1007/978-3-319-21359-0_3.
[22] S. Utsuki *et al.*, "Fluorescence-guided resection of metastatic brain tumors using a 5-aminolevulinic acid-induced protoporphyrin IX: pathological study," *Brain Tumor Pathol,* vol. 24, no. 2, pp. 53-55, Dec 2007, doi: 10.1007/s10014-007-0223-3.
[23] S. Magder, "Reactive oxygen species: toxic molecules or spark of life?," *Crit Care,* vol. 10, no. 1, p. 208, Feb 2006, doi: 10.1186/cc3992.
[24] B. Halliwell and J. M. C. Gutteridge, *Free Radicals in Biology and Medicine*, 5 ed. Oxford: Oxford University Press, 2015, p. 944.
[25] F. Yamakura, H. Taka, T. Fujimura, and K. Murayama, "Inactivation of human manganese-superoxide dismutase by peroxynitrite is caused by exclusive nitration of tyrosine 34 to 3-nitrotyrosine," *J Biol Chem,* vol. 273, no. 23, pp. 14085-14089, Jun 1998, doi: 10.1074/jbc.273.23.14085.
[26] K. Plaetzer, B. Krammer, J. Berlanda, F. Berr, and T. Kiesslich, "Photophysics and photochemistry of photodynamic therapy: fundamental aspects," *Lasers in Medical Science,* vol. 24, no. 2, pp. 259-268, Mar 2009, doi: 10.1007/s10103-008-0539-1.

[27] S. S. Cho *et al.*, "Intraoperative near-infrared imaging with receptor-specific versus passive delivery of fluorescent agents in pituitary adenomas," *Journal of Neurosurgery JNS,* vol. 131, no. 6, pp. 1974-1984, Dec 2019, doi: 10.3171/2018.7.Jns181642.
[28] J. Bartosová and Z. Hrkal, "Accumulation of protoporphyrin-IX (PpIX) in leukemic cell lines following induction by 5-aminolevulinic acid (ALA)," *Comp Biochem Physiol C Toxicol Pharmacol,* vol. 126, no. 3, pp. 245-252, Jul 2000, doi: 10.1016/s0742-8413(00)00125-0.
[29] K. Sato *et al.*, "Photoimmunotherapy: comparative effectiveness of two monoclonal antibodies targeting the epidermal growth factor receptor," *Mol Oncol,* vol. 8, no. 3, pp. 620-632, May 2014, doi: 10.1016/j.molonc.2014.01.006.
[30] G. E. Strangman, Z. Li, and Q. Zhang, "Depth sensitivity and source-detector separations for near infrared spectroscopy based on the Colin27 brain template," *PLoS One,* vol. 8, no. 8, p. e66319, Aug 2013, doi: 10.1371/journal.pone.0066319.
[31] Q. Tang, J. Lin, V. Tsytsarev, R. S. Erzurumlu, Y. Liu, and Y. Chen, "Review of mesoscopic optical tomography for depth-resolved imaging of hemodynamic changes and neural activities," *Neurophotonics,* vol. 4, no. 1, p. 011009, Jan 2017, doi: 10.1117/1.NPh.4.1.011009.
[32] R. Yao, X. Intes, and Q. Fang, "Direct approach to compute Jacobians for diffuse optical tomography using perturbation Monte Carlo-based photon "replay"," *Biomed Opt Express,* vol. 9, no. 10, pp. 4588-4603, Oct 2018, doi: 10.1364/BOE.9.004588.
[33] Q. Fang and D. A. Boas, "Monte Carlo simulation of photon migration in 3D turbid media accelerated by graphics processing units," *Opt Express,* vol. 17, no. 22, pp. 20178-20190, Oct 2009, doi: 10.1364/OE.17.020178.
[34] Q. Tang *et al.*, "High-dynamic-range fluorescence laminar optical tomography (HDR-FLOT)," *Biomed Opt Express,* vol. 8, no. 4, pp. 2124-2137, Apr 2017, doi: 10.1364/BOE.8.002124.
[35] Q. Tang *et al.*, "3D mesoscopic fluorescence tomography for imaging micro-distribution of antibody-photon absorber conjugates during near infrared photoimmunotherapy in vivo," *J Control Release,* vol. 279, pp. 171-180, Jun 2018, doi: 10.1016/j.jconrel.2018.04.027.
[36] Q. Tang *et al.*, "In Vivo Mesoscopic Voltage-Sensitive Dye Imaging of Brain Activation," *Sci Rep,* vol. 6, p. 25269, Apr 2016, doi: 10.1038/srep25269.
[37] R. Dumollard, P. Marangos, G. Fitzharris, K. Swann, M. Duchen, and J. Carroll, "Sperm-triggered [Ca2+] oscillations and Ca2+ homeostasis in the mouse egg have an absolute requirement for mitochondrial ATP production," *Development,* vol. 131, no. 13, pp. 3057-3067, Jul 2004, doi: 10.1242/dev.01181.
[38] A. Podsednik, A. Jacob, L. Z. Li, and H. N. Xu, "Relationship between Optical Redox Status and Reactive Oxygen Species in Cancer Cells," *React Oxyg Species (Apex),* vol. 9, no. 26, pp. 95-108, Mar 2020.
[39] A. Mayevsky and G. G. Rogatsky, "Mitochondrial function in vivo evaluated by NADH fluorescence: from animal models to human studies," *Am J Physiol*

Cell Physiol, vol. 292, no. 2, pp. C615-640, Feb 2007, doi: 10.1152/ajpcell.00249.2006.

[40] K. A. Foster, C. J. Beaver, and D. A. Turner, "Interaction between tissue oxygen tension and NADH imaging during synaptic stimulation and hypoxia in rat hippocampal slices," *Neuroscience,* vol. 132, no. 3, pp. 645-657, Apr 2005, doi: 10.1016/j.neuroscience.2005.01.040.

[41] K. Alhallak, L. G. Rebello, T. J. Muldoon, K. P. Quinn, and N. Rajaram, "Optical redox ratio identifies metastatic potential-dependent changes in breast cancer cell metabolism," *Biomed Opt Express,* vol. 7, no. 11, pp. 4364-4374, Nov 2016, doi: 10.1364/BOE.7.004364.

[42] K. Pye and B. Chance, "Sustained sinusoidal oscillations of reduced pyridine nucleotide in a cell-free extract of Saccharomyces carlsbergensis," *Proc Natl Acad Sci U S A,* vol. 55, no. 4, pp. 888-894, Apr 1966, doi: 10.1073/pnas.55.4.888.

[43] B. Chance and H. Baltscheffsky, "Respiratory enzymes in oxidative phosphorylation. VII. Binding of intramitochondrial reduced pyridine nucleotide," *J Biol Chem,* vol. 233, no. 3, pp. 736-739, Sep 1958, doi: 10.1016/S0021-9258(18)64738-6.

[44] G. C. Su, Y. H. Wei, and H. W. Wang, "NADH fluorescence as a photobiological metric in 5-aminolevlinic acid (ALA)-photodynamic therapy," *Opt Express,* vol. 19, no. 22, pp. 21145-21154, Oct 2011, doi: 10.1364/OE.19.021145.

[45] M. Broekgaarden, A. L. Bulin, J. Frederick, Z. Mai, and T. Hasan, "Tracking Photodynamic- and Chemotherapy-Induced Redox-State Perturbations in 3D Culture Models of Pancreatic Cancer: A Tool for Identifying Therapy-Induced Metabolic Changes," *J Clin Med,* vol. 8, no. 9, p. 1399, Sep 2019, doi: 10.3390/jcm8091399.

[46] C. Blauth, J. Arnold, E. M. Kohner, and K. M. Taylor, "Retinal microembolism during cardiopulmonary bypass demonstrated by fluorescein angiography," *Lancet,* vol. 2, no. 8511, pp. 837-839, Oct 1986, doi: 10.1016/s0140-6736(86)92871-0.

[47] A. Manivannan, J. Plskova, A. Farrow, S. McKay, P. F. Sharp, and J. V. Forrester, "Ultra-wide-field fluorescein angiography of the ocular fundus," *Am J Ophthalmol,* vol. 140, no. 3, pp. 525-527, Sep 2005, doi: 10.1016/j.ajo.2005.02.055.

[48] J. Shinoda *et al.*, "Fluorescence-guided resection of glioblastoma multiforme by using high-dose fluorescein sodium. Technical note," *J Neurosurg,* vol. 99, no. 3, pp. 597-603, Sep 2003, doi: 10.3171/jns.2003.99.3.0597.

[49] J. R. van der Vorst *et al.*, "Near-infrared fluorescence-guided resection of colorectal liver metastases," *Cancer,* vol. 119, no. 18, pp. 3411-3418, Sep 2013, doi: 10.1002/cncr.28203.

[50] M. I. Canto, S. Setrakian, R. E. Petras, E. Blades, A. Chak, and M. V. Sivak, Jr., "Methylene blue selectively stains intestinal metaplasia in Barrett's esophagus," *Gastrointest Endosc,* vol. 44, no. 1, pp. 1-7, Jul 1996, doi: 10.1016/s0016-5107(96)70221-3.

[51] F. P. Verbeek *et al.*, "Intraoperative near infrared fluorescence guided identification of the ureters using low dose methylene blue: a first in human experience," *J Urol,* vol. 190, no. 2, pp. 574-579, Aug 2013, doi: 10.1016/j.juro.2013.02.3187.
[52] Q. R. Tummers *et al.*, "Real-time intraoperative detection of breast cancer using near-infrared fluorescence imaging and Methylene Blue," *Eur J Surg Oncol,* vol. 40, no. 7, pp. 850-858, Jul 2014, doi: 10.1016/j.ejso.2014.02.225.
[53] D. Shin, M. C. Pierce, A. M. Gillenwater, M. D. Williams, and R. R. Richards-Kortum, "A fiber-optic fluorescence microscope using a consumer-grade digital camera for in vivo cellular imaging," *PLoS One,* vol. 5, no. 6, p. e11218, Jun 2010, doi: 10.1371/journal.pone.0011218.
[54] K. Kim, H. Park, and K. M. Lim, "Phototoxicity: Its Mechanism and Animal Alternative Test Methods," *Toxicol Res,* vol. 31, no. 2, pp. 97-104, Jun 2015, doi: 10.5487/TR.2015.31.2.097.
[55] L. Huang, Y. Xuan, Y. Koide, T. Zhiyentayev, M. Tanaka, and M. R. Hamblin, "Type I and Type II mechanisms of antimicrobial photodynamic therapy: an in vitro study on gram-negative and gram-positive bacteria," *Lasers Surg Med,* vol. 44, no. 6, pp. 490-499, Aug 2012, doi: 10.1002/lsm.22045.
[56] M. Garcia-Diaz, Y. Y. Huang, and M. R. Hamblin, "Use of fluorescent probes for ROS to tease apart Type I and Type II photochemical pathways in photodynamic therapy," (in eng), *Methods,* vol. 109, pp. 158-166, Oct 2016, doi: 10.1016/j.ymeth.2016.06.025.
[57] E. R. Stadtman and R. L. Levine, "Protein oxidation," *Ann N Y Acad Sci,* vol. 899, no. 1, pp. 191-208, Jun 2000, doi: 10.1111/j.1749-6632.2000.tb06187.x.
[58] G. O. Fruhwirth and A. Hermetter, "Mediation of Apoptosis by Oxidized Phospholipids," in *Subcellular Biochemistry*: Springer Netherlands, 2008, pp. 351-367.
[59] R. L. Auten, M. H. Whorton, and S. Nicholas Mason, "Blocking neutrophil influx reduces DNA damage in hyperoxia-exposed newborn rat lung," *Am J Respir Cell Mol Biol,* vol. 26, no. 4, pp. 391-397, Apr 2002, doi: 10.1165/ajrcmb.26.4.4708.
[60] C. S. Foote, "Mechanisms of photosensitized oxidation. There are several different types of photosensitized oxidation which may be important in biological systems," *Science,* vol. 162, no. 3857, pp. 963-970, Nov 1968, doi: 10.1126/science.162.3857.963.
[61] *Singlet Oxygen* (Comprehensive Series in Photochemical & Photobiological Sciences). 2016.
[62] H. Lin *et al.*, "Feasibility study on quantitative measurements of singlet oxygen generation using singlet oxygen sensor green," *J Fluoresc,* vol. 23, no. 1, pp. 41-47, Jan 2013, doi: 10.1007/s10895-012-1114-5.
[63] L. V. Lutkus, S. S. Rickenbach, and T. M. McCormick, "Singlet oxygen quantum yields determined by oxygen consumption," *J Photoch Photobio A,* vol. 378, pp. 131-135, Jun 2019, doi: 10.1016/j.jphotochem.2019.04.029.
[64] I. Pathak, N. L. Davis, Y. N. Hsiang, N. F. Quenville, and B. Palcic, "Detection of squamous neoplasia by fluorescence imaging comparing

porfimer sodium fluorescence to tissue autofluorescence in the hamster cheek-pouch model," *Am J Surg,* vol. 170, no. 5, pp. 423-426, Nov 1995, doi: 10.1016/s0002-9610(99)80321-3.

[65] M. Sachar, K. E. Anderson, and X. Ma, "Protoporphyrin IX: the Good, the Bad, and the Ugly," *J Pharmacol Exp Ther,* vol. 356, no. 2, pp. 267-275, Feb 2016, doi: 10.1124/jpet.115.228130.

[66] C. G. Hadjipanayis, G. Widhalm, and W. Stummer, "What is the Surgical Benefit of Utilizing 5-Aminolevulinic Acid for Fluorescence-Guided Surgery of Malignant Gliomas?," *Neurosurgery,* vol. 77, no. 5, pp. 663-673, Nov 2015, doi: 10.1227/NEU.0000000000000929.

[67] W. Stummer *et al.*, "Fluorescence-guided surgery with 5-aminolevulinic acid for resection of malignant glioma: a randomised controlled multicentre phase III trial," *Lancet Oncol,* vol. 7, no. 5, pp. 392-401, May 2006, doi: 10.1016/S1470-2045(06)70665-9.

[68] J. C. Kennedy, R. H. Pottier, and D. C. Pross, "Photodynamic therapy with endogenous protoporphyrin IX: basic principles and present clinical experience," *J Photochem Photobiol B,* vol. 6, no. 1-2, pp. 143-148, Jun 1990, doi: 10.1016/1011-1344(90)85083-9.

[69] H. Stepp and W. Stummer, "5-ALA in the management of malignant glioma," *Lasers Surg Med,* vol. 50, no. 5, pp. 399-419, Jul 2018, doi: 10.1002/lsm.22933.

[70] H. C. Manning *et al.*, "Molecular imaging of therapeutic response to epidermal growth factor receptor blockade in colorectal cancer," *Clin Cancer Res,* vol. 14, no. 22, pp. 7413-7422, Nov 2008, doi: 10.1158/1078-0432.CCR-08-0239.

[71] L. D. Beilke *et al.*, "Decreased apoptosis during CAR-mediated hepatoprotection against lithocholic acid-induced liver injury in mice," *Toxicol Lett,* vol. 188, no. 1, pp. 38-44, Jul 2009, doi: 10.1016/j.toxlet.2009.03.005.

[72] B. W. Pogue *et al.*, "Imaging targeted-agent binding in vivo with two probes," *J Biomed Opt,* vol. 15, no. 3, p. 030513, May 2010, doi: 10.1117/1.3449109.

[73] T. Nishimura *et al.*, "Photoimmunotherapy targeting biliary-pancreatic cancer with humanized anti-TROP2 antibody," *Cancer Med,* vol. 8, no. 18, pp. 7781-7792, Dec 2019, doi: 10.1002/cam4.2658.

[74] Y. Isobe *et al.*, "Near infrared photoimmunotherapy targeting DLL3 for small cell lung cancer," *EBioMedicine,* vol. 52, p. 102632, Feb 2020, doi: 10.1016/j.ebiom.2020.102632.

[75] T. Nagaya, K. Sato, T. Harada, Y. Nakamura, P. L. Choyke, and H. Kobayashi, "Near Infrared Photoimmunotherapy Targeting EGFR Positive Triple Negative Breast Cancer: Optimizing the Conjugate-Light Regimen," *PLoS One,* vol. 10, no. 8, p. e0136829, Aug 2015, doi: 10.1371/journal.pone.0136829.

[76] T. J. McBride, J. E. Schneider, R. A. Floyd, and L. A. Loeb, "Mutations induced by methylene blue plus light in single-stranded M13mp2," *Proc Natl Acad Sci U S A,* vol. 89, no. 15, pp. 6866-6870, Aug 1992, doi: 10.1073/pnas.89.15.6866.

[77] J. R. Olliver, C. P. Wild, P. Sahay, S. Dexter, and L. J. Hardie, "Chromoendoscopy with methylene blue and associated DNA damage in Barrett's oesophagus," *Lancet,* vol. 362, no. 9381, pp. 373-374, Aug 2003, doi: 10.1016/s0140-6736(03)14026-3.
[78] C. D. Lytle, P. G. Carney, R. P. Felten, H. F. Bushar, and R. C. Straight, "Inactivation and mutagenesis of herpes virus by photodynamic treatment with therapeutic dyes," *Photochem Photobiol,* vol. 50, no. 3, pp. 367-371, Sep 1989, doi: 10.1111/j.1751-1097.1989.tb04171.x.
[79] J. L. Ravanat *et al.*, "Singlet oxygen-mediated damage to cellular DNA determined by the comet assay associated with DNA repair enzymes," *Biol Chem,* vol. 385, no. 1, pp. 17-20, Jan 2004, doi: 10.1515/BC.2004.003.
[80] W. S. Tummers *et al.*, "Regulatory Aspects of Optical Methods and Exogenous Targets for Cancer Detection," *Cancer Res,* vol. 77, no. 9, pp. 2197-2206, May 2017, doi: 10.1158/0008-5472.CAN-16-3217.
[81] S. Kim, M. Fujitsuka, and T. Majima, "Photochemistry of singlet oxygen sensor green," *J Phys Chem B,* vol. 117, no. 45, pp. 13985-13992, Nov 2013, doi: 10.1021/jp406638g.
[82] A. Prasad, M. Sedlarova, and P. Pospisil, "Singlet oxygen imaging using fluorescent probe Singlet Oxygen Sensor Green in photosynthetic organisms," *Sci Rep,* vol. 8, no. 1, p. 13685, Sep 2018, doi: 10.1038/s41598-018-31638-5.
[83] G. Obaid, W. Jin, S. Bano, D. Kessel, and T. Hasan, "Nanolipid Formulations of Benzoporphyrin Derivative: Exploring the Dependence of Nanoconstruct Photophysics and Photochemistry on Their Therapeutic Index in Ovarian Cancer Cells," *Photochem Photobiol,* vol. 95, no. 1, pp. 364-377, Jan 2019, doi: 10.1111/php.13002.
[84] C. Flors *et al.*, "Imaging the production of singlet oxygen in vivo using a new fluorescent sensor, Singlet Oxygen Sensor Green," *J Exp Bot,* vol. 57, no. 8, pp. 1725-1734, Apr 2006, doi: 10.1093/jxb/erj181.
[85] C. T. Inglut *et al.*, "Predictors and Limitations of the Penetration Depth of Photodynamic Effects in the Rodent Brain," *Photochem Photobiol,* vol. 96, no. 2, pp. 301-309, Mar 2020, doi: 10.1111/php.13155.
[86] K. Tanaka *et al.*, "Rational design of fluorescein-based fluorescence probes. Mechanism-based design of a maximum fluorescence probe for singlet oxygen," *J Am Chem Soc,* vol. 123, no. 11, pp. 2530-2536, Mar 2001, doi: 10.1021/ja0035708.
[87] R. Arora *et al.*, "Preservation of the metabolic rate of oxygen in preterm infants during indomethacin therapy for closure of the ductus arteriosus," *Pediatr Res,* vol. 73, no. 6, pp. 713-718, Jun 2013, doi: 10.1038/pr.2013.53.
[88] "IC-GREEN® (indocyanine green for injection USP) For Intravenous Injection." (accessed 2020).
[89] B. Zhu and E. M. Sevick-Muraca, "A review of performance of near-infrared fluorescence imaging devices used in clinical studies," *Br J Radiol,* vol. 88, no. 1045, p. 20140547, Jan 2015, doi: 10.1259/bjr.20140547.
[90] C. Peter, D. Hongwan, A. Kupfer, and B. H. Lauterburg, "Pharmacokinetics and organ distribution of intravenous and oral methylene blue," *Eur J Clin*

Pharmacol, vol. 56, no. 3, pp. 247-250, Jun 2000, doi: 10.1007/s002280000124.

[91] A. Matsui *et al.*, "Real-time, near-infrared, fluorescence-guided identification of the ureters using methylene blue," *Surgery,* vol. 148, no. 1, pp. 78-86, Jul 2010, doi: 10.1016/j.surg.2009.12.003.

[92] R. W. Gao *et al.*, "Safety of panitumumab-IRDye800CW and cetuximab-IRDye800CW for fluorescence-guided surgical navigation in head and neck cancers," *Theranostics,* vol. 8, no. 9, pp. 2488-2495, Mar 2018, doi: 10.7150/thno.24487.

[93] S. E. Miller *et al.*, "First-in-human intraoperative near-infrared fluorescence imaging of glioblastoma using cetuximab-IRDye800," *J Neurooncol,* vol. 139, no. 1, pp. 135-143, Aug 2018, doi: 10.1007/s11060-018-2854-0.

[94] K. Ito, M. Mitsunaga, T. Nishimura, H. Kobayashi, and H. Tajiri, "Combination photoimmunotherapy with monoclonal antibodies recognizing different epitopes of human epidermal growth factor receptor 2: an assessment of phototherapeutic effect based on fluorescence molecular imaging," *Oncotarget,* vol. 7, no. 12, pp. 14143-14152, Mar 2016, doi: 10.18632/oncotarget.7490.

[95] D. S. AV, H. Lin, E. R. Henderson, K. S. Samkoe, and B. W. Pogue, "Review of fluorescence guided surgery systems: identification of key performance capabilities beyond indocyanine green imaging," *J Biomed Opt,* vol. 21, no. 8, p. 80901, Aug 2016, doi: 10.1117/1.JBO.21.8.080901.

[96] Y. Tang, J. Carns, A. D. Polydorides, S. Anandasabapathy, and R. R. Richards-Kortum, "In vivo white light and contrast-enhanced vital-dye fluorescence imaging of Barrett's-related neoplasia in a single-endoscopic insertion," *J Biomed Opt,* vol. 21, no. 8, p. 86004, Aug 2016, doi: 10.1117/1.JBO.21.8.086004.

[97] V. Perez-Laguna *et al.*, "Antimicrobial photodynamic activity of Rose Bengal, alone or in combination with Gentamicin, against planktonic and biofilm Staphylococcus aureus," *Photodiagnosis Photodyn Ther,* vol. 21, pp. 211-216, Mar 2018, doi: 10.1016/j.pdpdt.2017.11.012.

[98] N. Unno *et al.*, "Preliminary experience with a novel fluorescence lymphography using indocyanine green in patients with secondary lymphedema," *J Vasc Surg,* vol. 45, no. 5, pp. 1016-1021, May 2007, doi: 10.1016/j.jvs.2007.01.023.

[99] M. Takeuchi *et al.*, "Lymphatic mapping with fluorescence navigation using indocyanine green and axillary surgery in patients with primary breast cancer," *Breast J,* vol. 18, no. 6, pp. 535-541, Nov 2012, doi: 10.1111/tbj.12004.

[100] T. Imai, K. Takahashi, F. Goto, and Y. Morishita, "Measurement of blood concentration of indocyanine green by pulse dye densitometry--comparison with the conventional spectrophotometric method," *J Clin Monit Comput,* vol. 14, no. 7-8, pp. 477-484, Dec 1998, doi: 10.1023/a:1009948128543.

[101] N. Tagaya *et al.*, "Intraoperative identification of sentinel lymph nodes by near-infrared fluorescence imaging in patients with breast cancer," *Am J Surg,* vol. 195, no. 6, pp. 850-853, Jun 2008, doi: 10.1016/j.amjsurg.2007.02.032.

[102] A. F. D. Di Stefano *et al.*, "Methylene blue MMX(R) tablets for chromoendoscopy. Bioavailability, colon staining and safety in healthy volunteers undergoing a full colonoscopy," *Contemp Clin Trials,* vol. 71, pp. 96-102, Aug 2018, doi: 10.1016/j.cct.2018.06.001.
[103] C. Tanielian and G. Heinrich, "Effect of Aggregation on the Hematoporphyrin-Sensitized Production of Singlet Molecular-Oxygen," *Photochemistry and Photobiology,* vol. 61, no. 2, pp. 131-135, Feb 1995, doi: DOI 10.1111/j.1751-1097.1995.tb03950.x.
[104] S. Mathai, T. A. Smith, and K. P. Ghiggino, "Singlet oxygen quantum yields of potential porphyrin-based photosensitisers for photodynamic therapy," *Photochem Photobiol Sci,* vol. 6, no. 9, pp. 995-1002, Sep 2007, doi: 10.1039/b705853e.
[105] F. Wilkinson, W. P. Helman, and A. B. Ross, "Quantum Yields for the Photosensitized Formation of the Lowest Electronically Excited Singlet-State of Molecular-Oxygen in Solution," *J Phys Chem Ref Data,* vol. 22, no. 1, pp. 113-262, Jan 1993, doi: Doi 10.1063/1.555934.
[106] S. Kishimoto *et al.*, "Evaluation of oxygen dependence on in vitro and in vivo cytotoxicity of photoimmunotherapy using IR-700-antibody conjugates," *Free Radic Biol Med,* vol. 85, pp. 24-32, Aug 2015, doi: 10.1016/j.freeradbiomed.2015.03.038.
[107] R. Kiesslich *et al.*, "Methylene blue-aided chromoendoscopy for the detection of intraepithelial neoplasia and colon cancer in ulcerative colitis," *Gastroenterology,* vol. 124, no. 4, pp. 880-888, Apr 2003, doi: 10.1053/gast.2003.50146.
[108] B. J. Harrison and F. Triponez, "Intraoperative adjuncts in surgery for primary hyperparathyroidism," *Langenbecks Arch Surg,* vol. 394, no. 5, pp. 799-809, Sep 2009, doi: 10.1007/s00423-009-0532-6.
[109] J. H. Winer, H. S. Choi, S. L. Gibbs-Strauss, Y. Ashitate, Y. L. Colson, and J. V. Frangioni, "Intraoperative localization of insulinoma and normal pancreas using invisible near-infrared fluorescent light," *Ann Surg Oncol,* vol. 17, no. 4, pp. 1094-1100, Apr 2010, doi: 10.1245/s10434-009-0868-8.
[110] J. Kluk, R. Charles-Holmes, and D. Markham, "Acute phototoxicity induced by methylene blue-assisted parathyroidectomy: an unreported risk of a common procedure," *Br J Dermatol,* vol. 166, no. 4, pp. 907-908, Apr 2012, doi: 10.1111/j.1365-2133.2011.10703.x.
[111] M. R. Sills and W. H. Zinkham, "Methylene blue-induced Heinz body hemolytic anemia," *Arch Pediatr Adolesc Med,* vol. 148, no. 3, pp. 306-310, Mar 1994, doi: 10.1001/archpedi.1994.02170030076017.
[112] R. Porat, S. Gilbert, and D. Magilner, "Methylene blue-induced phototoxicity: an unrecognized complication," *Pediatrics,* vol. 97, no. 5, pp. 717-721, May 1996.
[113] J. Davies, D. Burke, J. R. Olliver, L. J. Hardie, C. P. Wild, and M. N. Routledge, "Methylene blue but not indigo carmine causes DNA damage to colonocytes in vitro and in vivo at concentrations used in clinical chromoendoscopy," *Gut,* vol. 56, no. 1, pp. 155-156, Jan 2007, doi: 10.1136/gut.2006.107300.

[114] C. M. Klais, M. D. Ober, and L. A. Yannuzzi, "Indocyanine Green Angiography: General Aspects and Interpretation," in *Retinal Angiography and Optical Coherence Tomography*: Springer New York, 2009, ch. Chapter 3, pp. 43-59.
[115] S. Balamurugan, A. Agrawal, Y. Kato, and H. Sano, "Intra operative indocyanine green video-angiography in cerebrovascular surgery: An overview with review of literature," *Asian J Neurosurg,* vol. 6, no. 2, pp. 88-93, Jul 2011, doi: 10.4103/1793-5482.92168.
[116] J. Y. K. Lee *et al.*, "Intraoperative Near-Infrared Optical Contrast Can Localize Brain Metastases," *World Neurosurg,* vol. 106, pp. 120-130, Oct 2017, doi: 10.1016/j.wneu.2017.06.128.
[117] Q. Y. Chen *et al.*, "Safety and Efficacy of Indocyanine Green Tracer-Guided Lymph Node Dissection During Laparoscopic Radical Gastrectomy in Patients With Gastric Cancer: A Randomized Clinical Trial," *JAMA Surg,* vol. 155, no. 4, pp. 300-311, Apr 2020, doi: 10.1001/jamasurg.2019.6033.
[118] E. Engel *et al.*, "Light-induced decomposition of indocyanine green," *Invest Ophthalmol Vis Sci,* vol. 49, no. 5, pp. 1777-1783, May 2008, doi: 10.1167/iovs.07-0911.
[119] A. Dimofte, J. C. Finlay, and T. C. Zhu, "A method for determination of the absorption and scattering properties interstitially in turbid media," *Phys Med Biol,* vol. 50, no. 10, pp. 2291-2311, May 2005, doi: 10.1088/0031-9155/50/10/008.
[120] S. L. Jacques, "How tissue optics affect dosimetry of photodynamic therapy," *J Biomed Opt,* vol. 15, no. 5, p. 051608, Sep 2010, doi: 10.1117/1.3494561.
[121] D. Bechet, S. R. Mordon, F. Guillemin, and M. A. Barberi-Heyob, "Photodynamic therapy of malignant brain tumours: a complementary approach to conventional therapies," *Cancer Treat Rev,* vol. 40, no. 2, pp. 229-241, Mar 2014, doi: 10.1016/j.ctrv.2012.07.004.
[122] N. Lakomkin and C. G. Hadjipanayis, "Fluorescence-guided surgery for high-grade gliomas," *Journal of surgical oncology,* vol. 118, no. 2, pp. 356-361, Aug 2018, doi: 10.1002/jso.25154.
[123] C. G. Hadjipanayis and W. Stummer, "5-ALA and FDA approval for glioma surgery," *J Neurooncol,* vol. 141, no. 3, pp. 479-486, Feb 2019, doi: 10.1007/s11060-019-03098-y.
[124] Q. T. Ostrom *et al.*, "CBTRUS Statistical Report: Primary brain and other central nervous system tumors diagnosed in the United States in 2010-2014," *Neuro-oncology,* vol. 19, no. suppl_5, pp. v1-v88, Nov 2017, doi: 10.1093/neuonc/nox158.
[125] H. Kostron, A. Obwegeser, and R. Jakober, "Photodynamic therapy in neurosurgery: a review," *J Photochem Photobiol B,* vol. 36, no. 2, pp. 157-168, Nov 1996, doi: 10.1016/s1011-1344(96)07364-2.
[126] M. S. Eljamel, C. Goodman, and H. Moseley, "ALA and Photofrin fluorescence-guided resection and repetitive PDT in glioblastoma multiforme: a single centre Phase III randomised controlled trial," *Lasers Med Sci,* vol. 23, no. 4, pp. 361-367, Oct 2008, doi: 10.1007/s10103-007-0494-2.

[127] C. Dupont *et al.*, "INtraoperative photoDYnamic Therapy for GliOblastomas (INDYGO): Study Protocol for a Phase I Clinical Trial," *Neurosurgery,* vol. 84, no. 6, pp. E414-E419, Jun 2019, doi: 10.1093/neuros/nyy324.
[128] J. L. Sandell and T. C. Zhu, "A review of in-vivo optical properties of human tissues and its impact on PDT," *J Biophotonics,* vol. 4, no. 11-12, pp. 773-787, Nov 2011, doi: 10.1002/jbio.201100062.
[129] S. H. Yun and S. J. J. Kwok, "Light in diagnosis, therapy and surgery," *Nat Biomed Eng,* Review Article vol. 1, p. 0008, Jan 2017, doi: 10.1038/s41551-016-0008.
[130] P. Wang and T. Li, "Which wavelength is optimal for transcranial low-level laser stimulation?," *J Biophotonics,* vol. 12, no. 2, p. e201800173, Feb 2019, doi: 10.1002/jbio.201800173.
[131] T. Li, C. Xue, P. B. Wang, Y. Li, and L. H. Wu, "Photon penetration depth in human brain for light stimulation and treatment: A realistic Monte Carlo simulation study," *J Innov Opt Heal Sci,* vol. 10, no. 5, p. 1743002, Sep 2017, doi: Artn 1743002
10.1112/S1793515817130027.
[132] F. B. Haeussinger, S. Heinzel, T. Hahn, M. Schecklmann, A. C. Ehlis, and A. J. Fallgatter, "Simulation of near-infrared light absorption considering individual head and prefrontal cortex anatomy: implications for optical neuroimaging," *PLoS One,* vol. 6, no. 10, p. e26377, Oct 2011, doi: 10.1371/journal.pone.0026377.
[133] A. Pitzschke *et al.*, "Red and NIR light dosimetry in the human deep brain," *Phys Med Biol,* vol. 60, no. 7, pp. 2921-2937, Apr 2015, doi: 10.1088/0031-9155/60/7/2921.
[134] C. E. Tedford, S. DeLapp, S. Jacques, and J. Anders, "Quantitative analysis of transcranial and intraparenchymal light penetration in human cadaver brain tissue," *Lasers Surg Med,* vol. 47, no. 4, pp. 312-322, Apr 2015, doi: 10.1002/lsm.22343.
[135] T. A. Henderson and L. D. Morries, "Near-infrared photonic energy penetration: can infrared phototherapy effectively reach the human brain?," *Neuropsychiatric disease and treatment,* vol. 11, pp. 2191-2208, Sep 2015, doi: 10.2147/NDT.S78182.
[136] M. R. Hamblin, "Shining light on the head: Photobiomodulation for brain disorders," *BBA clinical,* vol. 6, pp. 113-124, Dec 2016, doi: 10.1016/j.bbacli.2016.09.002.
[137] C. Perria *et al.*, "Fast attempts at the photodynamic treatment of human gliomas," *Journal of neurosurgical sciences,* vol. 24, no. 3-4, pp. 119-129, Jul 1980.
[138] M.-K. Cheng, J. McKean, D. Boisvert, J. Tulip, and W. B. Mielke, "Effects of Photoradiation Therapy on Normal Rat Brian," *Neurosurgery,* vol. 15, no. 6, pp. 804-810, Jun 1984, doi: 10.1097/00006123-198412000-00006.
[139] B. C. Wilson, P. J. Muller, and J. C. Yanch, "Instrumentation and light dosimetry for intra-operative photodynamic therapy (PDT) of malignant brain tumours," *Phys Med Biol,* vol. 31, no. 2, pp. 125-133, Feb 1986, doi: 10.1088/0031-9155/31/2/002.

[140] B. Olzowy, C. S. Hundt, S. Stocker, K. Bise, H. J. Reulen, and W. Stummer, "Photoirradiation therapy of experimental malignant glioma with 5-aminolevulinic acid," *J Neurosurg,* vol. 97, no. 4, pp. 970-976, Oct 2002, doi: 10.3171/jns.2002.97.4.0970.
[141] N. M. Bressler, "Photodynamic therapy of subfoveal choroidal neovascularization in age-related macular degeneration with verteporfin: one-year results of 2 randomized clinical trials--TAP report. Treatment of age-related macular degeneration with photodynamic therapy (TAP) Study Group," *Archives of ophthalmology (Chicago, Ill. : 1960),* vol. 117, no. 10, pp. 1329-1345, Oct 1999, doi: 10.1001/archopht.117.10.1329.
[142] U. Schmidt-Erfurth, T. Hasan, E. Gragoudas, N. Michaud, T. J. Flotte, and R. Birngruber, "Vascular targeting in photodynamic occlusion of subretinal vessels," *Ophthalmology,* vol. 101, no. 12, pp. 1953-1961, Dec 1994, doi: 10.1016/s0161-6420(13)31079-3.
[143] M. H. Schmidt *et al.*, "Evaluation of photodynamic therapy near functional brain tissue in patients with recurrent brain tumors," (in eng), *J Neurooncol,* vol. 67, no. 1-2, pp. 201-207, Mar 2004, doi: 10.1023/b:neon.0000021804.50002.85.
[144] A. L. Tessaro *et al.*, "Stability of benzoporphyrin photosensitizers in water/ethanol mixtures: pK(a) determination and self-aggregation processes," *J Phys Org Chem,* vol. 24, no. 2, pp. 155-161, Feb 2011, doi: 10.1002/poc.1721.
[145] L. M. Scolaro, M. Castriciano, A. Romeo, S. Patane, E. Cefali, and M. Allegrini, "Aggregation behavior of protoporphyrin IX in aqueous solutions: Clear evidence of vesicle formation," *Journal of Physical Chemistry B,* vol. 106, no. 10, pp. 2453-2459, Mar 2002, doi: 10.1021/jp013155h.
[146] L. Yan *et al.*, "Dextran-Benzoporphyrin Derivative (BPD) Coated Superparamagnetic Iron Oxide Nanoparticle (SPION) Micelles for T2-Weighted Magnetic Resonance Imaging and Photodynamic Therapy," *Bioconjug Chem,* vol. 30, no. 11, pp. 2974-2981, Nov 2019, doi: 10.1021/acs.bioconjchem.9b00676.
[147] Y. Baglo, B. J. Liang, R. W. Robey, S. V. Ambudkar, M. M. Gottesman, and H. C. Huang, "Porphyrin-lipid assemblies and nanovesicles overcome ABC transporter-mediated photodynamic therapy resistance in cancer cells," *Cancer Lett,* vol. 457, pp. 110-118, Aug 2019, doi: 10.1016/j.canlet.2019.04.037.
[148] M. Pigula *et al.*, "Size-dependent Tumor Response to Photodynamic Therapy and Irinotecan Monotherapies Revealed by Longitudinal Ultrasound Monitoring in an Orthotopic Pancreatic Cancer Model," *Photochem Photobiol,* vol. 95, no. 1, pp. 378-386, Jan 2019, doi: 10.1111/php.13016.
[149] H. C. Huang *et al.*, "Photodynamic Priming Mitigates Chemotherapeutic Selection Pressures and Improves Drug Delivery," *Cancer Res,* vol. 78, no. 2, pp. 558-571, Jan 2018, doi: 10.1158/0008-5472.CAN-17-1700.
[150] H. C. Huang *et al.*, "Photodynamic Therapy Synergizes with Irinotecan to Overcome Compensatory Mechanisms and Improve Treatment Outcomes in

Pancreatic Cancer," *Cancer Res,* vol. 76, no. 5, pp. 1066-1077, Mar 2016, doi: 10.1158/0008-5472.CAN-15-0391.
[151] H. C. Huang *et al.*, "Mechanism-informed Repurposing of Minocycline Overcomes Resistance to Topoisomerase Inhibition for Peritoneal Carcinomatosis," *Molecular cancer therapeutics,* vol. 17, no. 2, pp. 508-520, Feb 2018, doi: 10.1158/1535-7163.MCT-17-0568.
[152] C. A. Schneider, W. S. Rasband, and K. W. Eliceiri, "NIH Image to ImageJ: 25 years of image analysis," *Nature methods,* vol. 9, no. 7, pp. 671-675, Jul 2012, doi: 10.1038/nmeth.2089.
[153] J. P. Celli *et al.*, "Imaging and photodynamic therapy: mechanisms, monitoring, and optimization," *Chem Rev,* vol. 110, no. 5, pp. 2795-2838, May 2010, doi: 10.1021/cr900300p.
[154] B. M. Aveline, T. Hasan, and R. W. Redmond, "The effects of aggregation, protein binding and cellular incorporation on the photophysical properties of benzoporphyrin derivative monoacid ring A (BPDMA)," *J Photochem Photobiol B,* vol. 30, no. 2-3, pp. 161-169, Oct 1995, doi: 10.1016/1011-1344(95)07174-z.
[155] R. W. Redmond and J. N. Gamlin, "A compilation of singlet oxygen yields from biologically relevant molecules," *Photochem Photobiol,* vol. 70, no. 4, pp. 391-475, Oct 1999.
[156] B. Aveline, T. Hasan, and R. W. Redmond, "Photophysical and photosensitizing properties of benzoporphyrin derivative monoacid ring A (BPD-MA)," *Photochem Photobiol,* vol. 59, no. 3, pp. 328-335, Mar 1994, doi: 10.1111/j.1751-1097.1994.tb05042.x.
[157] G. I. Lozovaya, Z. Masinovsky, and A. A. Sivash, "Protoporphyrin-IX as a Possible Ancient Photosensitizer - Spectral and Photochemical Studies," *Origins Life Evol B,* vol. 20, no. 3-4, pp. 321-330, May 1990, doi: 10.1007/Bf01808114.
[158] A. P. Castano, P. Mroz, and M. R. Hamblin, "Photodynamic therapy and anti-tumour immunity," *Nat Rev Cancer,* 10.1038/nrc1894 vol. 6, no. 7, pp. 535-545, Jul 2006, doi: 10.1038/nrc1894.
[159] D. E. Dolmans, D. Fukumura, and R. K. Jain, "Photodynamic therapy for cancer," *Nat Rev Cancer,* vol. 3, no. 5, pp. 380-387, May 2003, doi: 10.1038/nrc1071.
[160] M. T. Jarvi, M. S. Patterson, and B. C. Wilson, "Insights into photodynamic therapy dosimetry: simultaneous singlet oxygen luminescence and photosensitizer photobleaching measurements," *Biophysical journal,* vol. 102, no. 63, pp. 661-671, Feb 2012, doi: 10.1016/j.bpj.2011.12.043.
[161] M. M. Kim, J. C. Finlay, and T. C. Zhu, "Macroscopic singlet oxygen model incorporating photobleaching as an input parameter," *Proceedings of SPIE--the International Society for Optical Engineering,* vol. 9308, p. 93080V, Mar 2015, doi: 10.1117/12.2079046.
[162] J. C. Finlay, S. Mitra, and T. H. Foster, "In vivo mTHPC photobleaching in normal rat skin exhibits unique irradiance-dependent features," *Photochem Photobiol,* vol. 75, no. 3, pp. 282-288, Mar 2002, doi: 10.1562/0031-8655(2002)075<0282:ivmpin>2.0.co;2.

[163] J. C. Finlay, S. Mitra, M. S. Patterson, and T. H. Foster, "Photobleaching kinetics of Photofrin in vivo and in multicell tumour spheroids indicate two simultaneous bleaching mechanisms," *Phys Med Biol,* vol. 49, no. 21, pp. 4837-4860, Nov 2004, doi: 10.1088/0031-9155/49/21/001.
[164] R. Bonnett and G. Martínez, "Photobleaching of sensitisers used in photodynamic therapy," *Tetrahedron,* vol. 57, no. 47, pp. 9513-9547, Nov 2001, doi: 10.1016/S0040-4020(01)00952-8.
[165] M. O. Dereski, M. Chopp, J. H. Garcia, and F. W. Hetzel, "Depth measurements and histopathological characterization of photodynamic therapy generated normal brain necrosis as a function of incident optical energy dose," *Photochem Photobiol,* vol. 54, no. 1, pp. 109-112, Jul 1991, doi: 10.1111/j.1751-1097.1991.tb01992.x.
[166] S. Ikuta *et al.*, "Penetration depth of the 664-nm semiconductor laser light with talaporfin sodium into human brain tissue with glioma," *Photodiagnosis and Photodynamic Therapy,* vol. 12, no. 3, p. 349, Sep 2015, doi: 10.1016/j.pdpdt.2015.07.098.
[167] S. L. Jacques, *Simple optical theory for light dosimetry during PDT (Invited Paper)* (OE/LASE '92). SPIE, 1992.
[168] S. L. Jacques, "Optical properties of biological tissues: a review," *Phys Med Biol,* vol. 58, no. 11, pp. R37-61, Jun 2013, doi: 10.1088/0031-9155/58/11/R37.
[169] J. Binding, J. Ben Arous, J. F. Leger, S. Gigan, C. Boccara, and L. Bourdieu, "Brain refractive index measured in vivo with high-NA defocus-corrected full-field OCT and consequences for two-photon microscopy," *Opt Express,* vol. 19, no. 6, pp. 4833-4847, Mar 2011, doi: 10.1364/OE.19.004833.
[170] S. L. Jacques, "Light distributions from point, line and plane sources for photochemical reactions and fluorescence in turbid biological tissues," *Photochem Photobiol,* vol. 67, no. 1, pp. 23-32, Jan 1998.
[171] Y. H. Ong and T. C. Zhu, "Analytic function for predicting light fluence rate of circular fields on a semi-infinite turbid medium," *Opt Express,* vol. 24, no. 23, pp. 26261-26281, Nov 2016, doi: 10.1364/OE.24.026261.
[172] F. Bevilacqua, D. Piguet, P. Marquet, J. D. Gross, B. J. Tromberg, and C. Depeursinge, "In vivo local determination of tissue optical properties: applications to human brain," *Applied optics,* vol. 38, no. 22, pp. 4939-4950, Aug 1999, doi: 10.1364/ao.38.004939.
[173] G. Yona, N. Meitav, I. Kahn, and S. Shoham, "Realistic Numerical and Analytical Modeling of Light Scattering in Brain Tissue for Optogenetic Applications(1,2,3)," *eNeuro,* vol. 3, no. 1, Jan 2016, doi: 10.1523/ENEURO.0059-15.2015.
[174] L. B. Josefsen and R. W. Boyle, "Photodynamic therapy and the development of metal-based photosensitisers," *Metal-based drugs,* vol. 2008, p. 276109, Sep 2008, doi: 10.1155/2008/276109.
[175] J. L. Schnapf, T. W. Kraft, and D. A. Baylor, "Spectral sensitivity of human cone photoreceptors," *Nature,* vol. 325, no. 6103, pp. 439-441, Jan 1987, doi: 10.1038/325439a0.

[176] B. A. Hartl, H. Hirschberg, L. Marcu, and S. R. Cherry, "Activating Photodynamic Therapy in vitro with Cerenkov Radiation Generated from Yttrium-90," *Journal of Environmental Pathology, Toxicology and Oncology,* vol. 35, no. 2, pp. 185-192, Mar 2016, doi: 10.1615/jenvironpatholtoxicoloncol.2016016903.
[177] G. D. Wang *et al.*, "X-Ray Induced Photodynamic Therapy: A Combination of Radiotherapy and Photodynamic Therapy," *Theranostics,* vol. 6, no. 13, pp. 2295-2305, Oct 2016, doi: 10.7150/thno.16141.
[178] H. Qiu, M. Tan, T. Ohulchanskyy, J. Lovell, and G. Chen, "Recent Progress in Upconversion Photodynamic Therapy," *Nanomaterials,* vol. 8, no. 5, p. 344, 2018, doi: 10.3390/nano8050344.
[179] K. E. Wallner, J. H. Galicich, G. Krol, E. Arbit, and M. G. Malkin, "Patterns of failure following treatment for glioblastoma multiforme and anaplastic astrocytoma," *International journal of radiation oncology, biology, physics,* vol. 16, no. 6, pp. 1405-1409, Jun 1989, doi: 10.1016/0360-3016(89)90941-3.
[180] J. Sherriff *et al.*, "Patterns of relapse in glioblastoma multiforme following concomitant chemoradiotherapy with temozolomide," *Br J Radiol,* vol. 86, no. 1022, p. 20120414, Feb 2013, doi: 10.1259/bjr.20120414.
[181] D. L. Silbergeld and M. R. Chicoine, "Isolation and characterization of human malignant glioma cells from histologically normal brain," *J Neurosurg,* vol. 86, no. 3, pp. 525-531, Mar 1997, doi: 10.3171/jns.1997.86.3.0525.
[182] D. E. Chandler and R. W. Roberson, *Bioimaging : current concepts in light and electron microscopy*. 2009, p. 440.
[183] H. Lehmann, *Lumineszenzmikroskop, seine Grundlagen und seine Anwendungen*. 1913.
[184] A. K. Sinha *et al.*, "Methotrexate used in combination with aminolaevulinic acid for photodynamic killing of prostate cancer cells," *Br J Cancer,* vol. 95, no. 4, pp. 485-495, Aug 2006, doi: 10.1038/sj.bjc.6603273.
[185] L. Teng *et al.*, "Silencing of ferrochelatase enhances 5-aminolevulinic acid-based fluorescence and photodynamic therapy efficacy," *Br J Cancer,* vol. 104, no. 5, pp. 798-807, Mar 2011, doi: 10.1038/bjc.2011.12.
[186] Y. Hagiya *et al.*, "Expression levels of PEPT1 and ABCG2 play key roles in 5-aminolevulinic acid (ALA)-induced tumor-specific protoporphyrin IX (PpIX) accumulation in bladder cancer," *Photodiagnosis Photodyn Ther,* vol. 10, no. 3, pp. 288-295, Sep 2013, doi: 10.1016/j.pdpdt.2013.02.001.
[187] W. Stummer, A. Novotny, H. Stepp, C. Goetz, K. Bise, and H. J. Reulen, "Fluorescence-guided resection of glioblastoma multiforme by using 5-aminolevulinic acid-induced porphyrins: a prospective study in 52 consecutive patients," *J Neurosurg,* vol. 93, no. 6, pp. 1003-1013, Dec 2000, doi: 10.3171/jns.2000.93.6.1003.
[188] S. Gandhi *et al.*, "Survival Outcomes Among Patients With High-Grade Glioma Treated With 5-Aminolevulinic Acid-Guided Surgery: A Systematic Review and Meta-Analysis," *Front Oncol,* vol. 9, p. 620, Jul 2019, doi: 10.3389/fonc.2019.00620.

[189] A. J. Sorrin *et al.*, "Photodynamic Therapy and the Biophysics of the Tumor Microenvironment," *Photochem Photobiol,* vol. 96, no. 2, pp. 232-259, Mar 2020, doi: 10.1111/php.13209.
[190] H. B. Ris *et al.*, "Effect of drug-light interval on photodynamic therapy with meta-tetrahydroxyphenylchlorin in malignant mesothelioma," *Int J Cancer,* vol. 53, no. 1, pp. 141-146, Jan 1993, doi: 10.1002/ijc.2910530126.
[191] L. B. Li and R. C. Luo, "Effect of drug-light interval on the mode of action of Photofrin photodynamic therapy in a mouse tumor model," *Lasers Med Sci,* vol. 24, no. 4, pp. 597-603, Jul 2009, doi: 10.1007/s10103-008-0620-9.
[192] C. Sheng, B. W. Pogue, E. Wang, J. E. Hutchins, and P. J. Hoopes, "Assessment of Photosensitizer Dosimetry and Tissue Damage Assay for Photodynamic Therapy in Advanced-stage Tumors," *Photochemistry and Photobiology,* vol. 79, no. 6, pp. 520-526, May 2007, doi: 10.1111/j.1751-1097.2004.tb01270.x.
[193] L. B. Rocha, L. C. Gomes-da-Silva, J. M. Dabrowski, and L. G. Arnaut, "Elimination of primary tumours and control of metastasis with rationally designed bacteriochlorin photodynamic therapy regimens," *Eur J Cancer,* vol. 51, no. 13, pp. 1822-1830, Sep 2015, doi: 10.1016/j.ejca.2015.06.002.
[194] C. T. Inglut *et al.*, "Systematic Evaluation of Light-Activatable Biohybrids for Anti-Glioma Photodynamic Therapy," *J Clin Med,* vol. 8, no. 9, p. 1269, Aug 2019, doi: 10.3390/jcm8091269.
[195] M. Venturini, R. Sala, S. Gonzalez, and P. G. Calzavara-Pinton, "Reflectance confocal microscopy allows in vivo real-time noninvasive assessment of the outcome of methyl aminolaevulinate photodynamic therapy of basal cell carcinoma," *Br J Dermatol,* vol. 168, no. 1, pp. 99-105, Jan 2013, doi: 10.1111/bjd.12052.
[196] C. Olsovsky, R. Shelton, O. Carrasco-Zevallos, B. E. Applegate, and K. C. Maitland, "Chromatic confocal microscopy for multi-depth imaging of epithelial tissue," *Biomed Opt Express,* vol. 4, no. 5, pp. 732-740, May 2013, doi: 10.1364/BOE.4.000732.
[197] V. Ntziachristos, "Going deeper than microscopy: the optical imaging frontier in biology," *Nature methods,* vol. 7, no. 8, pp. 603-614, Aug 2010, doi: 10.1038/nmeth.1483.
[198] D. J. Cuccia, F. Bevilacqua, A. J. Durkin, F. R. Ayers, and B. J. Tromberg, "Quantitation and mapping of tissue optical properties using modulated imaging," *J Biomed Opt,* vol. 14, no. 2, p. 024012, Mar 2009, doi: 10.1117/1.3088140.
[199] S. D. Konecky, A. Mazhar, D. Cuccia, A. J. Durkin, J. C. Schotland, and B. J. Tromberg, "Quantitative optical tomography of sub-surface heterogeneities using spatially modulated structured light," *Opt Express,* vol. 17, no. 17, pp. 14780-14790, Aug 2009, doi: 10.1364/oe.17.014780.
[200] A. M. Laughney *et al.*, "System analysis of spatial frequency domain imaging for quantitative mapping of surgically resected breast tissues," *J Biomed Opt,* vol. 18, no. 3, p. 036012, Mar 2013, doi: 10.1117/1.JBO.18.3.036012.
[201] M. Sibai, D. J. Wirth, F. Leblond, D. W. Roberts, K. D. Paulsen, and B. C. Wilson, "Quantitative subsurface spatial frequency-domain fluorescence

imaging for enhanced glioma resection," *J Biophotonics,* vol. 12, no. 5, p. e201800271, May 2019, doi: 10.1002/jbio.201800271.
[202] D. J. Wirth, M. Sibai, B. C. Wilson, D. W. Roberts, and K. Paulsen, "First experience with spatial frequency domain imaging and red-light excitation of protoporphyrin IX fluorescence during tumor resection," *Biomed Opt Express,* vol. 11, no. 8, pp. 4306-4315, Aug 2020, doi: 10.1364/BOE.397507.
[203] E. M. Hillman, D. A. Boas, A. M. Dale, and A. K. Dunn, "Laminar optical tomography: demonstration of millimeter-scale depth-resolved imaging in turbid media," *Opt Lett,* vol. 29, no. 14, pp. 1650-1652, Jul 2004, doi: 10.1364/ol.29.001650.
[204] E. M. Hillman, O. Bernus, E. Pease, M. B. Bouchard, and A. Pertsov, "Depth-resolved optical imaging of transmural electrical propagation in perfused heart," *Opt Express,* vol. 15, no. 26, pp. 17827-17841, Dec 2007, doi: 10.1364/oe.15.017827.
[205] Y. Chen *et al.*, "Integrated Optical Coherence Tomography (OCT) and Fluorescence Laminar Optical Tomography (FLOT)," *IEEE Journal of Selected Topics in Quantum Electronics,* vol. 16, no. 4, pp. 755-766, Jul 2010, doi: 10.1109/jstqe.2009.2037723.
[206] C.-W. Chen and Y. U. Chen, "Optimization of Design Parameters for Fluorescence Laminar Optical Tomography," (in English), *J Innov Opt Heal Sci,* vol. 04, no. 03, pp. 309-323, Jul 2011, doi: 10.1142/s1793545811001435.
[207] X. Intes, J. Ripoll, Y. Chen, S. Nioka, A. G. Yodh, and B. Chance, "In vivo continuous-wave optical breast imaging enhanced with Indocyanine Green," *Med Phys,* vol. 30, no. 6, pp. 1039-1047, Jun 2003, doi: 10.1118/1.1573791.
[208] L. Wang and S. L. Jacques, "Use of a laser beam with an oblique angle of incidence to measure the reduced scattering coefficient of a turbid medium," *Applied optics,* vol. 34, no. 13, pp. 2362-2366, May 1995, doi: 10.1364/AO.34.002362.
[209] U. Kanniyappan *et al.*, "Performance test methods for near-infrared fluorescence imaging," *Med Phys,* vol. 47, no. 8, pp. 3389-3401, Aug 2020, doi: 10.1002/mp.14189.
[210] T. C. Zhu, M. M. Kim, X. Liang, J. C. Finlay, and T. M. Busch, "In-vivo singlet oxygen threshold doses for PDT," *Photonics Lasers Med,* vol. 4, no. 1, pp. 59-71, Feb 2015, doi: 10.1515/plm-2014-0037.
[211] H. Niu, Z. J. Lin, F. Tian, S. Dhamne, and H. Liu, "Comprehensive investigation of three-dimensional diffuse optical tomography with depth compensation algorithm," *J Biomed Opt,* vol. 15, no. 4, p. 046005, Jul 2010, doi: 10.1117/1.3462986.
[212] W. M. Star, "Light dosimetry in vivo," *Phys Med Biol,* vol. 42, no. 5, pp. 763-787, May 1997, doi: 10.1088/0031-9155/42/5/003.
[213] M. Johns, C. Giller, D. German, and H. Liu, "Determination of reduced scattering coefficient of biological tissue from a needle-like probe," *Opt Express,* vol. 13, no. 13, pp. 4828-4842, Jun 2005, doi: 10.1364/opex.13.004828.

[214] R. Yao, X. Intes, and Q. Fang, "Generalized mesh-based Monte Carlo for wide-field illumination and detection via mesh retessellation," *Biomed Opt Express,* vol. 7, no. 1, pp. 171-184, Jan 2016, doi: 10.1364/BOE.7.000171.
[215] M. Sibai *et al.*, "Preclinical evaluation of spatial frequency domain-enabled wide-field quantitative imaging for enhanced glioma resection," *J Biomed Opt,* vol. 22, no. 7, p. 76007, Jul 2017, doi: 10.1117/1.JBO.22.7.076007.
[216] L. S. Halperin, R. J. Olk, G. Soubrane, and G. Coscas, "Safety of fluorescein angiography during pregnancy," *Am J Ophthalmol,* vol. 109, no. 5, pp. 563-566, May 1990, doi: 10.1016/s0002-9394(14)70686-5.
[217] I. Pavlova, M. Williams, A. El-Naggar, R. Richards-Kortum, and A. Gillenwater, "Understanding the biological basis of autofluorescence imaging for oral cancer detection: high-resolution fluorescence microscopy in viable tissue," *Clin Cancer Res,* vol. 14, no. 8, pp. 2396-2404, Apr 2008, doi: 10.1158/1078-0432.CCR-07-1609.
[218] T. Kuiper *et al.*, "Automatic optical diagnosis of small colorectal lesions by laser-induced autofluorescence," *Endoscopy,* vol. 47, no. 1, pp. 56-62, Jan 2015, doi: 10.1055/s-0034-1378112.
[219] O. Warburg, W. Christian, and A. Griese, "Hydrogen Transferring Coenzyme Its Composition and Mode of Functioning," *Biochem Z.,* vol. 208, pp. 157-205, 1935.
[220] B. Chance, "Spectra and reaction kinetics of respiratory pigments of homogenized and intact cells," *Nature,* vol. 169, no. 4293, pp. 215-221, Feb 1952, doi: 10.1038/169215a0.
[221] B. Chance, P. Cohen, F. Jobsis, and B. Schoener, "Intracellular oxidation-reduction states in vivo," *Science,* vol. 137, no. 3529, pp. 499-508, Aug 1962, doi: 10.1126/science.137.3529.499.
[222] M. G. Vander Heiden, L. C. Cantley, and C. B. Thompson, "Understanding the Warburg effect: the metabolic requirements of cell proliferation," *Science,* vol. 324, no. 5930, pp. 1029-1033, May 2009, doi: 10.1126/science.1160809.
[223] M. V. Liberti and J. W. Locasale, "The Warburg Effect: How Does it Benefit Cancer Cells?," *Trends Biochem Sci,* vol. 41, no. 3, pp. 211-218, Mar 2016, doi: 10.1016/j.tibs.2015.12.001.
[224] H. N. Xu, J. Tchou, M. Feng, H. Zhao, and L. Z. Li, "Optical redox imaging indices discriminate human breast cancer from normal tissues," *J Biomed Opt,* vol. 21, no. 11, p. 114003, Nov 2016, doi: 10.1117/1.JBO.21.11.114003.
[225] H. N. Xu, S. Nioka, J. D. Glickson, B. Chance, and L. Z. Li, "Quantitative mitochondrial redox imaging of breast cancer metastatic potential," *J Biomed Opt,* vol. 15, no. 3, p. 036010, May 2010, doi: 10.1117/1.3431714.
[226] Y. Wen, H. N. Xu, L. Privette Vinnedge, M. Feng, and L. Z. Li, "Optical Redox Imaging Detects the Effects of DEK Oncogene Knockdown on the Redox State of MDA-MB-231 Breast Cancer Cells," *Mol Imaging Biol,* vol. 21, no. 3, pp. 410-416, Jun 2019, doi: 10.1007/s11307-019-01321-w.
[227] A. T. Shah, M. Demory Beckler, A. J. Walsh, W. P. Jones, P. R. Pohlmann, and M. C. Skala, "Optical Metabolic Imaging of Treatment Response in Human Head and Neck Squamous Cell Carcinoma," *PLoS One,* vol. 9, no. 3, p. e90746, 2014, doi: 10.1371/journal.pone.0090746.

[228] B. Quistorff, J. C. Haselgrove, and B. Chance, "High spatial resolution readout of 3-D metabolic organ structure: an automated, low-temperature redox ratio-scanning instrument," *Anal Biochem,* vol. 148, no. 2, pp. 389-400, Aug 1985, doi: 10.1016/0003-2697(85)90244-1.
[229] M. Ranji *et al.*, "Fluorescent Images of Mitochondrial Redox States Inin Situmouse Hypoxic Ischemic Intestines," *J Innov Opt Heal Sci,* vol. 02, no. 04, pp. 365-374, 2011, doi: 10.1142/s1793545809000723.
[230] M. F. la Cour *et al.*, "Optical metabolic imaging of irradiated rat heart exposed to ischemia-reperfusion injury," *J Biomed Opt,* vol. 23, no. 1, pp. 1-9, Jan 2018, doi: 10.1117/1.JBO.23.1.016011.
[231] S. Mehrvar, M. F. la Cour, M. Medhora, A. K. S. Camara, and M. Ranji, "Optical Metabolic Imaging for Assessment of Radiation-Induced Injury to Rat Kidney and Mitigation by Lisinopril," *Ann Biomed Eng,* vol. 47, no. 7, pp. 1564-1574, Jul 2019, doi: 10.1007/s10439-019-02255-8.
[232] L. Z. Li, H. N. Xu, M. Ranji, S. Nioka, and B. Chance, "Mitochondrial Redox Imaging for Cancer Diagnostic and Therapeutic Studies," *J Innov Opt Health Sci,* vol. 2, no. 4, pp. 325-341, Oct 2009, doi: 10.1142/S1793545809000735.
[233] H. N. Xu, J. Tchou, B. Chance, and L. Z. Li, "Imaging the Redox States of Human Breast Cancer Core Biopsies," *Advances in Experimental Medicine and Biology,* pp. 343-349, Feb 2013, doi: 10.1007/978-1-4614-4989-8_48.
[234] S. Wu *et al.*, "Quantitative evaluation of redox ratio and collagen characteristics during breast cancer chemotherapy using two-photon intrinsic imaging," *Biomed Opt Express,* vol. 9, no. 3, pp. 1375-1388, Mar 2018, doi: 10.1364/BOE.9.001375.
[235] M. C. Skala *et al.*, "In vivo multiphoton microscopy of NADH and FAD redox states, fluorescence lifetimes, and cellular morphology in precancerous epithelia," *Proc Natl Acad Sci U S A,* vol. 104, no. 49, pp. 19494-19499, Dec 2007, doi: 10.1073/pnas.0708425104.
[236] D. A. Gil, D. Deming, and M. C. Skala, "Patient-derived cancer organoid tracking with wide-field one-photon redox imaging to assess treatment response," *J Biomed Opt,* vol. 26, no. 3, p. 036005, Mar 2021, doi: 10.1117/1.JBO.26.3.036005.
[237] P. F. Favreau, J. He, D. A. Gil, D. A. Deming, J. Huisken, and M. C. Skala, "Label-free redox imaging of patient-derived organoids using selective plane illumination microscopy," *Biomed Opt Express,* vol. 11, no. 5, pp. 2591-2606, May 2020, doi: 10.1364/BOE.389164.
[238] R. A. Romano, R. G. Teixeira Rosa, A. G. Salvio, J. A. Jo, and C. Kurachi, "Multispectral autofluorescence dermoscope for skin lesion assessment," *Photodiagnosis Photodyn Ther,* vol. 30, p. 101704, Jun 2020, doi: 10.1016/j.pdpdt.2020.101704.
[239] W. Liang, G. Hall, B. Messerschmidt, M. J. Li, and X. Li, "Nonlinear optical endomicroscopy for label-free functional histology in vivo," *Light Sci Appl,* vol. 6, no. 11, pp. e17082-e17082, May 2017, doi: 10.1038/lsa.2017.82.
[240] B. L. Meena, A. Agarwal, C. Pantola, K. Pandey, and A. Pradhan, "Concentration of FAD as a marker for cervical precancer detection," *J*

Biomed Opt, vol. 24, no. 3, pp. 1-7, Mar 2019, doi: 10.1117/1.JBO.24.3.035008.
[241] W. Q. Zhang *et al.*, "Development of an optical fiber-based redox monitoring system for tissue metabolism," *J Biophotonics,* vol. 15, no. 4, p. e202100304, Apr 2022, doi: 10.1002/jbio.202100304.
[242] J. A. Udovich, N. D. Kirkpatrick, A. Kano, A. Tanbakuchi, U. Utzinger, and A. F. Gmitro, "Spectral background and transmission characteristics of fiber optic imaging bundles," *Applied optics,* vol. 47, no. 25, pp. 4560-4568, Sep 2008, doi: 10.1364/ao.47.004560.
[243] S. M. Willems, C. H. van Deurzen, and P. J. van Diest, "Diagnosis of breast lesions: fine-needle aspiration cytology or core needle biopsy? A review," *J Clin Pathol,* vol. 65, no. 4, pp. 287-292, Apr 2012, doi: 10.1136/jclinpath-2011-200410.
[244] H. L. Park and J. Hong, "Vacuum-assisted breast biopsy for breast cancer," *Gland Surg,* vol. 3, no. 2, pp. 120-127, May 2014, doi: 10.3978/j.issn.2227-684X.2014.02.03.
[245] J. H. Youk, E. K. Kim, M. J. Kim, J. Y. Lee, and K. K. Oh, "Missed breast cancers at US-guided core needle biopsy: how to reduce them," *Radiographics,* vol. 27, no. 1, pp. 79-94, Jan 2007, doi: 10.1148/rg.271065029.
[246] L. Spinelli, A. Torricelli, A. Pifferi, P. Taroni, G. M. Danesini, and R. Cubeddu, "Bulk optical properties and tissue components in the female breast from multiwavelength time-resolved optical mammography," *J Biomed Opt,* vol. 9, no. 6, pp. 1137-1142, Nov 2004, doi: 10.1117/1.1803546.
[247] S. C. Kanick *et al.*, "Scattering phase function spectrum makes reflectance spectrum measured from Intralipid phantoms and tissue sensitive to the device detection geometry," *Biomed Opt Express,* vol. 3, no. 5, pp. 1086-1100, May 2012, doi: 10.1364/BOE.3.001086.
[248] "Validation of analytical procedures: text and methodology Q2(R1)," in "ICH Harmonized Tripartite Guideline," International Council for Harmonisation, 2005.
[249] A. N. Bashkatov, E. A. Genina, V. I. Kochubey, and V. V. Tuchin, "Optical properties of human skin, subcutaneous and mucous tissues in the wavelength range from 400 to 2000 nm," *J Phys D Appl Phys,* vol. 38, no. 15, pp. 2543-2555, Aug 2005, doi: 10.1088/0022-3727/38/15/004.
[250] J. Brazard, A. Usman, F. Lacombat, C. Ley, M. M. Martin, and P. Plaza, "New insights into the ultrafast photophysics of oxidized and reduced FAD in solution," *J Phys Chem A,* vol. 115, no. 15, pp. 3251-3262, Apr 2011, doi: 10.1021/jp110741y.
[251] G. Li and K. D. Glusac, "The role of adenine in fast excited-state deactivation of FAD: a femtosecond mid-IR transient absorption study," *J Phys Chem B,* vol. 113, no. 27, pp. 9059-9061, Jul 2009, doi: 10.1021/jp905020u.
[252] B. Chance, B. Schoener, R. Oshino, F. Itshak, and Y. Nakase, "Oxidation-reduction ratio studies of mitochondria in freeze-trapped samples. NADH and flavoprotein fluorescence signals," *J Biol Chem,* vol. 254, no. 11, pp. 4764-4771, Jun 1979, doi: 10.1016/s0021-9258(17)30079-0.

[253] H. N. Xu *et al.*, "Optical Redox Imaging of Lonidamine Treatment Response of Melanoma Cells and Xenografts," *Mol Imaging Biol,* vol. 21, no. 3, pp. 426-435, Jun 2019, doi: 10.1007/s11307-018-1258-z.
[254] F. Bartolomé and A. Y. Abramov, "Measurement of Mitochondrial NADH and FAD Autofluorescence in Live Cells," Springer New York, 2015, pp. 263-270.
[255] M. Forkink, F. Basit, J. Teixeira, H. G. Swarts, W. J. H. Koopman, and P. Willems, "Complex I and complex III inhibition specifically increase cytosolic hydrogen peroxide levels without inducing oxidative stress in HEK293 cells," *Redox Biol,* vol. 6, pp. 607-616, Dec 2015, doi: 10.1016/j.redox.2015.09.003.
[256] L. Z. Li *et al.*, "Quantitative magnetic resonance and optical imaging biomarkers of melanoma metastatic potential," *Proc Natl Acad Sci U S A,* vol. 106, no. 16, pp. 6608-6613, Apr 2009, doi: 10.1073/pnas.0901807106.
[257] L. Moon, D. W. Frederick, J. A. Baur, and L. Z. Li, "Imaging Redox State in Mouse Muscles of Different Ages," *Adv Exp Med Biol,* vol. 977, pp. 51-57, Nov 2017, doi: 10.1007/978-3-319-55231-6_8.
[258] Z. Zhang *et al.*, "Redox ratio of mitochondria as an indicator for the response of photodynamic therapy," *J Biomed Opt,* vol. 9, no. 4, pp. 772-778, Jul 2004, doi: 10.1117/1.1760759.
[259] Z. Zhang *et al.*, "Rapamycin maintains NAD(+)/NADH redox homeostasis in muscle cells," *Aging (Albany NY),* vol. 12, no. 18, pp. 17786-17799, Sep 2020, doi: 10.18632/aging.103954.
[260] F. K. Chan, K. Moriwaki, and M. J. De Rosa, "Detection of necrosis by release of lactate dehydrogenase activity," *Methods in Molecular Biology,* vol. 979, pp. 65-70, Feb 2013, doi: 10.1007/978-1-62703-290-2_7.
[261] P. M. Tang *et al.*, "Photodynamic therapy inhibits P-glycoprotein mediated multidrug resistance via JNK activation in human hepatocellular carcinoma using the photosensitizer pheophorbide a," *Mol Cancer,* vol. 8, no. 1, p. 56, Jul 2009, doi: 10.1186/1476-4598-8-56.
[262] Y. Miki, J. Akimoto, K. Moritake, C. Hironaka, and Y. Fujiwara, "Photodynamic therapy using talaporfin sodium induces concentration-dependent programmed necroptosis in human glioblastoma T98G cells," *Lasers Med Sci,* vol. 30, no. 6, pp. 1739-1745, Aug 2015, doi: 10.1007/s10103-015-1783-9.
[263] B. W. Pogue *et al.*, "In vivo NADH fluorescence monitoring as an assay for cellular damage in photodynamic therapy," *Photochem Photobiol,* vol. 74, no. 6, pp. 817-824, Dec 2001, doi: 10.1562/0031-8655.
[264] S. M. Mahalingam, J. D. Ordaz, and P. S. Low, "Targeting of a Photosensitizer to the Mitochondrion Enhances the Potency of Photodynamic Therapy," *ACS Omega,* vol. 3, no. 6, pp. 6066-6074, June 2018, doi: 10.1021/acsomega.8b00692.
[265] M. Guirguis *et al.*, "Membrane composition is a functional determinant of NIR-activable liposomes in orthotopic head and neck cancer," *Nanophotonics,* vol. 10, no. 12, pp. 3169-3185, Sep 2021, doi: 10.1515/nanoph-2021-0191.

[266] B. Gaitan, C. T. Inglut, Y. Liu, Y. Chen, and H. C. Huang, "Depth-resolved imaging of photosensitizer in the rodent brain using fluorescence laminar optical tomography," *J Biomed Opt,* vol. 25, no. 9, p. 096007, Sep 2020, doi: 10.1117/1.JBO.25.9.096007.
[267] OECD, *Test No. 432: In Vitro 3T3 NRU Phototoxicity Test* (OECD Guidelines for the Testing of Chemicals, Section 4). 2019.
[268] M. Tanase *et al.*, "Role of Carbonyl Modifications on Aging-Associated Protein Aggregation," *Scientific Reports,* vol. 6, no. 1, p. 19311, Jan 2016, doi: 10.1038/srep19311.
[269] K. Uluc, G. C. Kujoth, and M. K. Baskaya, "Operating microscopes: past, present, and future," *Neurosurg Focus,* vol. 27, no. 3, p. E4, Sep 2009, doi: 10.3171/2009.6.FOCUS09120.
[270] M. A. van Veelen, C. J. Snijders, E. van Leeuwen, R. H. Goossens, and G. Kazemier, "Improvement of foot pedals used during surgery based on new ergonomic guidelines," *Surg Endosc,* vol. 17, no. 7, pp. 1086-1091, Jul 2003, doi: 10.1007/s00464-002-9185-z.